Ranging-Based Adaptive Navigation for Autonomous Micro Aerial Vehicles

Nguyen Pham Nhat Thien Minh

School of Electrical & Electronic Engineering

A thesis submitted to the Nanyang Technological University
in partial fulfillment of the requirements for the degree of
Doctor of Philosophy

2020

Statement of Originality

I hereby certify that the work embodied in this thesis is the result of original research, is free of plagiarised materials, and has not been submitted for a higher degree to any other University or Institution.

11th February 2020
.....

Date

.....

Nguyen Pham Nhat Thien Minh

Supervisor Declaration Statement

I have reviewed the content and presentation style of this thesis and declare it is free of plagiarism and of sufficient grammatical clarity to be examined. To the best of my knowledge, the research and writing are those of the candidate except as acknowledged in the Author Attribution Statement. I confirm that the investigations were conducted in accord with the ethics policies and integrity standards of Nanyang Technological University and that the research data are presented honestly and without prejudice.

11th February 2020

.....

Date

.....

Prof. Lihua XIE

Authorship Attribution Statement

This thesis contains material from 5 papers published in the following peer-reviewed journals / conferences in which I am listed as an author.

Chapter 3 is published as Thien-Minh Nguyen, Abdul Hanif Zaini, Chen Wang, Kexin Guo, and Lihua Xie, "Robust Target-Relative Localization with Ultra-Wideband Ranging and Communication", in 2018 IEEE International Conference on Robotics and Automation (ICRA), pp. 2312-2319, May 2018.
DOI: 10.1109/ICRA.2018.8460844.

The contributions of the co-authors are as follows:

- I proposed the idea, formulated the problem, designed the experiments, and prepared the manuscript.
- Abdul Hanif Zaini, Chen Wang and Kexin Guo and I conducted the experiments.
- The manuscript was revised by Prof. Lihua Xie.

Chapter 4 is published as Thien-Minh Nguyen, Zhirong Qiu, Muqing Cao, Thien Hoang Nguyen, and Lihua Xie, "Single Landmark Distance-Based Navigation", in IEEE Transactions on Control Systems Technology, 2019, accepted, early access at https://ieeexplore.ieee.org/document/8754704.
DOI: 10.1109/TCST.2019.2916089.

The contributions of the co-authors are as follows:

- I proposed the idea, formulated the problem, designed the experiments, and prepared the manuscript.
- Dr. Zhirong Qiu assisted in the theoretical analyses.
- Muqing Cao, Thien Hoang Nguyen, and I conducted the experiment.
- The manuscript was revised by Prof. Lihua Xie.

Chapter 5 is published as Thien-Minh Nguyen, Thien Hoang Nguyen, Muqing Cao, Zhirong Qiu, and Lihua Xie, "Integrated UWB-Vision Approach for Autonomous Docking of UAVs in GPS-Denied Environments", in 2019 IEEE International Conference on Robotics and Automation (ICRA), pp. 9603-9609, May 2019.
DOI:10.1109/ICRA.2019.8793851.

The contributions of the co-authors are as follows:

- I proposed the idea, formulated the problem, designed the experiments, and prepared the manuscript.
- Thien Hoang Nguyen, Muqing Cao, and I conducted the experiment.

- The manuscript was revised by Prof. Lihua Xie and Dr. Zhirong Qiu.

Chapter 6 is published as Thien-Minh Nguyen, Zhirong Qiu, Thien Hoang Nguyen, Muqing Cao, and Lihua Xie, "Distance-Based Cooperative Relative Localization and Leader-Following Control of MAVs", in IEEE Robotics and Automation Letters, vol. 4, no. 4, pp. 3641-3648, 2019 (the contents of this paper are also selected by IROS'19 Program Committee for presentation at the Conference).
DOI: 10.1109/LRA.2019.2926671.

The contributions of the co-authors are as follows:

- I proposed the idea, formulated the problem, designed the experiments, and prepared the manuscript.
- Dr. Zhirong Qiu assisted in the theoretical analyses.
- Thien Hoang Nguyen, Muqing Cao, and I conducted the experiment.
- The manuscript was revised by Prof. Lihua Xie and Dr. Zhirong Qiu.

Chapter 7 is submitted as Thien-Minh Nguyen, Zhirong Qiu, Thien Hoang Nguyen, Muqing Cao, and Lihua Xie, "Persistently-Excited Adaptive Relative Localization and Time-Varying Formation of Robot Swarms", in IEEE Transaction on Robotics, accepted, early access at https://ieeexplore.ieee.org/document/8931008.
DOI: 10.1109/TRO.2019.2954677

The contributions of the co-authors are as follows:

- I proposed the idea, formulated the problem, designed the experiments, and prepared the manuscript.
- Dr. Zhirong Qiu assisted in the theoretical analyses.
- Thien Hoang Nguyen, Muqing Cao, and I conducted the experiment.
- The manuscript was revised by Prof. Lihua Xie.

11th February 2020 ..... Date

..... Nguyen Pham Nhat Thien Minh

Acknowledgements

I would like to sincerely thank my advisor, Professor Xie Lihua, for giving me a wonderful opportunity to pursue my study at NTU. Professor Xie's encouragement, guidance and his academic professionalism are undoubtedly the best foundation one can ask for in his research career. This thesis would not be possible without his tremendous support.

I am totally indebted by all of the support from my wonderful colleagues. I would like to thank my colleague Abdul Hanif bin Zaini for helping me gain many hands-on engineering skills in working with MAVs. I would like to express my highest regards to Dr. Qiu Zhirong, whose mathematical acumen was crucial in helping tackle many tough problems we came across in our works. I would like to sincerely thank our colleagues Cao Muqing and Nguyen Hoang Thien for their valuable practical experience that helped bring about the real-world demonstrations for many of our ideas. I would like to send many thanks to my seniors Dr. Guo Kexin for all of his experience with the UWB systems and Dr. Wang Chen for sharing many useful software tools and techniques with us. I would like to thank Dr. Chen Chun Lin, Dr. Li Xiuxian, Hoang Minh Chung, Fang Xu, Wang Han, Ji Tete, Li Juncheng, our collaborators from STE Aerospace Pang Jia Hui, Li Luowen, Teong Soo Soon for all of the assistance and the pleasant interactions we have had over the years.

Last but not least, I would like to express my deepest gratitude to my dear parents, grandparents, brother, cousins, aunts, uncles, other family members and my significant other that have always looked after and wished me the best on my journey. I would not have got this far without your encouragement.

"I am a great believer in luck, the harder I work the more I seem to have it."

—Thomas Jefferson (*attributed*)

To my dear family

Abstract

The last decade has witnessed a surge in popularity of Micro Aerial Vehicles (MAVs) in many civilian, industrial and military applications. It can be seen that most research interests on MAV revolve around two main problems, namely localization and navigation, or estimation and control in a more general sense. Most commonly we find that these two problems are addressed in a separate manner, whereas localization capability is the basis upon which different navigation strategies are developed. While this approach may facilitate convenient solutions and analysis, it also brings about several compromises, such as low adaptability to complex/cluttered environments when localization relies on an external positioning system, or estimation drift and limited cooperative capability for MAVs relying on onboard visual odometry (VO) systems. Motivated by these issues, this thesis is dedicated to studying infrastructure-free navigation schemes that can achieve a high level of flexibility, portability and practicality for autonomous operations of multi-MAV systems in GPS-denied environments. As will be shown later, ranging-based integrated estimation-control technique, i.e. adaptive navigation, is the key in our approach towards this objective.

As a first expedition into this direction, a sensor fusion scheme is proposed to achieve relative positioning and tracking of a target by MAV, featuring the use of multiple Ultra-wideband (UWB) ranging sensors strategically installed on both the MAV and the target. An estimator based on Extended Kalman Filter (EKF) is developed to fuse UWB ranging measurements with data from onboard sensors such as inertial measurement unit (IMU), altimeters and optical flow. In addition, UWB-based communication capability is utilized to transfer the target's onboard information to the quadcopter. Experiment results demonstrate the ability of the MAV to robustly control its position relative to a moving target even with uncertain velocity.

While the aforementioned method of ranging to multiple UWB nodes on the target can achieve effective relative positioning and tracking at a close range, to

maximize the operation range and flexibility, it would be more convenient to rely on a single beacon ranging scheme. Thus, we formulate a distance-based adaptive navigation problem where the MAV is required to approach a landmark at an arbitrary unknown location. To solve this problem, we propose an integrated estimation-control scheme to simultaneously accomplish two objectives: relative localization using only distance and odometry measurements, and navigation to a desired location under a nonlinear distance-based bounded control law. Asymptotic convergence is obtained by invoking the discrete-time LaSalle's invariance principle in the noise-free case, and the stability under distance measurement noise is also investigated. Multiple numerical simulations and real-world experiments on quadcopter MAV in GPS-denied environments are carried out to validate theoretical findings and the efficacy of the proposed estimation-control scheme.

In the next phase, a ranging-based *autonomous docking* operation in GPS-denied environment is conceived with the insights from previous investigations. Specifically, a method combining sequential ranging of UWB sensor with vision-based techniques is developed to achieve both autonomous approaching and landing capabilities in GPS-denied environments. In the approaching phase, a recursive least-squares optimization algorithm is proposed to estimate the position of the MAV relative to the target by using the distance and relative displacement measurements. Using this estimate, MAV is able to efficiently approach the target until the landing pad is detected by an onboard vision system, then UWB measurements and vision-derived poses are fused with other onboard sensor information to facilitate an accurate landing maneuver. Real-world experiments are conducted to demonstrate the efficiency of the proposed method.

Based on the insights from the aforementioned single-MAV localization-navigation schemes, we set out to develop new cooperative operations of multi-MAV systems. On this direction, we investigate the problem of leader-following control of multiple MAVs, which is then extended to distributed adaptive control of dynamic formation of multi-MAV system, supported by relative position estimate derived from distance and self-displacement measurements. The main challenge of the problem, which is to simultaneously fulfill both relative localization and control tasks, is resolved by different approaches to guaranteeing the *persistent excitation* (PE) condition, i.e the introduction of specialized agents, or by embedding the distance-based relative localization technique into a *time-varying formation*. By

assuming that the leader is globally reachable and selecting proper parameters for the estimation and control laws, it is shown that the integrated estimation-control schemes ensure exponential convergence (EC) of relative localization error, which leads to EC of formation error when the leader's behavior is deterministic, and bounded formation error for a nondeterministic leader. Extensive numerical simulations and real-world implementations are carried out to verify the theoretical results and demonstrate the efficacy and effectiveness of the proposed method.

Contents

List of Figures

List of Tables

Symbols and Acronyms

Symbols

$\mathbb{N}$, $\mathbb{N}^+$	the sets of natural numbers and positive natural numbers, respectively
$\mathbb{R}$, $\mathbb{R}^+$	the set of real numbers and non-negative real numbers, respectively
$\mathbb{R}^m$	the set of m-dimensional real number column vectors
$\mathbb{R}^{m\times n}$	the set of real $m \times n$ matrices
A'	the transpose of matrix A
$\varsigma_M(A)$	the largest singular value of matrix A
$\varsigma_m(A)$	the smallest singular value of matrix A
I	the identity matrix
$\mathrm{col}\{\dots\}$	the column vector formed by stacking vectors in the set $\{\dots\}$
$\langle x, y\rangle$	the inner product of two vectors x, y
$\circ$	the quaternion product
$\otimes$	the Kronecker product
$\|\cdot\|$	the 2-norm of a vector or matrix norm induced by vector norm
$\|\cdot\|_\infty$	the infinity norm of a vector
$\|\cdot\|$	the absolute value of a real number or the cardinality of a set
$\bar{\mathcal{B}}(p, r)$	the ball centered at p with the radius r
$\angle(a, b)$	the angle between two vectors a and b
$\lceil x\rceil$	the least integer greater than or equal to x
$\lfloor x\rfloor$	the greatest integer less than or equal to x
$\mathrm{span}\{\dots\}$	the span of a set of vectors
$\limsup_{k\to\infty} x(k)$	limit superior of the sequence $x(k)$
$\liminf_{k\to\infty} x(k)$	limit inferior of the sequence $x(k)$
$\max_{y\in S} x(y)$	maximum of $x(y)$ where y takes value from the set S
$\min_{y\in S} x(y)$	minimum of $x(y)$ where y takes value from the set S

$\arg\max_{y \in S} x(y)$	argument of the maximum of $x(y)$ over the set S
$\arg\min_{y \in S} x(y)$	argument of the minimum of $x(y)$ over the set S
$x(k) \equiv y$	$x(k)$ is identically equal to y for all value of k
$x(k) \not\equiv y$	there exists k such that $x(k)$ is not equal to y

Acronyms

MAV	Micro aerial vehicle
UGV	Unmanned ground vehicle
GPS	Global positioning system
VO	Visual odometry
VIO	Visual-inertial odometry
UWB	Ultra-wideband
IMU	Inertial measurement unit
TOA	Time of arrival
TDOA	Time difference of arrival
TWTOF	Two-way time of flight
TDMA	Time division multiple access
FOV	Field of view
EKF	Extended Kalman filter
SLAM	Simultaneous localization and mapping
ROS	Robot operating system
3D	3-dimensional
2D	2-dimensional
RMS	Root mean square
SD	Standard deviation
DAG	Directed acyclic graph
EC	Exponential convergence
PE	Persistent excitation
e.c.	exponentially convergent
p.e.	persistently exciting

Chapter 1

Introduction

1.1 Scope and Overview

Over the last decade, Micro Aerial Vehicle (MAV) applications have become pervasive in many sectors of our society, e.g. aerial mapping [1], agriculture [2], search and rescue [3]. Recently some researchers have begun exploring possible applications of multiple MAVs in complex tasks such as area coverage [4, 5], transport [6, 7] and military operations [8]. However, existing applications are still focusing on the use of a small number of MAVs, and the potential of large-scale cooperative multi-MAV systems is still open to more investigation, as many technological and methodological gaps still need to be resolved before multi-MAV applications can actually reach maturity.

In general, to realize most multi-robot systems, or multi-MAV systems in particular, two basic prerequisites have to be satisfied. First, each MAV must possess a level of *self-sustained mobility*, i.e. the capability of estimating and controlling its own position within an environment. Second, the robot must be able to obtain the position, or more specifically relative position, of its neighbour to synthesize its control and decision subject to some defined tasks. This can be referred to as *relative localization* capability.

On the first requirement, generally speaking, there exist two methods for its realization. The first approach involves the use of an *external localization system*, and the second focuses on an *onboard perception system*. Examples of external

localization system include those relying on one or multiple navigational satellite systems (GPS[1], GLONASS[2], Galileo[3], BDS[4]), motion capture system [9–11] or indoor beacon-based system [12–16]. Indeed, it can be seen that with the access to a common external localization system, by having the robots exchange their position via some communication network, the relative localization prerequisite can also be accomplished straightforwardly. This approach is often adopted to demonstrate many large-scale multi-robot schemes in literature such as flocking [17, 18], formation [19–21] and interception [22–24]. However, the use of infrastructure in these systems bring about several issues such as limited coverage, additional deployment-maintenance costs as well as labor-intensive calibration and troubleshooting. As a consequence, applications based on these systems face significant challenges when operating in cluttered and complex environments.

On the other hand, the aforementioned issues can be generally avoided with the use of perception-based localization systems, e.g Visual Odometry (VO) or Simultaneous Localization and Mapping (SLAM) with mono/stereo cameras or laser scanners (LiDAR). Indeed, onboard perception methods have become quite mature and is now a standard approach for many autonomous operations of MAVs [25–31]. However, though the limitations associated with external localization system can be avoided with perception-based localization, new challenges in delivering relative localization for multi-MAV systems would arise. Specifically, while perception-based techniques are effective for single MAV applications, in multi-MAVs operations, since each visual localization system uses a different frame of reference, collaborative operations between the MAVs would require *a priori* knowledge to convert the position information from one frame to another [32], or involves a central station to combine the camera information from multiple MAVs [33]. In either way, these extra requirements would hinder the flexibility and scalability of the multi-MAV scheme.

As it is ever more certain that onboard perception systems would be the standard approach for self-sustained mobility, in order to accomplish multi-MAVs systems that can operate under GPS-denied condition, it can be seen that the main challenge under this topic is to realize the relative localization capability with minimal

[1] https://www.gps.gov
[2] https://www.glonass-iac.ru/en/
[3] https://galileognss.eu/
[4] http://en.beidou.gov.cn/

deployment cost and maximally achievable flexibility. Indeed, to this end, many extra vision-based techniques have been proposed to allow MAVs to actively track each other [34–37]. However, these vision-based techniques are still subject to limited field of view (FOV), can be easily occluded and require that the MAVs maintain their sight on their neighbours, which entails limited versatility and scalability of the system [38].

Different from these attempts, in this thesis we shall focus on development and integration of relative localization schemes leveraging ranging and basic VO techniques, starting from single-MAV scenarios and then moving towards generalized multi-MAV operations. Similar to perception-based systems, ranging-based methods only rely on onboard sensors, thus is not affected by coverage of GPS signal or restricted to a specific location. Also, as UWB ranging technology is omnidirectional, it can also avoid the problem of limited FOV as with direct relative localization techniques using vision.

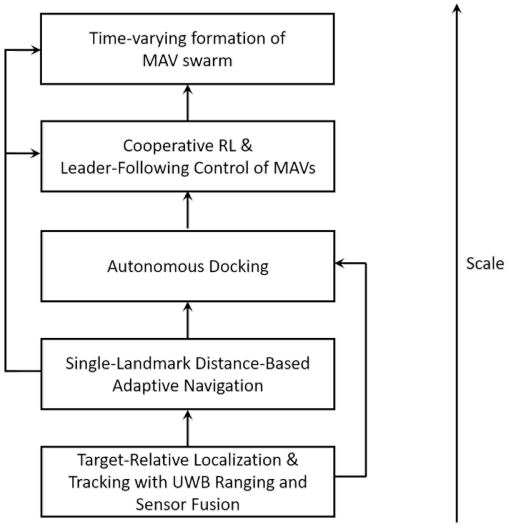

FIGURE 1.1: The course of investigations and their connections in this thesis: from a small-scale relative localization scheme based on UWB ranging and sensor fusion towards integrated relative localization and time-varying formation of MAV swarm.

Figure 1.1 summarizes the course of research in this thesis. In the first step on this direction, we study a sensor fusion scheme to combine UWB ranging measurements with other visual and inertial information to estimate the MAV's position relative to a target, based on which robust tracking capability can be achieved. In order to extend the range and flexibility of the MAV operation, with a slightly different perspective where the target is simplified to a single node, we investigate

a single-landmark distance-based adaptive navigation scheme, in which an integrated localization-navigation technique is developed to simultaneously estimate the position of the MAV relative to the landmark and control it to move towards a desired location. Most importantly, in this navigation scheme we develop a relative localization algorithm based on *distance* and *displacement* measurements, which can be easily acquired from generic ranging and VO techniques. With the accomplishments of relative localization and navigation over both operation ranges, we further integrate the two relative localization schemes to achieve an autonomous approach and precise landing capability for MAV in GPS denied environments.

Based on the insights from these initial developments, in the next phase, we embark on new investigations of multi-MAV adaptive control schemes integrated with the distance-displacement-based relative localization technique developed in the preceding phase. In these studies, we found that while it is well-known that the convergence of a class of related estimators is closely related to the *persistent excitation* (PE) condition, existing works in the literature usually forgo a deliberated guarantee for this condition, thus the obtained results are often unsatisfactory. To tackle this issue, we first conceive a simultaneous relative localization and leader-following control scheme for MAVs, in which a cooperative estimation-control scheme with specialized agents is proposed to satisfy the PE condition. Specifically, by introducing some so-called *orbiters* tasked with maintaining *persistently exciting* (p.e.) trajectories, *exponential convergence* (EC) of both *relative localization* and *tracking errors* can be achieved. Having achieved *exponentially convergent* (e.c.) performance in this manner, we extend the cooperative scheme by embedding the distance-displacement-based relative localization technique into the *time-varying formation* of multi-MAV swarm and further study the convergence and stability of the MAV swarm system under deterministic and nondeterministic behaviors of the leader. Experiments in GPS-denied environments are carried out to verify the theoretical findings for the proposed ranging-based relative localization and formation control of multi-MAV systems.

1.2 Main Contributions

The contribution of this thesis can be stated as follows:

- We develop a sensor fusion scheme to combine UWB measurements with measurements from other onboard sensors to achieve robust close-range relative localization and tracking of a target. Specifically, UWB-based ranging and communication techniques were developed to achieve accurate ranging and exchange of information between MAV and the target. Moreover, strategic installation of the UWB nodes is also deliberated to achieve coupling of the relative position and orientation with the distance observations. In addition, UWB measurements with other onboard sensors such as IMU, altimeter, optical flow, etc. are fused together in an Extended Kalman Filter (EKF) to achieve accurate and robust estimates. Extensive experiments have been conducted to demonstrate the effectiveness and accuracy of this method.

- We investigate a distance-based navigation problem of MAV by using a single landmark placed at an arbitrarily unknown location. In this investigation, an adaptive estimation-control scheme leveraging distance and self-displacement measurements is proposed to estimate the MAV position relative to the landmark. To ensure maximal compatibility with real-world implementation, all dynamics, estimation and control processes are directly formulated and analysed under a discrete-time framework. Moreover, to avoid overburdening the physical system, bounded control input is also considered in the design of the control law. By employing discrete-time LaSalle's invariance principle, asymptotic convergence of the navigation task is established in the noise-free case, and the stability under distance measurement noise is also investigated. Comprehensive simulation and real-world experiments are conducted to demonstrate the efficiency of our method.

- We combine the close range sensor fusion scheme with the long range relative localization and navigation technique to achieve the autonomous docking capability in GPS-denied environment for MAV. Specifically, by using a least-squares-based optimization algorithm, the MAV can localize and approach target from a significant distance, and upon the entry of the target in the MAV camera's FOV, sensor fusion technique can be employed to combine distance and visual information to achieve robust and undisrupted precise landing capability for the MAV. Extensive experiments were conducted to demonstrate the performance of the autonomous docking system with effective approach and landing capability of MAV from over 50m away.

- We propose a cooperative estimation-control scheme where specialized agents called *orbiters* are tasked with maintaining p.e. trajectories to facilitate EC of both *relative localization* and *tracking errors* for itself and others. Discrete-time formulation and bounded control input are considered to ensure maximum compatibility of the algorithm with practical implementation. Under some parametric conditions, it can be shown that both relative localization and tracking errors are *exponentially convergent* (e.c.). Experiments on quadcopters in GPS-denied conditions are carried out to validate the efficacy of the proposed scheme.

- We propose an effective and efficient integration scheme for relative localization and time-varying formation of the MAV swarm, where the time-varying formation objective and the relative localization objective are inherently reinforcing each other: the predefined time-varying formation reference trajectories satisfy a PE condition, which facilitates the EC of relative localization; reciprocally, the time-varying formation can be achieved with EC for a globally reachable and deterministic leader, and with ultimately bounded error for a nondeterministic leader. Note that for the nondeterministic case, different from related works that study the coordination problem of multi-agent system under input saturation and external disturbance, which employed small gain approach to avoid saturation and can only achieve semi-global stability, our analysis establishes a global stability and the predicted error bound matches closely with the simulation result. Experiments on quadcopters is also carried out to further validate the result.

1.3 Organisation of the Thesis

The rest of this thesis is organised as follows:

- Chapter 2 presents a literature review on relevant research on localization, relative localization and navigation of MAV/multi-MAV systems.

- Chapter 3 describes the target-relative localization and tracking by MAV with UWB-based ranging, communication and sensor fusion techniques.

- Chapter 4 details the study on a single landmark distance-based adaptive navigation problem, in which an important finding on the distance-displacement-based relative localization algorithm is achieved.

- Chapter 5 introduces the integration of distance-displacement-based relative localization algorithm with sensor fusion technique for autonomous docking of MAV in GPS-denied environments.

- Chapter 6 discusses a cooperative relative localization and leader-following control scheme of MAVs, whereas specialized agents are tasked with maintaining p.e. trajectories to induce EC of relative localization and tracking errors in the network.

- Chapter 7 puts forth the integration of the distance-displacement-based relative localization with time-varying formation of MAV swarm, on which convergence of relative localization and time-varying formation objectives are studied under some parametric and topological conditions.

Chapter 2

Literature Review

2.1 GPS-less Localization Techniques for MAVs

It can be seen that for mobile robot in general, and MAV in particular, localization plays the most crucial role. Thus there exists an extensive body of literature spanning across multiple disciplines investigating new methods that can improve the localization capabilities of robots. In this section, we will review some of the relevant localization techniques that MAV can rely on under GPS-denied condition.

2.1.1 Motion Capture Systems

One popular solution for indoor localization is the motion capture system, which utilises several cameras connected to a single computer to calculate the positions and orientations of subjects within view. A typical MCS system would be capable of providing millimetre/degree accuracy and update rates at over 200Hz[1] for high performance aerial control experiments, e.g. indoor formation, cooperative control, acrobatic motions and swarming [9, 11, 39, 40]. However, it can be seen that motion capture system is highly centralised, thus it is costly, has significant setup time (even for a small sensing area) and can usually only be used indoors. These issues would limit its use with proof-of-concept experiments or a ground truth system.

[1] https://www.vicon.com/

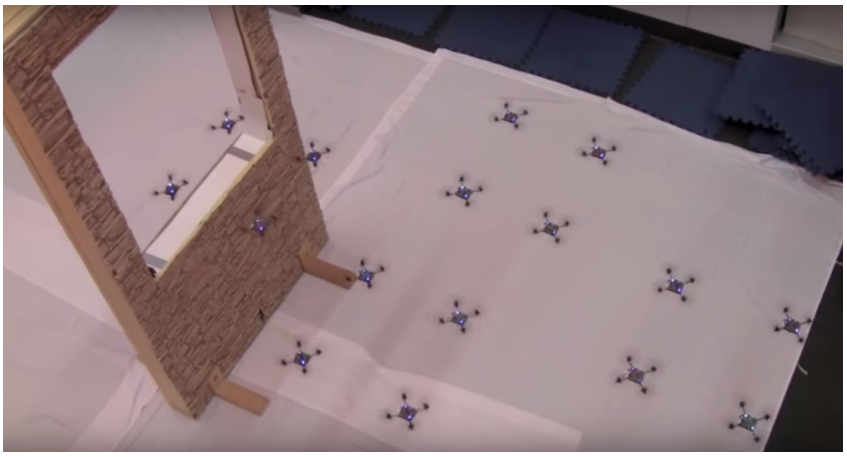

(a) Design and control for aggressive formation flight of quadrotor MAVs with motion capture [39].

(b) A 49-MAV formation using localization based on motion capture by [11].

FIGURE 2.1: Application of motion capture system in studies on multi-MAV systems.

2.1.2 Wireless Positioning Technologies

2.1.2.1 Overview

Different from the motion capture system, in which a central processing unit will process visual information from the camera array to calculate the object's motion, localization using wireless position techniques often involves transmission, reception and calculation of wireless signals from some networked sensors. In fact, one of the most well known localization systems based on this approach is GPS [41], where the GPS receiver detects the signals from some satellites, decodes the message for the location and the distance to the satellites, then estimates its location based on these data. However, GPS signals will suffer greatly from the blocking of line-of-sight and multipath effects. Furthermore, GPS units are unable to work in an

indoor environment. In this case, many researchers have studied wireless sensor networks for their application on localization in indoor environments [16, 42–45]. In this approach, typically some so called anchor nodes will be stationed at known positions, and the distance from an anchor to the MAV can be estimated from the received signals. Table 2.1 provides a review of indoor wireless localization techniques from [46]. Some notable localization methods with direct experiments on MAVs can be listed as [45], which employs Radio Frequency transceivers (e.g. Xbee), and [16], which focuses on ultrasound sensors.

TABLE 2.1: Summary of different wireless technologies for localization by [46].

Technology	**Max. range**	**Power Consumption**	**Advantages**	**Disadvantages**
Wi-Fi	250 m outdoor	Moderate	Widely available, requires simple hardware	Prone to noise, requires complex processing algorithm.
Ultrasound [16]	Couple-tens of meters	Low-moderate	Comparatively less absorption	Dependence on sensor placement
Acoustics [47]	Couple of meters	Low-moderate	Can be used for proprietary applications, can provide high accuracy	Affected by sound pollution, requires extra anchor points or hardware
RFID [48]	200 m	Low	Low power, wide range	Low accuracy
Bluetooth [49]	100 m	Low	High range, low energy consumption	Low accuracy
UWB [50]	10-100 m	Moderate	Immune to interference, high accuracy	Special hardware, high cost
Visible light [51]	1.4 km	Relatively high	Wide-scale availability, potential to provide high accuracy, multi-path-free	Comparatively higher power consumption, range is affected by obstacles, primarily requires LoS

2.1.2.2 UWB-Based Ranging and Localization Techniques

Figure 2.2a provides a visualization of indoor localization techniques in terms of coverage and accuracy. It can be seen from this summary that for applications which require accuracy from 1cm to 1m with a coverage from 10m to 100m, the most appropriate approach would be based on the pulse-based UWB radio technology. As can be seen in Figure 2.2b, with the large bandwidth and pulse-based

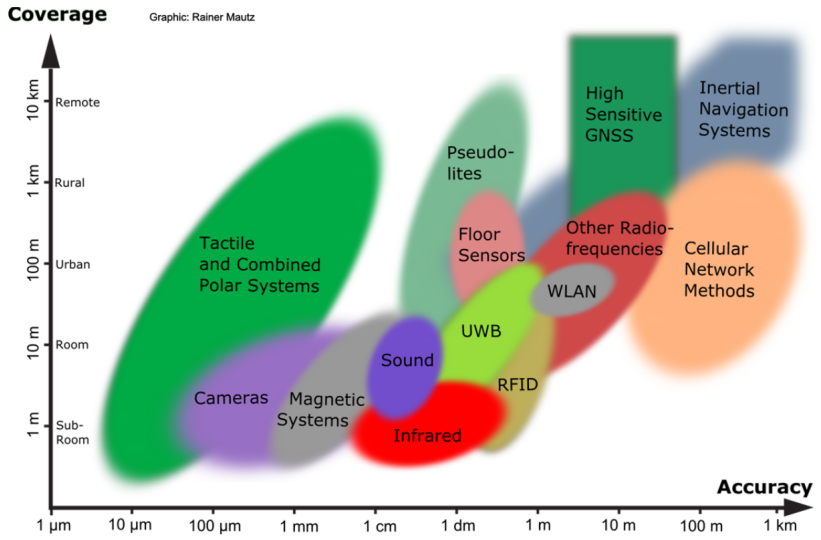

(a) Overview of indoor localization technologies with regard to accuracy and coverage.

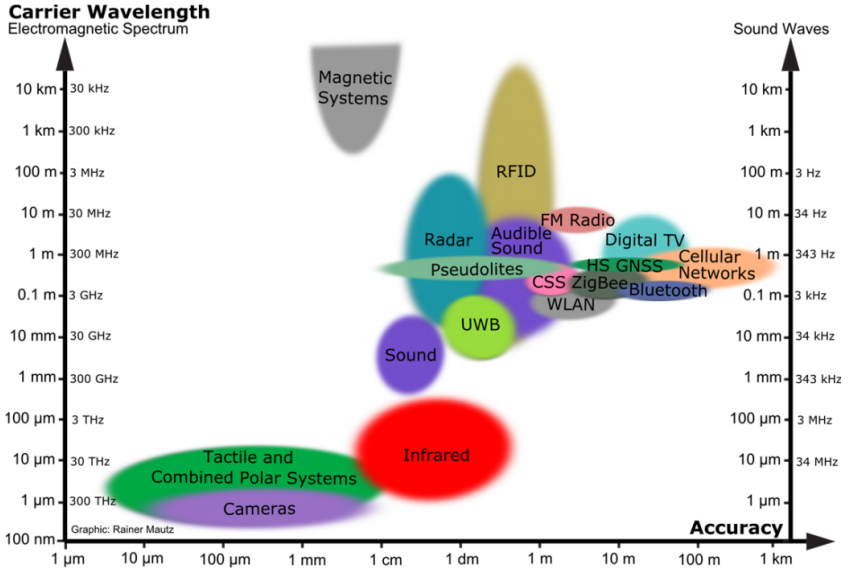

(b) Indoor localization technologies with regard to accuracy and carrier wavelength.

FIGURE 2.2: Classification of localization based on Ultra-wideband among other indoor localization techniques according to [52].

communication, UWB enables spectrum sharing and does not interfere with conventional signals. This technology also has the properties of strong multi-path resistance.

There are two common methods that are often used to obtain distance measurements from UWB signals based on the communication method. In the first method, which resembles the operation principle of GPS, the clocks of the anchor nodes will be synchronized and would periodically emit some signals at fixed intervals. Given the coordinates of the anchor and the time of flight of the signals emitted from

the anchors, the robot can interpret its position. An example of this scheme is the one-way communication method in [15]. As illustrated in Figure 2.3, at time ${}_0T_{-1}^{T_x}$ and time ${}_0T_0^{T_x}$, anchor 0 will broadcast two consecutive messages that are received at time ${}_rT_{-1}^{R_x}$ and time ${}_rT_0^{R_x}$ by the robot. For anchor 1, it will receive the second message from anchor 0 at time ${}_0T_0^{T_x} + \Delta^0 + n_{0,1} + \Delta^1$, where Δ^0 is the internal delay of anchor 0, $n_{0,1}$ is the time of flight for signal from anchor 0 to anchor 1, presumably fixed, and Δ^0 is the internal delay of anchor 1. Hence at time ${}_0T_1^{T_x} = {}_0T_0^{T_x} + \Delta^0 + n_{0,1} + \Delta^0 + \delta_1$ it will broadcast a message that is received at the robot at time ${}_rT_1^{R_x}$. Similarly, anchor 1 will broadcast a message at time ${}_0T_2^{T_x} = {}_0T_0^{T_x} + \Delta^0 + n_{0,2} + \Delta_2 + \delta_2$, which is received by the robot at time ${}_rT_2^{R_x}$. After this, the cycle can be repeated. Given the time instances ${}_rT_0^{R_x}$, ${}_rT_{-1}^{R_x}$, ${}_rT_1^{R_x}$, ${}_rT_2^{R_x}$, the robot can calculate the following observations that are coupled with its position. Specifically, using the time of arrival technique, we can calculate the distance d_i from the robot to the anchor i as follows:

$$d_i = h(p, p_i) = \|p - p_i\| = cf_i = c\left(\frac{{}_rT_i^{R_x} - {}_0T_i^{T_x}}{2} - \Theta\right), \tag{2.1}$$

where p is the position of the MAV, p_i is the anchor's known coordinates, c is the speed of light, f_i is the time of flight of the signal and Θ is the robot's clock offset from the anchor's clock.

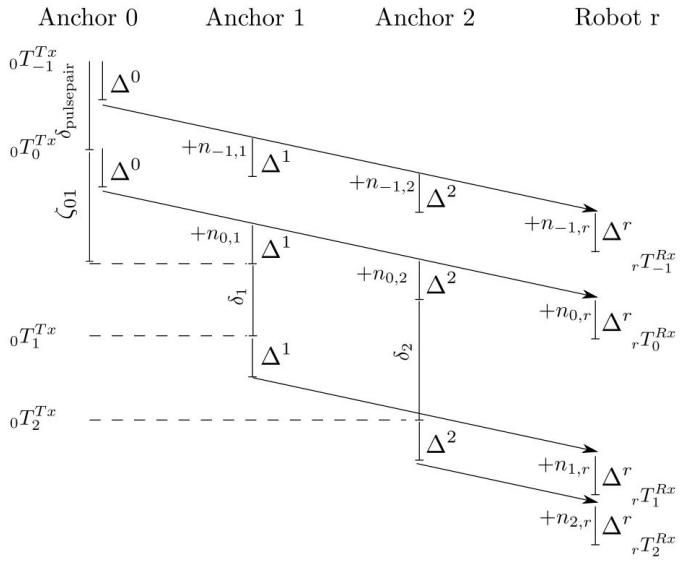

FIGURE 2.3: One-way communication and localization scheme according to [15].

On the other hand, using the Time Difference of Arrival (TDOA) approach, one can obtain the following observation:

$$d_{i,j} = h(p, p_i, p_j) = c\left(\|p - p_i\| - \|p - p_j\|\right) \tag{2.2}$$

$$= c\left[(\rho_{0,r} + 1)({}_rT_i^{R_x} - {}_rT_j^{R_x}) - ({}_0T_i^{T_x} - {}_0T_j^{T_x})\right], \tag{2.3}$$

where $\rho_{0,r} = \dfrac{{}_0T_0^{T_x} - {}_0T_{-1}^{T_x}}{{}_rT_0^{R_x} - {}_rT_{-1}^{R_x}} - 1$ is the skew factor between the MAV's clock and the anchor's clock.

In the second method [14], as illustrated in Figure 2.4, the distance d_i to an anchor i is directly measured via a peer-to-peer Two-way time of flight (TWTOF) scheme as follows:

$$d_i = h(p, p_i) = \|p - p_i\| = cf = c\frac{Q_{M_1}^{R_x} - Q_{M_0}^{T_x} - \delta_Q}{2}, \tag{2.4}$$

where p is the position of the MAV, p_i is the anchor's known coordinates, c is the speed of light, f is the time of flight of the signal, $Q_{M_0}^{T_x}$ is the time instance when the message M_0 is transmitted, $Q_{M_0}^{R_x}$ is the time instance when the reply message M_1 is received on the MAV's clock and $\delta_Q = \delta_A$ is the wait time of the anchor, measured by the MAV's clock as the interval between two consecutive replies M_1 and M_0 from the anchor node.

Given the measurements d_i or $d_{i,j}$ obtained from the aforementioned techniques (2.1), (2.2), (2.4), several techniques can be used to estimate the position of the MAV, e.g. EKF [12–15], non-linear regression [13], or graph optimization methods [53, 54] to estimate the position p of the MAVs.

It can be seen from (2.1), (2.2) that the main disadvantage of one-way communication method is that there is a need for synchronization between the MAV's clock and the anchors' clock. In contrast, in the TWTOF method, there is no need for this synchronization as all time instances are referenced to the MAV's clock, which eliminates a very prominent source of error. Nevertheless, with centimetre-level ranging accuracy, small size and light weight, low-power UWB modules[2][3] using either technique have been widely applied for MAV localization in indoor environments [12–14, 55, 56].

[2] https://www.decawave.com/product/dwm1000-module/
[3] https://www.timedomain.com

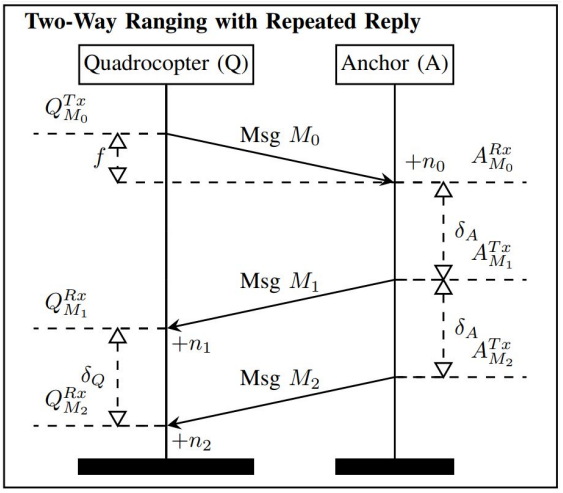

FIGURE 2.4: TWTOF ranging scheme according to [14].

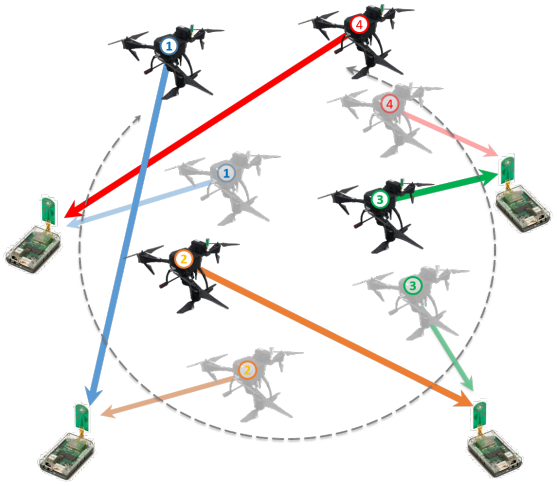

FIGURE 2.5: A synchronised TDMA network of multiple MAVs sequentially ranging to the anchors at known locations over two consecutive time steps.

On the other hand, it should be noted that the number of MAVs that can be supported by the one-way communication scheme is theoretically infinite. While for TWTOF, as one anchor can only communicate with one MAV at a time, at the maximum ranging effeciency, the maximum number of MAVs can only be that of the number of anchors, which is achievable under a Time Division Multiple Access (TDMA) scheme (see Figure 2.5). However, in a multi-MAV operation context, since it is necessary to avoid the use of the anchors, the advantage of the one-way communication method on the number of MAVs that can be supported may not be relevant. Rather, the TWTOF can be adopted and the peer-to-peer ranging sequence can be studied under a switching topology framework. In this thesis, we mainly focus on the application of TWTOF ranging technique of UWB.

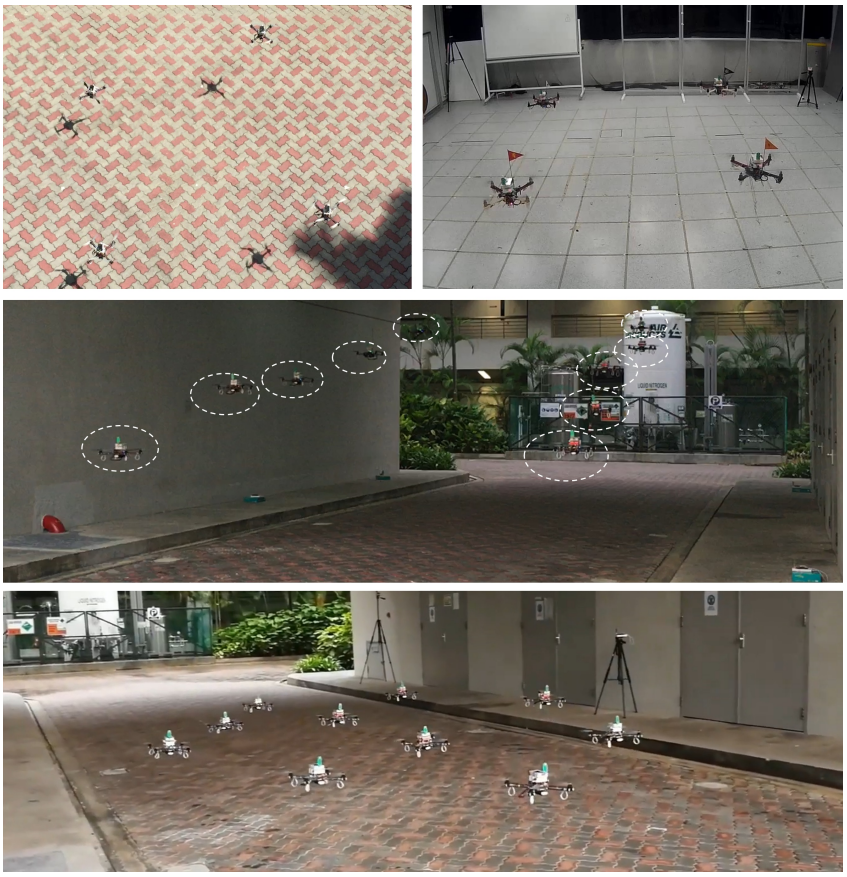

FIGURE 2.6: Flight tests of localization system based on TWTOF UWB ranging techniques in different environments (video recording of these tests can be viewed at https://youtu.be/AUjk5Sk8XXs).

2.1.3 Onboard Perception-Based Localization

Instead of relying on a centralised image processing unit like motion capture system, or requiring artificial anchors to be installed in the environments like wireless positioning approaches, onboard perception-based techniques directly "perceives" the environment and extract the information regarding the MAV position and/or orientation in such environment. Moreover, besides localization function, perception-based techniques also enable obstacles detection/avoidance, mapping, and object recognition capabilities. Enabled by new advances in computation power and portability, vision-based localization methods have attracted a large number of researchers. As such, it has become an integral part in the research and development of autonomous robot systems over the years.

Generally, perception-based localization is a complex process that involves quite a

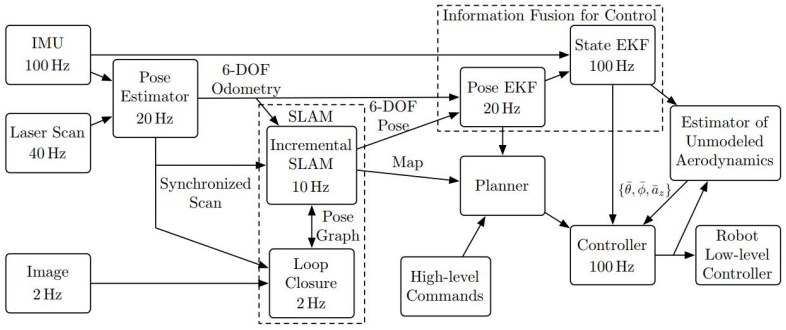

(a) Overview of the system.

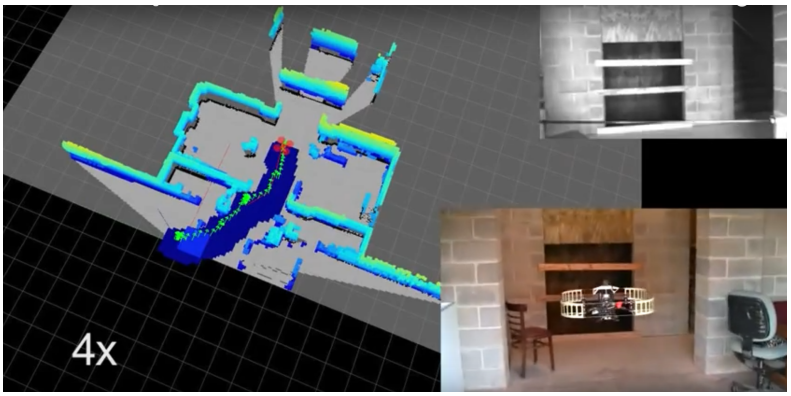

(b) Autonomous navigation and mapping of MAV.

FIGURE 2.7: Autonomous MAV navigation in confined indoor environments using 2D lidar, IMU, and monocular camera by [28].

few types of techniques. For example, to develop a typical *Simultaneous Localization and Mapping* (SLAM) system on an autonomous vehicle, which involves the construction of a map of the environment while simultaneously localizing the vehicle relative to this map, one would have to accomplish several sub-processes such as *feature extraction*, *data association*, *loop closure*, *occupancy mapping*, etc. Specifically, feature extraction is the process of detecting feature points that can persist over successive camera frames without being affected by rotation or translation [58]. Data association is the problem of *determining whether or not two features observed at different points in time correspond to one and the same object in the physical world* [59], hence the translation/rotation of robot can be determined from such change of the features between the camera frames. Loop closure is the process of *deciding whether or not a vehicle has, after an excursion of arbitrary length, returned to a previously visited area* [60], by then the whole trajectory as well as the map can be optimized [61]. Occupancy mapping is the process of providing a volumetric representation of space [62], based on which other navigation processes such as obstacle avoidance, manipulation and path planning can be carried out.

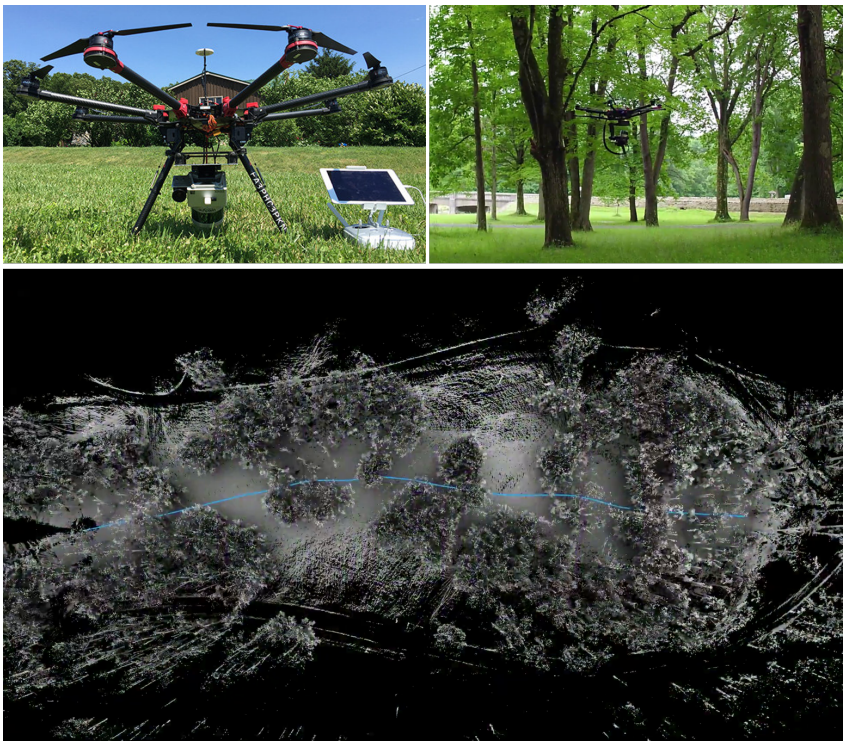

FIGURE 2.8: Visual inertial dometry and mapping with 3D lidar in cluttered environment by [57].

Due to such complexity, achieving all of the aforementioned capabilities would require quite a significant amount of resources. As such, for a resource-constrained system such as MAV, to achieve self-sustained mobility, oftentimes we only focus on the localization issue, and the mapping process can be waived. In that sense, perception-based localization techniques that don't necessarily focus on the mapping aspect are usually referred to as VO in the literature.

Regarding the sensor type, most perception-based localization systems would employ a combination of laser scanner (2D or 3D, also called LIDAR), camera (monocular or stereo camera), and IMU. For example, in [28], a visual odometry system based on 2D LIDAR was combined with IMU and monocular camera was used to achieve autonomous navigation in a building with multiple floor (Figure 2.7). In [57], 3D LIDAR, camera and IMU are integrated into an MAV to map and traverse a cluttered environment at an impressive velocity of 10 m/s. The advantage of using LIDAR for perception and navigation task is that the robot can achieve an accurate scan of the environment with an error of only a few centimeters, thus it can build an accurate map of the environment and the position estimate would have less drift. However, current laser scanners for robots are still quite heavy and

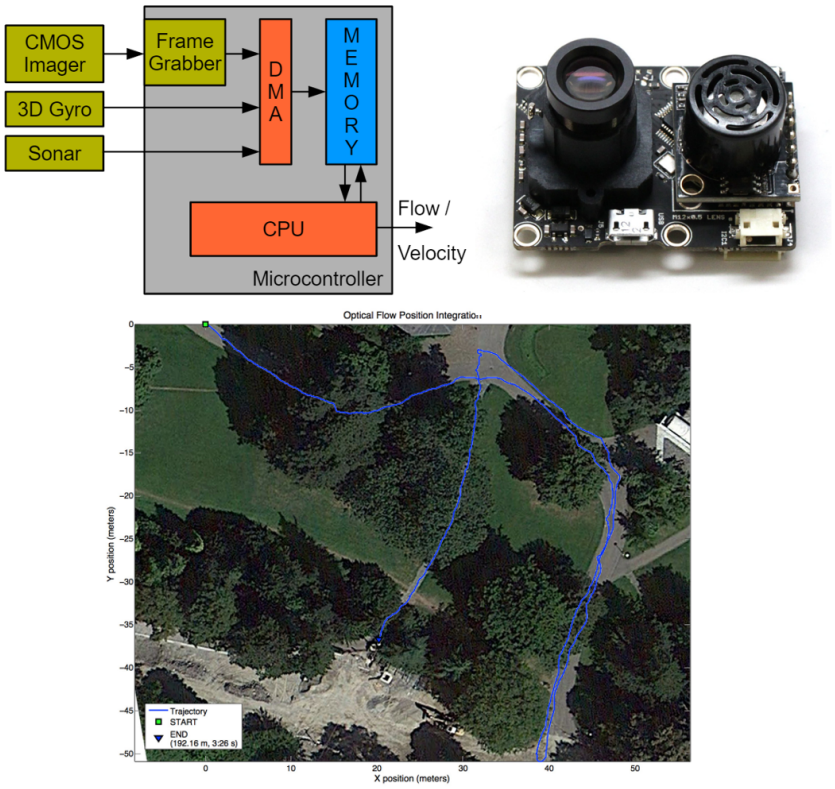

FIGURE 2.9: A low-cost open source visual-inertial odometry (VIO) system by [63] with low estimation drift while operating over a long period of time.

costly, thus they can only be used for MAVs with significant frame size and battery life.

To reduce the weight and cost, other researchers have focused on VO techniques that involve only camera and IMU [31, 63]. Note that since VO systems relying solely on camera for odometry information would be subject to scale ambiguity [64–67], metric IMU information is employed here to help retrieve the scale, which prompts the techniques to be named more specifically as *visual-inertial odometry* (VIO) in the literature. For example, in [63], Honegger et al has developed a minimal VIO system that fits on a single circuit board of a few centimeters. Despite the simplicity, the system demonstrates a high level of reliability and efficiency over a long operation (Figure 2.9). In [31], a robust VIO system is integrated to a small-scale MAV that can perform very aggressive maneuvers. Another direction on stereo vision [68] and multi-camera system [68], which can provide direct metric depth image of the environment, have been gaining more attention for research on VO in recent years.

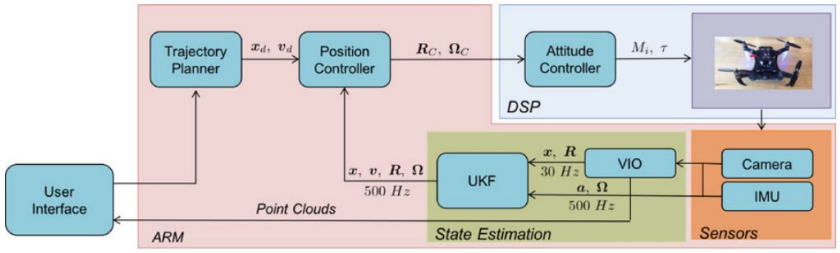

(a) Overview of the system.

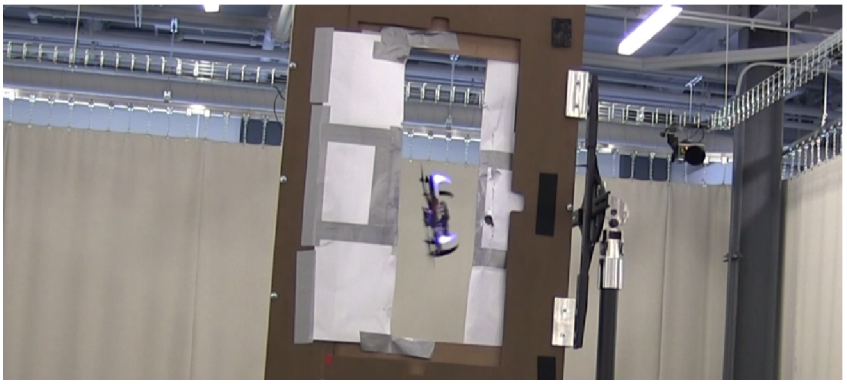

(b) Aggressive maneuver of the small quadrotor with a single camera VIO system.

FIGURE 2.10: Estimation, control, and trajectory planning for aggressive flight of a small quadrotor with single-camera-based VIO by [31].

With the rapid advances in computation power and hardware design, perception-based methods have attracted a large number of researchers over the years. As such, ever higher accuracy and robustness have been reported. However, despite the maturity of the techniques, several issues still exist as intrinsic characteristics of perception-based techniques, namely estimation drift, feature dependence and high computation load, which have to be considered as one seeks to apply these techniques in their specific application. Moreover, as having explained earlier in Chapter 1, since each MAV localizes itself relative to its own local frame of references, they cannot perform some kind of collaborative task without some central processing stations, which motivates the subsequent investigations on using ranging-based techniques for relative localization in this thesis.

2.2 Distance-Based Relative Localization and Navigation of MAVs

2.2.1 Relative Localization and Distance-Based Relative Localization Techniques

As introduced in Chapter 1, relative localization is a crucial requirement for multi-robot systems. Despite its importance, this requirement is still not satisfactorily resolved compared with the self-sustained mobility requirement. In some scenarios, the MAVs can have access to external localization systems such as GPS, motion capture system... and exchange their coordinates to calculate their relative positions. However, the dependence on external systems leads to many restrictions: system can only operate outdoors and have to deal with large positioning error, as with GPS, or are restricted to a limited indoor operation area and require long calibration time along with high maintenance cost as with motion capture system. To overcome these limitations, some researchers have developed onboard sensing techniques to allow MAVs to actively track each other [34–37]. In [34, 35], the authors proposed a relative localization method where agents are equipped with an array of infrared transmitters and receivers to estimate the relative range, bearing and elevation of the two neighbouring agents. However, this method requires quite elaborate hardware that would incur heavy load on the MAV. On the other hand, direct visual tracking methods [36, 37], though accurate and requiring simpler hardware, have limited FOV, is subject to occlusion, lightning conditions and requires that the MAVs have to maintain their sight on their neighbours, thus compromising the versatility and scalability of the system [38].

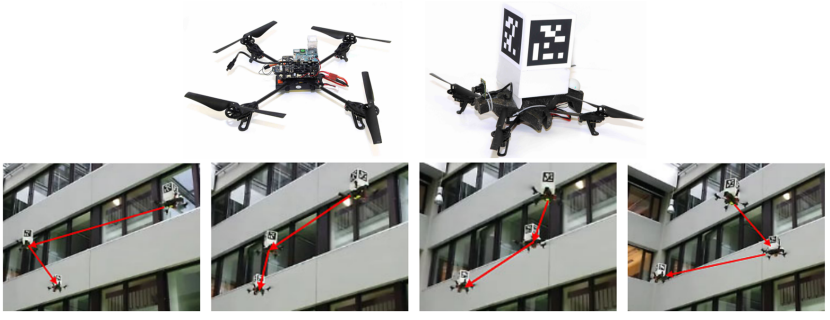

FIGURE 2.11: Direct measurement of relative position using vision and fiducial markers by [36].

Therefore, to achieve the relative localization capability, many researchers have looked into distance-based techniques due to several advantages [38, 69–71]. Compared to relative localization techniques using external localization such as GPS and motion capture system, the distance-based method only relies on a single onboard sensor, thus is not affected by coverage of GPS signal or restricted to a specific location. Also, the issue of limited FOV from vision-based technique can also be avoided with omni-directional ranging techniques [72].

Some related works on distance-based relative localization technique can be found in the literature. Notable works with real-flight experiments can be listed as [38, 69, 71]. In one approach [69], multiple UWB nodes can be installed on the MAV with known offset from the body's center to collect ranging measurements, which are combined with distance measurements to infer the location of the target. Due to constraint on the MAV's size, this scheme may be ineffective beyond a few meters while requiring more sensors. In [71], displacement measurements from the MAV's own motion combined with the distance measurements were used to estimate the relative position to a target. In [38] a heading-independent leader following scheme was proposed by studying the observability of the distance-based localization technique. However in these works the convergence of the relative position estimate is not investigated.

In [73, 74], an estimator derived from the earlier source localization method in [75–78] was proposed to estimate the relative position of the agents by using *distance*, *derivative of distance* and *velocity*. In this scheme, the authors showed that EC can be achieved if the relative velocity $v_{ij}(t)$ between the agents i and j satisfies the PE condition, i.e there exist non-negative constants T and γ such that:

$$\int_{t}^{t+T} v_{ij}(\tau)v'_{ij}(\tau)d\tau \geq \gamma I,\ \forall t \in [0,\infty)\,. \tag{2.5}$$

An intuitive interpretation for the PE condition (2.5) can be given as that at any given interval $[t, t+T]$, the relative velocity $v_{ij}(t)$ must be derived from non-colinear motions in 2D or non-coplanar motions in 3D case. It should be noted that in the works of [73, 74], the requirement of derivative of distance is quite restrictive as there is no direct method to measure it. Although the authors have proposed some extended state observers for this estimation, these methods are quite sensitive to noise in the practical scenario, hence the performance of the

estimation will be degraded. Moreover, these works also only focus on the relative localization issue, and no control strategy was proposed. Hence there is a need to research further onto new methods that can waive the excessive requirements on the types of measurement. Moreover, it is also necessary to investigate how one can integrate such distance-based relative localization method with distributed control schemes and address the requirement for PE condition directly from the control design point of view.

2.2.2 Single Landmark Distance-Based Navigation of MAV

Single landmark navigation is a problem that has been studied extensively in the literature with two related variants under investigations: a circumnavigation problem where an MAV is required to circle around a stationary or moving target [78–82], and a target pursuit or docking problem where an MAV is required to navigate to the prescribed position relative to the fixed landmark(s) [75, 83].

In the first class of problems, for MAVs modeled by unicycle dynamics (fixed-wing type MAV), the distance measurements and the corresponding change rate were employed to tune the heading of the MAV towards/away from the landmark [79–82], while global position and distance measurements are used to estimate the position of the target, upon which a control law is designed to drive the vehicle to the desired circle centered at the target. For the second class of problems, based on adaptive estimation techniques [77, 78, 84] that make use of the global position information and distance measurements to the target, certain kinds of trajectories were designed to drive the vehicle to the target asymptotically [75, 83].

It can be seen that the aforementioned methods may face some challenges in actual implementation. First, the systems in these works are usually formulated in continuous time. Therefore, the theoretical result may no longer hold in implementation when discretization has to be carried out. Moreover, in these works control saturation is often not enforced, which can also pose a risk of overburdening the physical MAV in implementation. Finally, while using distance, some works require extra information on the change rate of distance [79–82], or global position [75, 78], which again limit the practicality of the proposed methods in several scenarios of implementation.

Thus, more research is needed to develop new algorithms that can address the aforementioned limitations. More specifically, the technique should be formulated in discrete-time for more convenience in implementation. In addition, the method should only rely on onboard sensor measurements such as distance and odometry measurements to avoid the dependence on external localization systems.

2.2.3 Autonomous Docking of MAV

Autonomous docking of aerial vehicles has been an active research area over the past decade. In general, it consists of two phases: an approaching phase and a landing phase. Firstly, the MAV needs to locate and navigate towards the target, which can be a landing track, a manned or unmanned ground vehicle, possibly from some distance up to a hundred meters away. Once the MAV is in close proximity of the target, it will try to land in a predefined area. Conventionally, onboard vision systems are widely employed to perform precise landing [85–92] due to their ability to provide accurate positioning information. However, while the landing techniques can be considered mature with the use of vision, it comes to our attention that the approaching problem still lacks a good solution.

In many cases when GPS is available, the approaching capability can be achieved by simply communicating GPS data between the MAV and the target. Recent works have showed that by integrating GPS and vision data, the MAV can land on a vehicle moving at 50 km/h [93], or a fixed-wing aerial vehicle can successfully dock onto a mid-air target [94]. However, this method depends greatly on the availability and the quality of GPS signals, and hence can only be applied in limited scenarios. Specifically, it cannot be applied in city canyons, forests, caves, or deep mines. Other methods have also been proposed under GPS-denied conditions. For example, Kong et. al. [95] proposed a method using a ground-based stereo camera to track and guide the MAV in the landing process. Similarly, Gui et. al. [96] reversed the solution by making MAV carry the camera to detect infrared signals from special lamps installed at the destination. It should be noted that these works are only concerned with landing the MAV on a static target, require a long calibration process and can be easily affected by background lighting conditions. Also they do not entirely resolve the issue when the target is out of view of the MAV, or vice versa. Thus, it can be seen that more research is needed in developing

reliable relative localization and autonomous approaching capability for MAV in both indoor and outdoor conditions.

2.2.4 Distance-Based Adaptive Relative Localization and Control of Multi-MAV Systems

Distributed control of multi-agent systems, which include MAVs, has been a highly active research topic over the years, and a great number of control schemes have been proposed based on relative position [97–104] or relative bearing measurements [105–107], motivated by the need to achieve independence from external localization systems. Nevertheless, the capability to directly measure the relative position or bearing remains a strong assumption from a technological point of view, and it can be seen that only distance-based methods can come close to effectively provide the relative localization capability. Nevertheless, such integration of distance based relative localization method with distributed control scheme still poses a significant challenge. While several strategies on this topic have been proposed over the years [108–111], many limitations still remain at the current stage.

In [108], a stop-and-go strategy was proposed so that each MAV can take turn to optimize a distance-based formation cost function. This implicitly requires an coordinator or coordination strategy that would be ineffective when the number of agents is large. In [109, 112, 113], the authors proposed a relative localization technique using circular motions and Fourier-analysis to calculate the relative position. However, this scheme requires that all MAVs be able to execute very well-defined circular trajectories and can only estimate the relative positions between the centers of these circles. In [111], Han et. al. integrated the relative localization method of Chai et. al. [73, 74, 114] with a formation control scheme. However, in this method, the PE condition was not enforced, thus, non-zero relative localization and formation errors would arise and cannot be eliminated with initial estimation error. In [110, 115], Sarras et. al. proposed a relative localization and target tracking scheme using a different estimator. Specifically, the method in these works employs distance, relative velocity and relative acceleration between the agents, thus waiving the need of derivative of distance. Moreover, the authors also recognize the problem of guaranteeing the PE condition by introducing a PE term in their control law. However, the use of relative acceleration in this case is

equivalent to each agent knowing the control input of its neighbour, which can be quite impractical, especially when the problem is formulated in continuous time. In addition, the relative localization error can converge to zero under PE condition. However, the PE term was introduced as a source of disturbance to the system, hence only bounded tracking error can be achieved. Moreover, it should be noted that the works [102, 110, 110] only focus on continuous systems, and do not consider the issue of input saturation. All of these issues have motivated us to develop an adaptive relative localization technique using only distance and displacement measurements, with a more complete integration of the relative localization techniques under bounded distributed control laws for multi-MAV systems in this thesis.

2.3 Conclusion

In this section, relevant and related research on localization, relative localization, simultaneous relative localization and distributed control of MAVs have been reviewed. It can be seen that many issues still remain unresolved from existing methods in the literature, which motivate the research of this thesis. Specifically, by acknowledging the maturity of perception-based localization methods for self-sustained mobility of MAV, and by recognizing the lacking of relative localization capability in multi-MAV systems, the thesis is dedicated to a course of studies that is ultimately aimed towards cooperative operations of multi-MAV systems in GPS-denied environment, leveraging the latest achievements on VO and ranging-based techniques for relative localization.

Chapter 3

Target-Relative Localization with UWB Ranging and Sensor Fusion

3.1 Introduction

In this chapter, we present a system for target-relative localization by using UWB-based TWTOF sequential ranging and EKF-based sensor fusion techniques. In this scheme, both the target and MAV carry multiple UWB antennae placed in a suitable configuration (Figure 3.1) to provide indirect observations on the relative pose between the two vehicles. We integrate these observations with IMU, altimeter and optical flow data in an EKF to provide accurate and reliable relative position estimates that allow the MAV to track the target. Note that in this work we also focus on experimenting the robustness of the system when the target is moving and the MAV does not know its velocity.

Our main contribution is a complete relative localization system integrating UWB ranging measurements with other standard MAV sensors such as IMU, altimeters and a computationally efficient optical flow, i.e. the *correlation flow*. Unlike the works in [69, 116], our system provides relative position estimates that are sufficiently accurate and stable for feedback-controlled flight and are independent of external systems for localization such as GPS or motion capture system for self-sustained mobility. Additionally, we exploit the UWB communication capability to share information between robots.

This chapter is organized into two main parts. Section 3.2 details the basic features of the system, most notably the sensor models and some pragmatic techniques in our EKF design. Section 3.3 presents the main achievements of our approach with two sets of experiments. The first set demonstrates the ability of the system for omni-directional positioning and the second set demonstrates the robustness of the estimation on the MAV over the unknown target's odometry. As relative position is our main goal, root mean square error (RMSE) and standard deviation (SD) of the relative position estimates are calculated and reported in detail, other data such as orientation and velocity estimate are also presented depending on the context. Finally, we conclude and discuss the potential for future development in Section 3.4.

3.2 Problem Formulation

3.2.1 Overview

Our main goal in this work is to estimate the quadcopter's position relative to the mobile platform, defined as q^E_{QM}, using the main sources of information as illustrated Figure 3.1 (notice the caption for some notational implications). First, multiple UWB nodes are installed on the quadcopter MAV and the mobile platform which can be a manned or unmanned vehicle. For convenience, we call this mobile platform the *target*. The UWB nodes on the target are called the responders and the UWB nodes on the quadcopter are named requesters. We denote the location of a responder i in the frame F_Q fixed on the quadcopter as a^Q_i. Similarly a^M_j is the location of a requester in the frame F_M attached to the target and the relative position between the MAV and the target is denoted as q^E_{QM}. The MAV can measure the distance d_{ij} between a requester i and a responder j via the TWTOF protocol. This measurement is the most important source of observation for localization in our system.

Besides the relative position, in close proximity the orientations of the MAV and target are also critical. In this work, we assume both MAV and target can estimate their orientation relative to an inertial frame of reference F_E. The MAV can receive the measurement of the target's orientation ψ^E_M relative to the inertial frame F_E via the responding messages M_{rspd} in the TWTOF transactions (Figure 3.2).

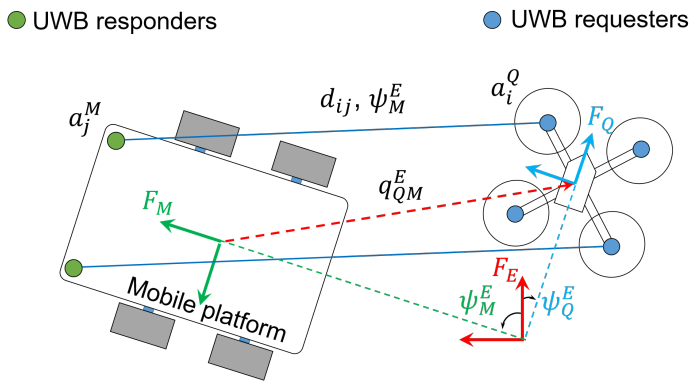

FIGURE 3.1: System overview. In this work, two ranging sensors, each has two separate antennae, are installed on the MAV. Thus, we can effectively count up to four UWB requester nodes. By using different channels, two range measurements can be acquired simultaneously by the two ranging sensors on the MAV. A ranging pattern is pre-programmed on the nodes to cycle through eight useful measurements in four consecutive steps. Note that in q_{QM}^E, the subscript $(\cdot)_{QM}$ is used to indicate that the direction of vector q is from the origin of the frame F_M to the origin of the frame F_Q, and the subscript E is used to indicate that the coordinates are in reference to the frame F_E.

It can be seen in Figure 3.1 that if all of the eight distance measurements d_{ij}, the mobile platform's orientation ψ_M^E, and the MAV's altitude are obtained at the same time, then we can directly calculate the relative position and orientation of the MAV to the target. However, since our ranging method is based on TWTOF, each UWB node can only make response/request to one other node in each transaction. Thus, the quadcopter can only obtain as many range measurements at a time as there are many requesters. In fact, in our system the MAV can only acquire at most two range measurements simultaneously even though four requester nodes are illustrated in Figure 3.1. This is because we can only install two ranging sensors on the MAV and the number of requester nodes are extended by carrying out ranging measurement over spatially separated antennae. Besides unsynchronized observations, measurement noise would also affect the accuracy of the estimate. Thus, the MAV has to carry out some prediction between the arrivals of new measurements and fuse these sources of information asynchronously to obtain a robust estimate for autonomous flight. In our case an EKF is developed for this purpose. The state vector of the quadcopter under this EKF approach is chosen as follows:

$$X \triangleq \mathrm{col}\left\{\psi,\ v,\ q\right\}, \tag{3.1}$$

where the states are defined as follows:

- $\psi = [\psi_w,\ \psi_x,\ \psi_y,\ \psi_z]'$ is the unit quaternion representing the quadcopter's orientation relative to the frame F_E, i.e. ψ_Q^E in Figure 3.1. Here we use the convention where ψ_w is the real part and $[\psi_x, \psi_y, \psi_z]'$ is the imaginary part.
- $v = [v_x,\ v_y,\ v_z]'$ is the relative velocity between the quadcopter and the target in the frame F_E, i.e. v_{QM}^E. Here v_x, v_y, v_z are the Cartesian coordinates of the velocity in the frame F_E.
- $q = [q_x,\ q_y,\ q_z]'$ is the quadcopter's position relative to the target, referenced in the frame F_E, i.e q_{QM}^E. Here q_x, q_y, q_z are the Cartesian coordinates of q in the frame F_E.

Note that $X \triangleq \text{col}\left\{\psi_Q^E,\ v_{QM}^E,\ q_{QM}^E\right\}$ could be a more expressive notation for the state vector, yet as the implications of the subscripts and superscripts can be easily inferred from the context, we opt to omit these extra details to keep the notation concise. With the state vector defined in (3.1), under the EKF paradigm, we can define a state estimate vector $\hat{X} = \text{col}\left\{\hat{\psi},\ \hat{v},\ \hat{q}\right\}$ of the state vector X. Hence, $\hat{X}$ can be updated using the observations d_{ij}, ψ_M^E, a_i^M, a_j^Q whose relationship with X is described in Section 3.2.2. As these measurements are obtained at different rates, an EKF is suitable to fuse all of these observations with other onboard sensors in an asynchronous fusion scheme to robustly estimate the state vector X so that feedback-control flight is sustainable.

3.2.2 Sensor Models

In this part we describe the model of sensors used in our system and discuss some of the important pragmatic measures to successfully achieve a robust estimation of the system states.

3.2.2.1 IMU

IMU is used to mainly estimate the orientation. We denote the data obtained from a IMU as follows:

- $\omega \in \mathbb{R}^3$ is the angular rate from the gyroscope.

- $a \in \mathbb{R}^3$ is the acceleration from the accelerometer.
- $m \in \mathbb{R}^3$ is the earth's magnetic field from the magnetometer.

All of the aforementioned sensor data are in the quadcopter's body frame F_Q. The relationship between ω, a and m with the state vector is described in following differential equations derived from the kinematics of a *strapdown inertial navigation system* [117, 118]:

$$\dot{\psi} = \frac{1}{2}(\psi \circ \psi_\omega), \tag{3.2}$$

$$\dot{v} = R_Q^E(\psi)a - \mathbf{g} - \dot{v}_M^E, \tag{3.3}$$

$$\dot{q} = v, \tag{3.4}$$

$$m = R_E^Q(\psi)\mathbf{m}, \tag{3.5}$$

where $(\circ)$ denotes the quaternion multiplication, ψ_ω is the quaternion with zero in the real component and the angular rate ω in the imaginary part, $R_Q^E(\psi)$ is the rotation matrix constructed from the quaternion ψ and $R_E^Q(\psi)$ is its inverse, $\mathbf{g}$ is the Earth's gravity, v_M^E is the velocity induced by the translation and rotation of the frame F_M (we assume these motions are small enough so that $\dot{v}_E^M$ can be considered as a process noise), and finally $\mathbf{m}$ is the direction of the Earth's magnetic field in the inertial frame F_E.

Notice that equations (3.2), (3.3), (3.4) are used for prediction while (3.5) is for the correction stage. Moreover, the gyroscope biases in the IMU measurements are also accounted for by introducing extra states beside the ten main states in (3.1). We will update the state estimate $\hat{X}$ of X using the discretized and linearized versions of the differential equations (3.2), (3.3), (3.4). These tasks follow quite well-established procedures in implementation of strapdown inertial navigation system [118–120], thus the details are ommited for the sake of brevity.

3.2.2.2 Orientation-Coupled Range Measurements

Figure 3.2 illustrates a TWTOF transaction in our system. As can be seen in this diagram, the distance between the requester and responder nodes can be calculated using the TWTOF model as follows:

$$d = c\frac{t_2 - t_1 - \delta}{2} - \Delta, \tag{3.6}$$

where c is the speed of light, t_1 and t_2 are the time instances when the request and responses messages are recorded on the requester's clock respectively, δ is a predefined period that the responder has to wait before responding, Δ is the gross distance bias due to electronic delays in the extension cables and connectors. This constant Δ has to be measured empirically for each pair of a requester and a responder.

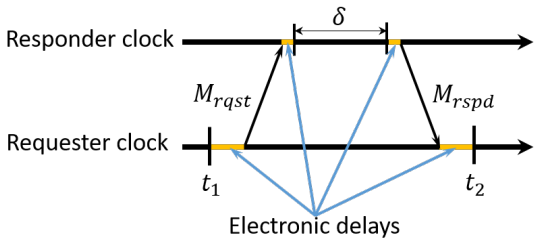

FIGURE 3.2: A diagram of TWTOF ranging protocol.

We can now state the relationship between the UWB measurement and our selected state vector X. Denote $||.||$ as the Euclidean norm of a vector in $\mathbb{R}^3$, the relationship between our measurement and state vector can be stated as follows:

$$d_{ij} = \left\| q + R_Q^E(\psi) a_i^Q - R_M^E(\psi_M^E) a_j^M \right\|, \tag{3.7}$$

where $R_Q^E(\psi)$ is the direct cosine matrix (DCM) constructed from the quarternion states ψ, and $R_M^E(\psi_M^E)$ is the DCM constructed from the orientation representation of the target's frame F_M relative to F_E.

We can see that the distance measurement couples both the position and orientation of the MAV. Thus, one advantage of having multiple requester nodes and at least two responder nodes in Figure 3.1 is that we can disambiguate the orientation of the MAV from the distance observation. Otherwise the yaw can very often drift if there is only a single UWB requester node on the MAV or a single requester node on the target.

3.2.2.3 Optical Flow

In this work, we employ the recently proposed optical flow algorithm, *kernel cross-correlator*-based *correlation flow* [121], to obtain an accurate velocity estimation.

It is open source[1], computationally efficient and robust to motion blur. The key feature of our method is the use of kernel cross-correlator to efficiently predict the transformation in Fourier domain between the current and previous image, including translation, rotation, and scale. After this operation, the position of the highest value in the correlation output will identify the most suitable translation, rotation and vertical movements of the camera between two frames. In this work we only use a simple model of 2D translational optical flow with the following measurement model:

$$\begin{bmatrix} v_{f_x} \\ v_{f_y} \end{bmatrix} = \begin{bmatrix} 1 & 0 & 0 \\ 0 & 1 & 0 \end{bmatrix} \frac{1}{q_z} R_E^Q(\psi) v. \tag{3.8}$$

The current implementation assumes that the camera's image plane is always parallel with the ground plane. Therefore the use of $R_E^Q(\psi)$ in the model (3.8) is not an exact description. However, as the MAV's angles are given some threshold (which is to limit the maximum speed), the effect of roll and pitch is minor and can be lumped to the process noise. This approach has been validated in actual autonomous flight tests with only one camera, IMU and onboard altimeters. The video recording of this test can be viewed online[2].

3.2.2.4 Altimeters

For altitude estimation a laser range finder and barometer data are used to measure the distance from the MAV to the floor at an angle. The relationship between the laser range finder reading l and the state vector can be stated as follows:

$$l = \frac{q_z}{\psi_w^2 - \psi_x^2 - \psi_y^2 + \psi_z^2}, \tag{3.9}$$

where q_z is the altitude of the MAV in the frame F_E and the denominator on the right hand side of (3.9) is the cosine of the angle between the vectors with coordinates $(0,\ 0,\ 1)$ in both F_E and F_Q frames.

[1] https://github.com/wang-chen/correlation_flow
[2] https://youtu.be/DEjwjzJX3b4

The barometer reading b is directly related to the altitude q_z with an offset b_0 as follows:

$$b = q_z + b_0. \tag{3.10}$$

3.2.3 Asynchronous Fusion

In this section we describe the workflow to fuse multiple sensor data described in previous parts. Algorithm 1 summarizes the main operations of this fusion thread.

Algorithm 1 EKF - Asynchronous fusion

while Thread is healthy **do**
  Poll_sensor_data()
  if New sensor data available **then**
    if New gyroscope and accelerometer data **then**
      Predict_orientation_velocity(ω, a)
    end if
    if New magnetometer data **then**
      Fuse_magnetometer(m)
    end if
    if New UWB data **then**
      Fuse_UWB_distance(d_{ij}, a_i^Q, a_j^E)
    end if
    if New correlation flow data **then**
      $v_{f_z} = [0, 0, 1]' R_E^Q(\hat{\psi})\hat{v}/q_z$
      $v = q_z R_Q^E(\hat{\psi}) \left[v_{f_x}, v_{f_y}, v_{f_z}\right]'$
      Fuse_velocity(v)
    end if
    if New laser range finder data **then**
      $h = l(\hat{\psi}_w^2 - \hat{\psi}_x^2 - \hat{\psi}_y^2 + \hat{\psi}_z^2)$
      Fuse_altitude(h)
    end if
    if New barometer data **then**
      $h = b - b_0$
      Fuse_altitude(h)
    end if
  end if
end while

As the sensors are managed by different threads with different update rates, the data from these sensors are not synchronized. Hence, in our fusion scheme, a fusion thread will keep polling for new sensor data and corresponding stages of prediction/update will be selected according to the sensor type. Note that in steps

4 to 25 of Algorithm 1, discretized versions of equations (3.2), (3.3), (3.4), (3.5), (3.7) and (3.8) are linearized to predict/update the state estimate and the error covariance matrix in a canonical way. However in steps 13 to 21, we pragmatically ignore the mathematical coupling of the observation with the orientation states. Specifically, for the optical flow estimate, we first convert the current velocity estimate to the body frame and scale it by the MAV's altitude estimate to obtain a so-called *artificial flow* (step 14). The z component of this *artificial flow* is thus extracted and combined with the 2D optical flow data from camera to form a 3D *augmented flow* measurement (step 15). This *augmented flow* vector is then used to produce an approximation of velocity measurement in the inertial frame F_E by multiplying it with $R_Q^E(\hat{\psi})$ and the altitude estimate. This approach helps reduce unnecessary computation given that the MAV's attitude is not supposed to vary too much and any error can be lumped to the process noise. The same rationale is applied to the treatment of the laser range finder for the altitude observation in step 19. The success of our flight tests would validate this pragmatism in retrospect.

3.3 Experiments

3.3.1 Setup

In this part we will describe in detail the physical implementation of our system. Video recording of our experiments can be found at `https://youtu.be/5zelvj_xPzM`. The datasets collected from these experiments can be downloaded at `https://github.com/BritskNguyen/icra2018_uwb_sensor_fusion`.

Figure 3.3 shows the main components in our experiments. On the target's side, two UWB radios are used as responders in ranging and communication transactions (we notice that a ranging error below $2cm$ is reported by the manufacturer for the latest version[3]). These radios are hosted by a small-size embedded computer whose main job is to query the orientation data from a low-cost IMU module comonly used in robotics research[4]. This IMU data is then relayed to the UWB radio's buffer to be included in the response messages of the TWTOF ranging transaction.

[3] `http://www.timedomain.com/products/pulson-440/`
[4] `http://wiki.ros.org/myahrs_driver`

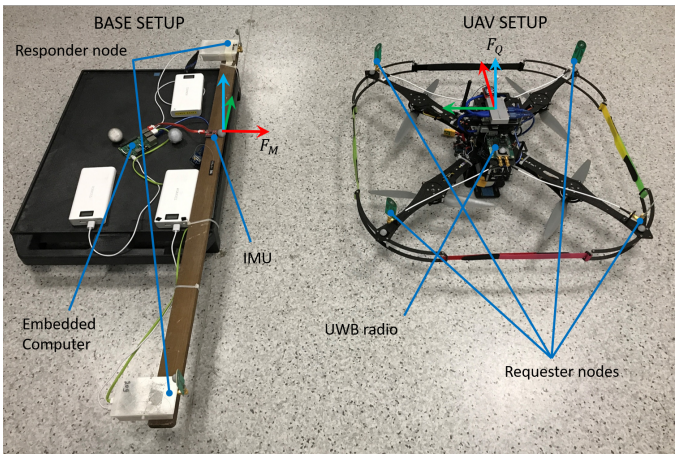

FIGURE 3.3: Actual equipment used in the experiments.

On the MAV's side, there are also two UWB radios but each uses two antennae, thus a total of four requester nodes are presented. The sensor's driver provides complete support to select which antenna to be used in each ranging transaction. Hence, in our setup, we can configure two requester nodes to range to two responder nodes simultaneously using different UWB channels (easily selectable by the sensor's API), then change the antennae to obtain another set of observation. In total, eight distance measurements from every pair of requester and responder can be obtained over a 0.116s long cycle using this switching scheme. We can say that ranging measurements are obtained at a rate of approximately 70Hz. The optical flow data is obtained at 30Hz, IMU data at 100Hz and laser range finder data is at 40Hz. The target's data sent over UWB signal is configured at 10Hz and Vicon data is received at approximately 35Hz. The antennae on the MAV are installed at the corners of a $0.55m \times 0.55m$ square centered around the origin of the frame F_Q. The quadcopter is equipped with another embedded computer board, referred to as the high-level board. The computer board has two main tasks. The first task is to organize and collect the UWB range measurement and the second task is to process the camera's image to produce the optical flow data. The high-level board will then send these measurements to a flight control computer (FCC) where the EKF is implemented. The FCC will fuse this information with data from other onboard sensors such as IMU and laser range finder in the EKF and use this estimate in the control loop. All data used for analysis are collected and stored by the high level board including the EKF estimate sent back by the FCC, the ground truth data sent over zigbee from a Vicon system and the target's information is sent over the UWB messages.

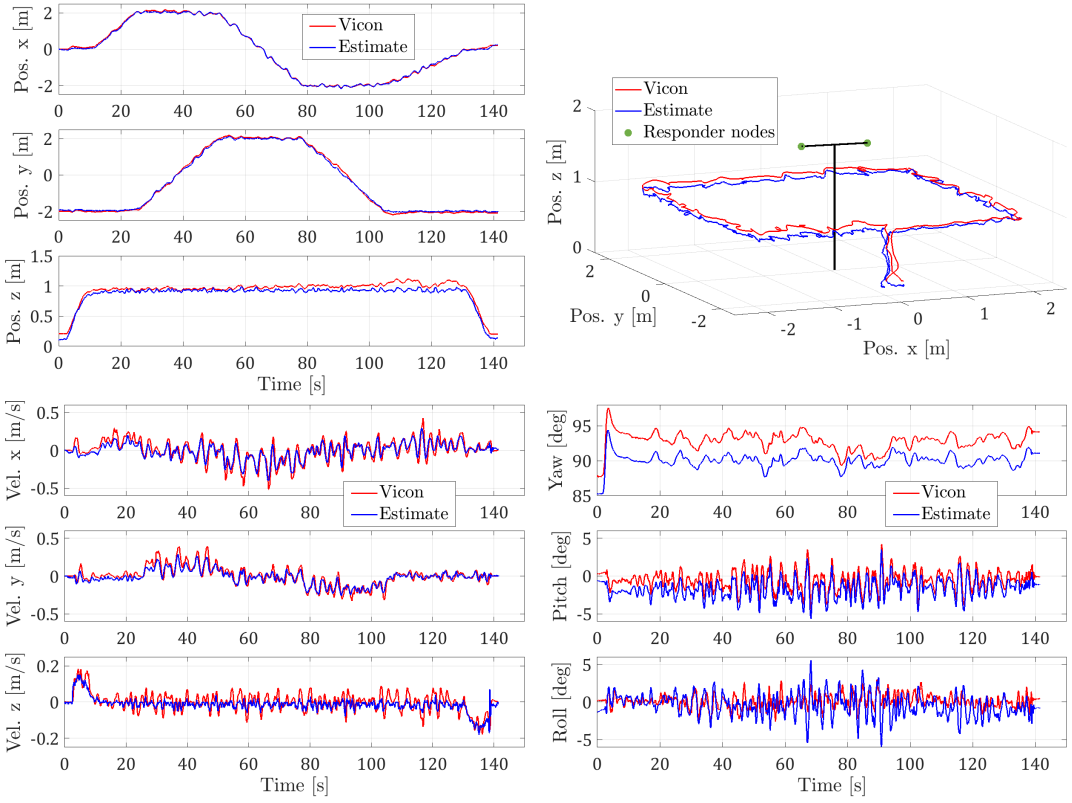

FIGURE 3.4: A static anchor experiment: The MAV follows a predefined path of a $4m \times 4m$ square at $0.9m$ altitude around the two static responders. All data are in reference to the frame F_E. The responders' coordinates in the frame F_M are $(0.04, -0.57, 1.753)$ and $(0.035, 0.424, 1.778)$, which means the two repsonder nodes are only separated for approximately 1 meter apart.

3.3.2 Static Target Experiments

In this section we demonstrate the MAV's omni-directional positioning relative to the target. In these so called static target tests, the MAV repeats a trajectory of a $4m \times 4m$ square defined in the frame F_E at different altitudes. Figure 3.4 shows the results of the test at $0.9m$ altitude. First, the 3D plot of the flight path is presented, then estimates of position, velocity and euler angles compared with ground truth over time are shown in Figure 3.4.

We take the Vicon data as the ground truth to calculate the relative position state q^E_{QM}. Based on this, we calculate the relative position estimation error $\tilde{q} = \hat{q} - q^E_{QM}$ and report the *root mean square* (RMS) and *standard deviation* (SD) of the positioning error in Table 3.1. Recording of one of these flight tests can be viewed at the begin of the video uploaded to the online link[5].

[5] https://youtu.be/5zelvj_xPzM

TABLE 3.1: RMS and SD of relative position estimation error $\tilde{q}$ with static anchor at different altitudes (unit: m).

Altitude	rms($\tilde{q}_x$)	rms($\tilde{q}_y$)	rms($\tilde{q}_z$)	sd($\tilde{q}_x$)	sd($\tilde{q}_x$)	sd($\tilde{q}_x$)
0.6m	**0.053**	**0.094**	**0.070**	0.044	0.094	0.025
0.9m	**0.043**	**0.074**	**0.074**	0.040	0.074	0.038
1.2m	**0.054**	**0.086**	**0.139**	0.049	0.084	0.032

Due to space constraints, we cannot carry out the same test where the MAV flies around the responder nodes on a larger square. However we are still interested in finding out to which extent localization is still robust. Thus, we shift the responder nodes approximately 3.5m forward in the y direction of the frame F_E. and let the MAVs fly at $0.6m$ altitude. Thus the maximum distance from the MAV to the responders can be up to 5m. Figure 3.5 shows the paths made by the MAV in these experiments. Similar to the near-anchor tests, the same statistics on the relative position estimates are obtained and reported in Table 3.2.

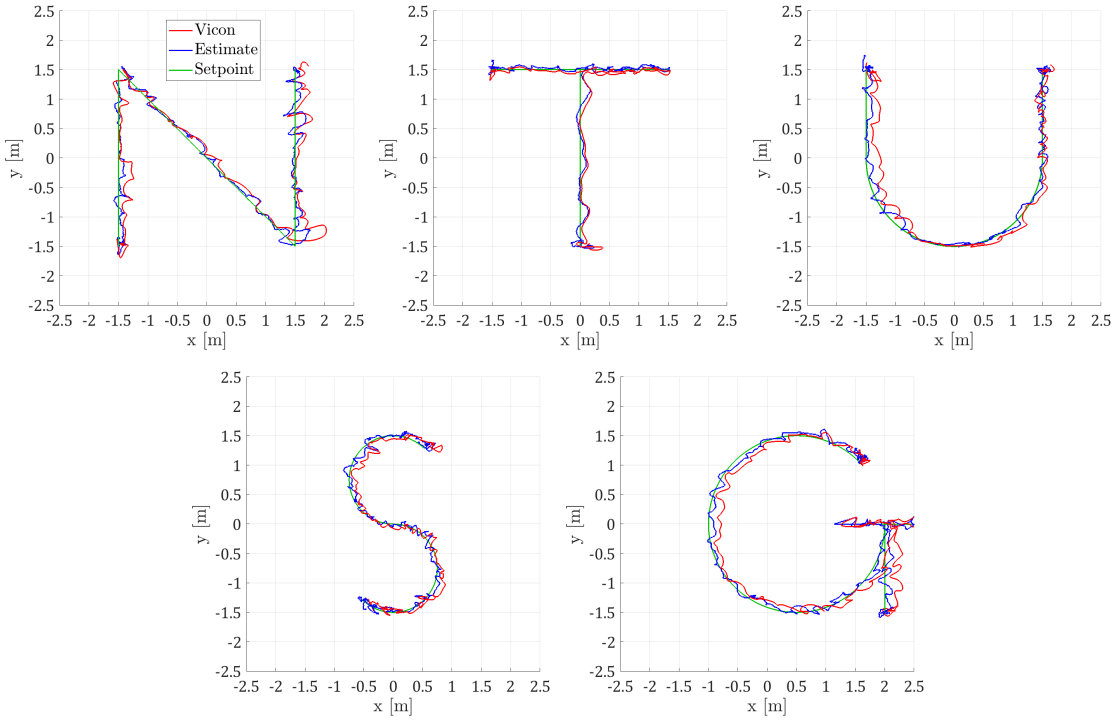

FIGURE 3.5: Result of static target experiments where MAV follows predefined trajectories with the static responder nodes shifted further away to the new locations $(0.369,\ 3.474,\ 1.733)$ and $(-0.625,\ 3.461,\ 1.77)$ in the frame F_E.

These flight tests have demonstrated that our localization system can actually achieve reliable localization data in all directions around the static responder nodes. We also show that our localization is still reliable at a distance up to 5m away from

TABLE 3.2: RMS and SD of relative position estimate error $\tilde{q}$ in the far-anchor experiments (unit: m).

Exp.	rms($\tilde{q}_x$)	rms($\tilde{q}_x$)	rms($\tilde{q}_x$)	sd($\tilde{q}_x$)	sd($\tilde{q}_x$)	sd($\tilde{q}_x$)
1	**0.094**	**0.040**	**0.029**	0.069	0.040	0.025
2	**0.061**	**0.044**	**0.093**	0.047	0.020	0.016
3	**0.112**	**0.068**	**0.078**	0.069	0.042	0.022
4	**0.099**	**0.040**	**0.074**	0.041	0.018	0.023
5	**0.123**	**0.046**	**0.084**	0.063	0.046	0.019

the target with a relatively small spacing of 1m between the responders and $0.55m$ spacing between the requesters. Moreover, the small angle assumption in dealing with correlation flow data is also verified as can be seen in Figure 3.4 where the maximum value of the roll and pitch angles are mostly below 5^o in absolute value.

3.3.3 Moving Target Experiments

Four flight tests are carried out in this experiment. For the first three experiments, so-called *translating target experiments*, the change in the target's orientation is kept relatively small as it moves around. The MAV is set to maintain a fixed position relative to the target. Video recording of these tests can be viewed at the online link[6]. The paths of the target and the MAV are plotted together in Figure 3.6.

In Figure 3.7, we show the velocities of the target recorded by Vicon along with the MAV's velocity estimate in the third *translating target experiment* as the target moves at highest speed in this test, which is around 0.4m/s in Figure 3.7. It can be seen that the velocity estimate does not change very much around zero as the relative position is always maintained.

TABLE 3.3: RMS and SD of the relative position estimation error $\tilde{q}$ in moving anchor experiments (unit: m).

Exp.	rms($\tilde{q}_x$)	rms($\tilde{q}_x$)	rms($\tilde{q}_x$)	sd($\tilde{q}_x$)	sd($\tilde{q}_x$)	sd($\tilde{q}_x$)
1	**0.062**	**0.023**	**0.035**	0.059	0.018	0.023
2	**0.081**	**0.047**	**0.072**	0.064	0.039	0.021
3	**0.097**	**0.048**	**0.076**	0.028	0.020	0.019
4	**0.132**	**0.065**	**0.081**	0.132	0.047	0.020

[6] https://youtu.be/5zelvj_xPzM

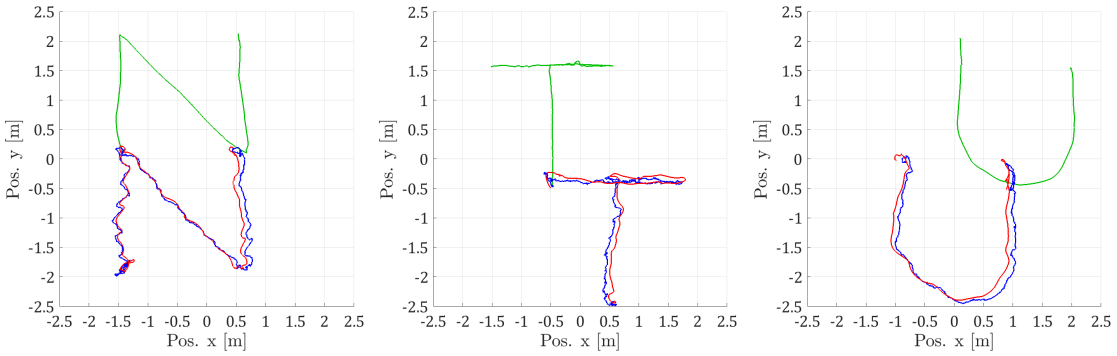

FIGURE 3.6: Target tracking experiments: The MAV is set to maintain fixed relative position with the target. The target's path recorded by Vicon is plotted in green and the MAV's path is plotted in red. The MAV's relative position estimate is offset by the target's position and displayed in blue. The responders' coordinates in the frame F_M are still separated from each other for about 1m and the values measured by Vicon are $(-0.019\ 0.700\ 1.428)$ and $(-0.012\ -0.338\ 1.419)$ respectively. It can be seen that the trajectories made by the MAV are similar to the target's path, which demonstrates the ability of the MAV to robustly estimate and maintain its relative position to the target.

In the fourth experiment, so-called *rotating target experiment*, a more complicated task is performed where the setpoint is updated by $R_E^M(\psi_E^M)\,[0, -2, 0.75]'$. This means that instead of maintaining a fixed position relative to the target, the MAV now has to change its relative position to make sure that it hovers at 2m "behind" the target's center. This resembles when the MAV has to land on a specific side of the UGV where the landing pad is.

Table 3.3 summarizes the statistics of the relative position estimation error in these experiments. Figure 3.8 shows the absolute error of the relative position estimate of the rotating target experiment as it has the largest RSME. We can see that the maximum error in any direction is approximately 0.25m, thus the absolute 2D localization error of relative positioning in the moving target experiment can be declared as 0.35m.

3.4 Conclusion

In this chapter we have developed a system for relative positioning between a quadcopter and a cooperative target using UWB distance measurements and several other onboard sensors. We showed that our use of UWB range measurement can achieve omni-directional relative position estimates that are reliable enough to

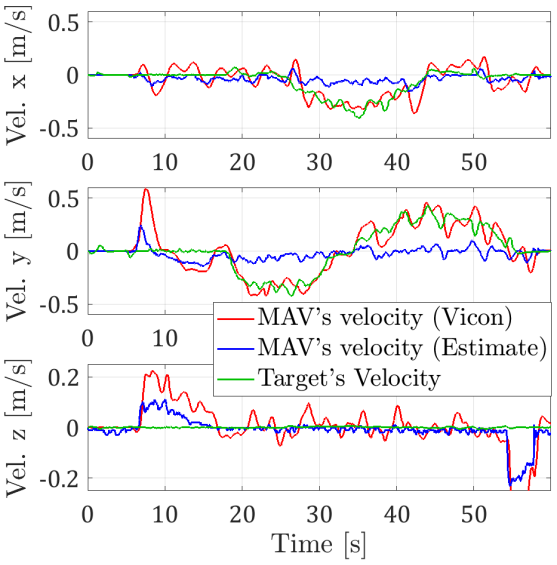

FIGURE 3.7: Velocities of the target and relative velocity estimate by the MAV in the third experiment. We can also see that the maximum velocity of the target is about 0.4 m/s and the MAV's actual velocity follows the velocity of the target, which renders the relative position estimate maintained around zero. From Figure 3.6 and the recorded video it can be seen that the MAV can maintain the relative position quite well. This demonstrates the robustness of the target-relative localization scheme even when the target's velocity is unknown.

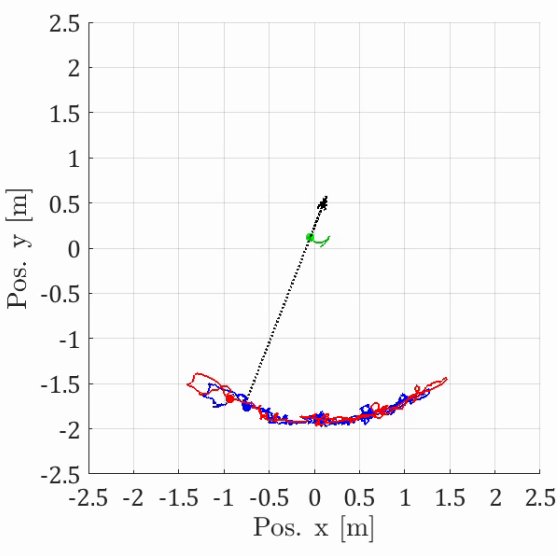

FIGURE 3.8: Trajectory of the MAV (red) and its position estimate (blue) when the relative position setpoint is updated according to the heading of the target. The position and trajectory of the target are respectively marked by the green dot and the green line, and its heading according to its attached IMU is shown by the small black arrow. The position and trajectory of the MAV are respectively marked by the red dot and red line, and their coresponding estimates are marked in red. The absolute error of relative position estimate in the rotating target experiment over time is shown in Figure 3.9.

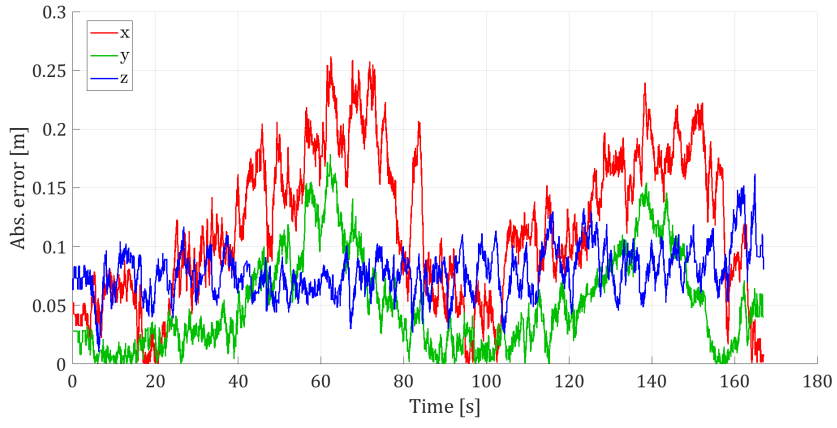

FIGURE 3.9: The absolute error of relative position estimate in the rotating target experiment over time. It can be seen that the maximum estimation error in any direction is below 0.25 m during the whole test.

support feedback-controlled flight, which allows the MAV to autonomously track a moving target. The results presented in this chapter serve as an important basis for next developments on precision landing and collaborative operations in the next chapters.

Chapter 4

Single Landmark Distance-Based Adaptive Navigation of MAVs

4.1 Introduction

In the previous chapter, we have developed a technique for relative localization using EKF and demonstrated that the method can achieve robust and efficient target tracking capability. However, this method is only effective in a close range scenario as the EKF requires an accurate initialization of the state estimate, otherwise it can fail to converge. While we can use some algebraic techniques such as trilateration [12] or nonlinear regression [13] to calculate the initial relative position using a few intial distance measurements at a close range, the accuracy of these techniques will be significantly degraded at a large distance [122]. Hence, we need to develop a new technique to drive the MAV to the target to resolve this issue.

To this end, we will investigate such a method in this chapter. We will assume that the MAV can achieve self-sustained mobility from some VO method, and by using the displacement from the VO system together with distance measurement to the target, the MAV can estimate its relative position and approach the target under some control law. Moreover, we further simplify the requirement of the UWB nodes to a single pair of requester and responder on the MAV and the target respectively, hence increasing the flexibility of the system.

An integrated localization-navigation scheme is developed for the aforementioned operation: we propose an adaptive estimation scheme to estimate the relative position to the landmark, and also delicately design a control scheme to ensure asymptotic convergence of the estimation as well as the navigation objectives. Motivated for practical implementation, we consider a discrete-time formulation and control input saturation. By employing adaptive control techniques and the discrete-time LaSalle's invariance principle, the convergence of the overall localization-navigation scheme is rigorously established. We also discuss the stability under distance measurement error and extend the navigation scheme to arbitrary locations relative to the landmark.

Some related works can be found in [75, 78–83] with a similar premise. Note that in this chapter we adopt a similar naming of the navigation objective as *docking* from [75]. In comparison with the related works [75, 83], in this thesis we only use distance and odometry measurements without requiring absolute position information. This change in the required measurements is quite important as it allows the algorithm to be readily compatible with operation in GPS-denied environments, where accurate displacement and distance measurements can be obtained from onboard sensors such as VIO system and UWB sensors. In addition, we also consider the issue of control input saturation which was not addressed in many previous works. Finally, we implement the proposed scheme on quadcopters and conduct experiments to validate the theoretical findings and applicability of the proposed scheme.

This chapter is organized as follows: after introducing the problem formulation along with the dynamics and sensor models in Section 4.2, we proceed to propose the distance-based relative localization and control laws in Section 4.3. We then provide the analyses on stability and convergence of the docking task in Section 4.4. We put forth some discussions on more practical scenarios with relative docking as well as influence of noise in Section 4.5. Simulation and experiment results are respectively provided in Sections 4.6 and 4.7 to validate the theory and demonstrate the practicality of the proposed algorithm. We conclude the chapter by Section 4.8.

4.2 Problem Statement

Given a landmark arbitrarily deployed at an unknown position p^*, the docking problem is solved if we can design a control law to achieve the following objective:

$$\lim_{k\to\infty} p(k) = p^*, \tag{4.1}$$

where $p(k) \in \mathbb{R}^m,\ m \in \{2, 3\}$ is the MAV's position in the same frame of reference of p^*. The MAV is modeled as a discrete-time integrator with bounded velocity as follows:

$$p(k+1) = p(k) + T\bar{u}(k),\ \|\bar{u}(k)\|_\infty \le U, \tag{4.2}$$

where T is the sampling period and U is the maximum velocity. Clearly, for any control input $u(k)$, the bounded velocity requirement can be satisfied by letting $\bar{u}(k) = \pi_U(u(k))$, where $\pi_U(\cdot)$ is a projection operator onto the ball $\bar{\mathcal{B}}(0, U)$ defined as follows:

$$\pi_U(u(k)) \triangleq s_U(u(k))u(k),\ s_U(u(k)) \triangleq U/\max\{U, \|u(k)\|\}. \tag{4.3}$$

In the sequel, we also write $s(k) = s_U(u(k))$ for conciseness.

Remark 4.1. *To convey the main ideas more efficiently, we model the MAV as a discrete-time single integrator with bounded velocity. In the literature, MAVs are usually modeled with double integrator dynamics. However, it should be noted that we have intentionally imposed a bounded input constraint $\bar{u}_i(k) \le U$ in the dynamics (4.2). Thus, under an acceleration-controlled double integrator dynamics, one can use control techniques such as optimal control, model predictive control to find an input that drives the MAV from $p(kT)$ to $p(kT) + T\bar{u}(k)$. As $T\bar{u}(k)$ is bounded, a feasible solution would exist given sufficiently large bound for acceleration input.*

In navigation, the MAV can obtain two types of measurements: distance measurement $d(k)$ and displacement $\phi(k)$, whose definitions and some mathematical relationships with other quantities are stated as follows:

$$d(k) \triangleq \|q(k)\| = \|p(k) - p^*\|, \tag{4.4}$$

$$\phi(k) \triangleq p(k+1) - p(k) = q(k+1) - q(k) = T\bar{u}(k), \tag{4.5}$$

where $q(k) \triangleq p(k) - p^*$ is the position of the MAV relative to the landmark and the equality $\phi(k) = T\bar{u}(k)$ is a result of the dynamics (4.2).

Remark 4.2. *It should be pointed out that the displacement $\phi(k)$ is obtained from onboard sensors, rather than from differentiating two consecutive absolute positions. Specifically, with the mature development of VO or SLAM techniques, it can be obtained accurately by calculating displacement of visual features in two consecutive camera image frames. In the experiment later we obtain $\phi(k)$ from a generic commercial optical flow sensor which operates in the same principle with VO techniques.*

4.3 Adaptive Navigation Scheme

In this section we shall design an integrated localization and navigation scheme to simultaneously solve the relative localization and docking problem. To be detailed, as shown in Figure 4.1, an adaptive estimator based on distance and odometry measurements is designed to achieve the relative localization, then based on which $\bar{u}(k)$ is designed in a particular form to solve the docking problem (4.1). See the next two subsections for details.

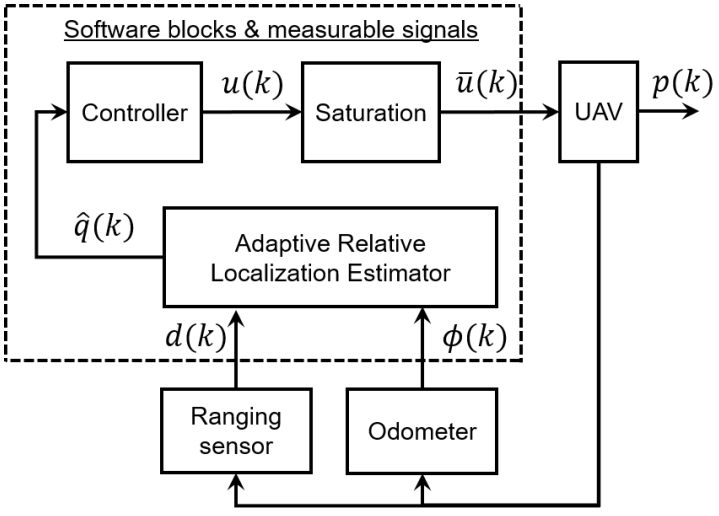

FIGURE 4.1: An integrated localization-navigation scheme.

4.3.1 Adaptive Estimator for Relative Localization

From (4.4) and (4.5) we get the following equality:

$$\begin{aligned} d^2(k) - d^2(k-1) &= \|q(k-1) + \phi(k-1)\|^2 - \|q(k-1)\|^2 \\ &= \|\phi(k-1)\|^2 + 2\phi'(k-1)q(k-1). \end{aligned}$$

Now we can define the following parametric model

$$\zeta(k-1) = \frac{1}{2}\left[d^2(k) - d^2(k-1) - \|\phi(k-1)\|^2\right] = \phi'(k-1)q(k-1). \tag{4.6}$$

Let us denote $\hat{q}(k)$ as the estimate of the relative position $q(k)$ and $\epsilon(k-1) = \zeta(k-1) - \phi'(k-1)\hat{q}(k-1)$ as an observation innovation. The following law is used for updating the relative position estimate $\hat{q}(k)$ when new measurements are obtained:

$$\hat{q}(k) = \pi_{d(k)}\left(\hat{q}(k-1) + \phi(k-1) + \gamma\phi(k-1)\epsilon(k-1)\right),\ \gamma > 0. \tag{4.7}$$

Remark 4.3. *Note that in (4.7), the projection operation $\pi_{d(k)}(\cdot)$ is used to enforce the relationship $\|q\|(k) = d(k)$ in updating the relative position estimate $\hat{q}(k)$. Effectively, this operation will "scale down" the estimate $\hat{q}(k)$ when its norm is larger than the observation $d(k)$, thus bringing it closer to the true value $q(k)$ and increase the convergence rate, which is explained in more details in the proof of Proposition 4.1.*

4.3.2 Bounded Control Law for Navigation

4.3.2.1 Control Law

Based on the estimator (4.7), the following controller is proposed to solve the docking problem (4.1):

$$\bar{u}(k) = \pi_U(u(k)),\ u(k) = -\beta\hat{q}(k) + \alpha d(k)\sigma(k),\ \alpha,\ \beta > 0, \tag{4.8}$$

where $\sigma(k) \in \mathbb{R}^m$ is an internal signal generated by an autonomous system as follows:

$$\begin{cases} \rho(k+1) = \Pi(\rho(k)); \\ \sigma(k) = \Sigma(\rho(k)); \ k = 0, 1, 2, \dots; \end{cases} \tag{4.9}$$

where Π and Σ are two continuous mappings chosen to satisfy the following assumptions:

Assumption 4.1.

i. $\Pi \colon \mathcal{S} \to \mathcal{S}$ *with* $\mathcal{S} \subseteq \mathbb{R}^n$ *being compact.*

ii. $\bar{\sigma} = \sup\{\|\sigma(k)\|, k = 0, 1, \dots\} \leq 1$.

iii. There exists $K \in \mathbb{N}$ *such that* $\sigma(k + K) = -\sigma(k), \forall k \in \mathbb{N}$*; moreover,* $\text{span}\{\sigma(k) \colon k = 0, 1, \dots, K-1\} = \mathbb{R}^m$.

Remark 4.4. *Note that the control law (4.8) consists of two terms: the first term is essentially a linear movement towards the landmark* p^* *if there is no estimation error, i.e.* $q(k) \equiv \hat{q}(k)$*, and the second one represents an oscillatory movement if* $d(k) \equiv d^* > 0$ *with* $\sigma(k)$ *generated by (4.11). Furthermore, in the absence of the first term, the second term is related with the PE condition [123], and a large* α *implies a faster convergence for the estimator.*

4.3.2.2 Design of the autonomous excitation:

In the design of the control law (4.8), it has been stated that σ needs to be generated from an autonomous process, which is necessary for the LaSalle's invariance principle to be invoked. Thus, in this part we will discuss some specific choices of Σ and Π for the case of $m = 2$ and $m = 3$, respectively corresponding to the cases of 2D and 3D localization. In both cases we take $\mathcal{S} = \{\rho = [\rho_1, \rho_2]' \in \mathbb{R}^2 \colon \|\rho\| = 1\}$, and define Π to be a matrix operator as follows

$$\Pi = \begin{bmatrix} \cos\omega & -\sin\omega \\ \sin\omega & \cos\omega \end{bmatrix}, \tag{4.10}$$

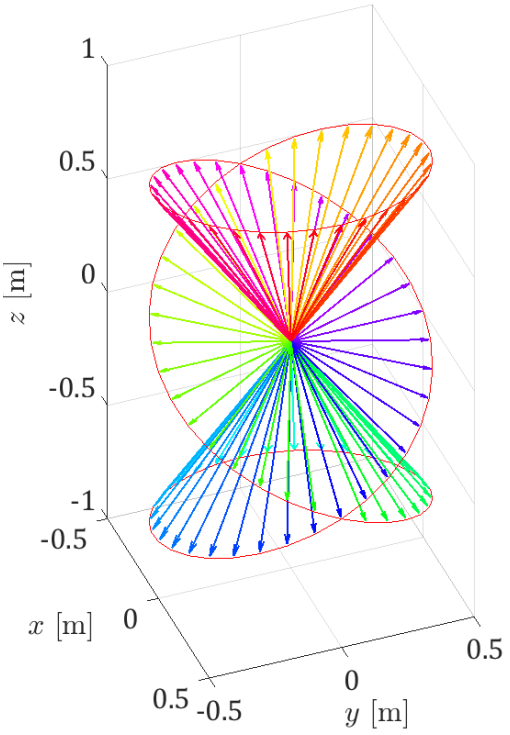

FIGURE 4.2: Visualization of $\{\sigma(k)\}_{k=0}^{N-1=95}$ in $\mathbb{R}^3$ with $r_1 = 1/2$, $r_2 = \sqrt{3}/2$. The tips of arrows are connected to aid in visualizing the transition.

where $\omega = 2\pi/N$ and N is an even integer. Based on this, we generate the signal $\sigma(k)$ by defining Σ as follows:

$$\Sigma(\rho) = \begin{cases} \rho, & m = 2; \\ [r_1\rho_1,\ r_1\rho_2,\ r_2(4\rho_1^3 - 3\rho_1)]', & m = 3, \end{cases} \tag{4.11}$$

where r_1 and r_2 are two positive constants satisfying $r_1^2 + r_2^2 = 1$. For $m = 2$, it can be easily seen that $\sigma(k)$ is a vector on the unit circle. For $m = 3$, Figure 4.2 provides a visualization of $\sigma(k)$ with $r_1 = 1/2$, $r_2 = \sqrt{3}/2$ and $N = 96$. Note that N is to be selected as in the following lemma:

Lemma 4.1. *The mappings Π, Σ defined by (4.10) and (4.11) satisfy Assumption 4.1 for all $\rho(0) \in \mathcal{S}$ if $N \geq 4$ for $m = 2$ and $N \geq 8$ for $m = 3$.*

Proof. Let $\rho(0) = [\cos\varphi \ \ \sin\varphi]' \in \mathcal{S}$ for some $\varphi \in [0, 2\pi]$. Direct computation shows that

$$\rho(k) = \Pi^k \rho(0) = \begin{bmatrix} \cos(k\omega + \varphi) \\ \sin(k\omega + \varphi) \end{bmatrix};\ \|\rho(k)\| \equiv 1,\ \forall k \in \mathbb{N}. \tag{4.12}$$

Therefore, the first condition in Assumption 4.1 is satisfied. Now we consider conditions ii. and iii. respectively for $m = 2$ and $m = 3$.

Case 1: $m = 2$.

In this case, we have $\sigma(k) = \rho(k)$ and it is clear that $\|\sigma(k)\| \equiv 1$ satisfies condition ii.. Moreover, if $N > 0$ is an even integer, then $\sigma(k + K) = -\sigma(k)$ with $K = N/2$, and we are left to show that $\operatorname{span}\{\sigma(k) : k = 0, 1, \ldots, K-1\} = \mathbb{R}^2$. Actually, it is easy to check that $\det S = [\sigma(0)\ \sigma(1)] = \begin{bmatrix} \cos\varphi & \sin(\omega+\varphi) \\ \sin\varphi & \cos(\omega+\varphi) \end{bmatrix}$ is non-singular with $\det S = \sin(2\pi/N) \neq 0$ ($N \geq 4$ is an even integer), which completes the proof for $m = 2$.

Case 2: $m = 3$. In this case, we have $\Sigma(\rho) = [r_1\rho_1,\ r_1\rho_2,\ r_2(4\rho_1^3 - 3\rho_1)]'$ by (4.11). Noticing that $\cos(3\theta) = 4\cos^3\theta - 3\cos\theta$, we have

$$\sigma(k) = \Sigma(\rho(k)) = \begin{bmatrix} r_1\cos(\omega k + \varphi) \\ r_1\sin(\omega k + \varphi) \\ r_2\cos(3\omega k + 3\varphi) \end{bmatrix}, \tag{4.13}$$

and it holds that $\|\sigma(k)\| \leq \sqrt{r_1^2 + r_2^2} = 1$, satisfying condition ii. of Assumption 4.1. Moreover, we can check that $\sigma(k + K) = -\sigma(k)$ with $K = N/2$ for an even integer N, and we are left to show that $\operatorname{span}\{\sigma(k) : k = 0, 1, \ldots, K-1\} = \mathbb{R}^3$.

To this end, we consider the matrix $S = \begin{bmatrix} \sigma(k) & \sigma(k+1) & \sigma_{k+2} \end{bmatrix}$ and find $\det S$ for $k = 0, 1, \ldots, K-1$. Direction computation by replacing $\theta = \omega k + \varphi$ shows that

$$\begin{aligned} \det S = {} & r_1^2 r_2 \cos(3\theta)\big[\cos(\theta+\omega)\sin(\theta+2\omega) \\ & \qquad - \sin(\theta+\omega)\cos(\theta+2\omega)\big] \\ & - r_1^2 r_2 \cos(3\theta+3\omega)\big[\cos\theta\sin(\theta+2\omega) \\ & \qquad - \sin\theta\cos(\theta+2\omega)\big] \\ & + r_1^2 r_2 \cos(3\theta+6\omega)\big[\cos\theta\sin(\theta+\omega) \\ & \qquad - \sin\theta\cos(\theta+\omega)\big] \\ = {} & r_1^2 r_2\big[\cos(3\theta)\sin(\omega) - \cos(3\theta+3\omega)\sin(2\omega) \\ & \qquad + \cos(3\theta+6\omega)\sin\omega\big], \end{aligned}$$

where we used $\sin(\alpha-\beta)=\sin\alpha\cos\beta-\cos\alpha\sin\beta$ for the last equality. Now by using the following identities

$$\cos(\alpha)\sin(\beta)=\frac{1}{2}\left(\sin(\alpha+\beta)-\sin(\alpha-\beta)\right),$$
$$\sin(\alpha)-\sin(\beta)=2\sin\left(\frac{\alpha-\beta}{2}\right)\cos\left(\frac{\alpha+\beta}{2}\right),$$

we can further manipulate $\det S$ as follows:

$$\begin{aligned}\det S &= \frac{r_1^2 r_2}{2}\big[\sin(3\theta+\omega)-\sin(3\theta-\omega)\\ &\qquad -\sin(3\theta+5\omega)+\sin(3\theta+\omega)\\ &\qquad +\sin(3\theta+7\omega)-\sin(3\theta+5\omega)\big]\\ &= \frac{r_1^2 r_2}{2}\big[\sin(3\theta+7\omega)-\sin(3\theta-\omega)\\ &\qquad +2\sin(3\theta+\omega)-2\sin(3\theta+5\omega)\big]\\ &= r_1^2 r_2\big(\sin(4\omega)-2\sin(2\omega)\big)\cos(3\theta+3\omega)\\ &= \mathcal{A}\cos(\mathcal{B}k+\mathcal{C}),\end{aligned}$$

where $\mathcal{A}\triangleq r_1^2 r_2\big[\sin(8\pi/N)-2\sin(4\pi/N)\big]$, $\mathcal{B}\triangleq 6\pi/N$, and $\mathcal{C}\triangleq 3\varphi+6\pi/N$.

Clearly, $\mathcal{A}=0$ iff $N=2,4$, and $\mathcal{A}\neq 0$ with $N\geq 8$. Moreover, note that $\cos(\mathcal{B}k+\mathcal{C})=0$ iff $6\pi(k+1)/N+3\varphi=2n\pi+\pi/2$ or $2n\pi+3\pi/2$ for some $n\in\mathbb{N}$. If $\cos(\mathcal{B}+\mathcal{C})\neq 0$ for $k=0$, then we conclude that $\text{span}\{\sigma(k)\colon k=0,1,2\}=\mathbb{R}^3$. Otherwise, assume that $6\pi/N+3\varphi=2n_0\pi+\pi/2$ for some $n_0\in\mathbb{N}$. Then it always holds that $6\pi/N<\pi$ with $N\geq 8$, namely that $\cos(2\mathcal{B}+\mathcal{C})\neq 0$, which implies $\text{span}\{\sigma(k)\colon k=1,2,3\}=\mathbb{R}^3$. A similar argument can be applied if $6\pi/N+3\varphi=2n_0\pi+3\pi/2$ for some $n_0\in\mathbb{N}$, and we conclude that $\text{span}\,\{\sigma(k)\colon k=0,1,\ldots,K-1\}=\mathbb{R}^m$. Now the proof is complete. ■

Remark 4.5. *Note that a function $f(d(k))$ satisfying $f(0)=0$, $0<f(d)\leq d$, $\forall d>0$ can be used in place of $d(k)$ in the control law (4.8) without affecting any result on stability and convergence. We have conducted simulations as well as experiments with $f(d(k))=10(1-e^{-10d(k)})$ and found that the convergence is slower than the case of $f(d(k))=d(k)$, hence the choice of $f(d)=d$ in the current control law.*

4.4 Convergence Analysis

In this section we will first establish the stability of the system, and then invoke LaSalle's invariance principle to establish the convergence of the docking objective (4.1).

4.4.1 Stability Analysis

Denote $\tilde{q}(k) = \hat{q}(k) - q(k)$ as the estimation error for relative localization, and note that $q(k) = p(k) - p^*$ is the position error for navigation. In this section, we shall show the boundedness of $\tilde{q}(k)$ and $q(k)$, respectively in Proposition 4.1 and Proposition 4.2 below. Specifically, we consider the following condition:

$$\gamma(TU)^2 < 2; \quad \alpha < \beta < 1/T, \tag{4.14}$$

where γ, β, α are constants. Note that for fixed γ and α, both of the above conditions can be met by a small sampling period T. On the other hand, for a fixed T, they can be satisfied by small γ and α. The following two propositions respectively establish the boundedness for the estimation error and the position error.

Proposition 4.1 (Boundedness of estimation error)**.** *Under the estimator* (4.7) *and the condition* $\gamma(TU)^2 < 2$*, it holds that* $\|\tilde{q}(k)\| \leq \|\tilde{q}(0)\|$ *and* $\epsilon(k) \in \ell_\infty \cap \ell_2$*.*

Proof. By defining $\bar{q}(k) \triangleq \hat{q}(k-1) + \phi(k-1) + \gamma\phi(k-1)\epsilon(k-1)$ and $g(k) \triangleq \pi_{d(k)}(\bar{q}(k)) - \bar{q}(k)$ we obtain the dynamics of $\tilde{q}(k)$ as follows:

$$\tilde{q}(k) = \bar{q}(k) + g(k) - q(k) = \big(I - \gamma\phi(k-1)\phi'(k-1)\big)\tilde{q}(k-1) + g(k). \tag{4.15}$$

From the error dynamics (4.15), we can define a Lyapunov-like function $V(k) \triangleq \gamma^{-1}\tilde{q}'(k)\tilde{q}(k)$ and examine its rate of change $\Delta V(k+1) = V(k+1) - V(k)$ using similar procedures that were used to prove Lemma 4.1.1 and Theorem 4.10.4 in [123]. From this examination and the assumption $\gamma(TU)^2 < 2$, we can see that $\forall k \geq 0$, $\Delta V(k+1) \leq -\epsilon^2(k)(2 - \gamma\phi'(k)\phi(k)) \leq 0$. Hence $\tilde{q}(k) \in \ell_\infty$ and $\epsilon(k) \in \ell_\infty \cap \ell_2$. ■

Proposition 4.2 (Ultimate boundedness of docking error)**.** *Under the estimator* (4.7) *and the bounded controller* (4.8)*, let condition* (4.14) *and Assumption 4.1*

hold. Given the initial relative estimation error $\tilde{q}(0)$ *and position error* $q(0)$*, there exists a constant* $M(\tilde{q}(0))$ *to satisfy the following statements:*

i. If $q(k_0) \in \mathcal{M} \triangleq \bar{\mathcal{B}}(0, M(\tilde{q}(0)))$ *for some* k_0*, then* $q(k) \in \mathcal{M}$ *for all* $k \geq k_0$*.*

ii. There exists a time step $k_0(q(0), M)$ *such that* $q(k_0) \in \mathcal{M}$*.*

As a consequence, $\limsup_{k\to\infty} \|q(k)\| \leq M(\tilde{q}(0))$ *for any* $q(0)$*.*

Proof. Define $D(k) = d^2(k)$ and $\Delta D(k) = D(k+1) - D(k)$. Recalling the definition of π_U in (4.3), we obtain by (4.5) that

$$\begin{aligned} \Delta D(k+1) &= (q(k) + T\bar{u}(k))'(q(k) + T\bar{u}(k)) - q'(k)q(k) \\ &= s(k)T(s(k)Tu'(k)u(k) + 2u'(k)q(k));\ s(k) \triangleq s_U(u(k)); \end{aligned} \tag{4.16}$$

which gives rise to $\Delta D(k+1)/(s(k)T) \leq Tu'(k)u(k) + 2u'(k)q(k) \triangleq \Delta\tilde{D}(k+1)$ as a result of $s(k) \in (0, 1]$. By substituting $u(k) = -\beta(q(k) + \tilde{q}(k)) + \alpha \|q(k)\| \sigma(k)$ into $\Delta\tilde{D}(k+1)$ as $\|q(k)\| = d(k)$, we get that (henceforth the time arguments (k), $(k+1)$ shall be omitted to keep the notation concise):

$$\begin{aligned} \Delta\tilde{D} &= T\beta^2(\|q\|^2 + \|\tilde{q}\|^2 + 2\tilde{q}'q) + T\alpha^2 \|q\|^2 \|\sigma\|^2 \\ &\quad - 2T\beta\alpha \|q\| \sigma'(q + \tilde{q}) - 2\beta(\|q\|^2 + \tilde{q}'q) + 2\alpha \|q\| \sigma'q \\ &= (T\beta^2 - 2\beta) \|q\|^2 + T\alpha^2 \|q\|^2 \|\sigma\|^2 + (2 - 2T\beta)\alpha \|q\| \sigma'q \\ &\quad + (2T\beta^2 - 2\beta)\tilde{q}'q - 2T\beta\alpha \|q\| \sigma'\tilde{q} + T\beta^2 \|\tilde{q}\|^2 \\ &\leq [T\beta^2 + T\alpha^2 - 2\beta + (2 - 2T\beta)\alpha] \|q\|^2 \\ &\quad + 2\beta[(1 - T\beta) + T\alpha] \|q\| \|\tilde{q}\| + T\beta^2 \|\tilde{q}\|^2, \end{aligned} \tag{4.17}$$

where to attain the last inequality we have used the condition $\|\sigma(k)\| \leq 1$ in Assumption 4.1, $1 - T\beta > 0$, as well as Cauchy-Schwartz inequality. Furthermore, by recalling (4.14), it is readily seen that the coefficient of $\|q(k)\|^2$ is given by

$$\begin{aligned} T\beta^2 + T\alpha^2 - 2\beta + (2 - 2T\beta)\alpha &= (\beta - \alpha)[T(\beta - \alpha) - 2] \\ &\leq -(\beta - \alpha)(T\alpha + 1) < 0. \end{aligned}$$

Thus, in combination with $\|\tilde{q}(k)\| \leq \tilde{Q} \triangleq \|\tilde{q}(0)\|$ in Proposition 4.1, we have

$$\Delta D(k) \leq s(k)T\big(-a \|q(k)\|^2 + b \|q(k)\| + c\big), \tag{4.18}$$

where $a = (\beta - \alpha)(T\alpha + 1)$, $b = 2\beta[(1 - T\beta) + T\alpha]\tilde{Q}$ and $c = T\beta^2\tilde{Q}^2$. Therefore, $\Delta D(k) < 0$ for $q(k) > \tilde{M}(\tilde{q}(0)) \triangleq (b + \sqrt{b^2 + 4ac})/(2a)$.

Consequently, if we take $M = \tilde{M}(\tilde{q}(0)) + TU$, then the statement i. can be achieved by the following induction: if $\|q(k_0)\| \leq \tilde{M}$, then $\|q(k_0 + 1)\| \leq M$ by noticing the bounded input (4.2); if $\tilde{M} < \|q(k_0)\| \leq M$, then $\|q(k_0 + 1)\| < \|q(k_0)\| \leq M$.

On the other hand, if $\|q(0)\| \leq M$ then the statement ii. follows. Otherwise we know that $\|q(k)\| \leq \|q(0)\|$ for all k, and $\|u(k)\| \leq \beta\tilde{Q} + \alpha\|q(0)\|$. Hence $s(k) = U/\max\{U, \|u(k)\|\} \geq U/\max\{U, \beta\tilde{Q} + \alpha\|q(0)\|\} > 0$. Moreover, it can be seen that $-a\|q(k)\|^2 + b\|q(k)\| + c \leq -aM^2 + bM + c < 0$ for $\|q(k)\| \geq M$; in this case, we can obtain from (4.18) that

$$\Delta D(k) \leq TU/\max\{U, \beta\tilde{Q} + \alpha\|q(0)\|\}\big(-aM^2 + bM + c\big), \tag{4.19}$$

implying that $\|q(k)\|$ will keep decreasing until $q(k_0) \in \mathcal{M}$ for some time step k_0, which is the statement ii. ■

4.4.2 Convergence

Let us recall the LaSalle's invariance principle for discrete-time autonomous systems as follows:

Lemma 4.2 (Discrete-time LaSalle's invariance principle [124]). *Consider a discrete-time autonomous system $x(k+1) = g(x(k)), k = 0, 1, 2, \ldots$, with $g\colon \mathcal{G} \to \mathcal{G}$ being a continuous map defined on a closed set $\mathcal{G} \subseteq \mathbb{R}^l$. Suppose there exists a scalar function $V\colon \mathbb{R}^l \to \mathbb{R}$ satisfying*

1. *$V(x)$ is continuous at any $x \in \mathcal{G}$;*
2. *$V(g(x)) - V(x) \leq 0$ for any $x \in \mathcal{G}$.*

For any $x(0) \in \mathcal{G}$, if $\mathcal{X} = \{x(k)\}_{k=0}^{\infty} \subseteq \mathcal{G}$ is bounded, then there exists $c \in \mathbb{R}$ such that the limit set of $\mathcal{X}$ is included in $\bar{\mathcal{I}} \cap V^{-1}(c)$, where $\bar{\mathcal{I}}$ is the maximum invariant set in $E \triangleq \{x \in \mathcal{G}\colon V(g(x)) - V(x) = 0\}$ and $V^{-1}(c) = \{x \in \mathbb{R}\colon V(x) = c\}$.

Now we are ready to assert the convergence of $q(k)$ to 0 in the theorem below:

Theorem 4.1. *Under Assumption 4.1, the distance-based docking problem (4.1) can be solved by combining the adaptive estimator (4.7) and the bounded controller (4.8), if we select proper gains to satisfy conditions (4.14).*

Proof. The overall system is given by combining the update protocol of $q(k), \tilde{q}(k), \rho(k)$ respectively in (4.5), (4.15) and (4.9) as follows:

$$\begin{cases} q(k+1) = q(k) + \phi(k), \\ \tilde{q}(k+1) = \pi_{d(k+1)}\left[q(k) + \phi(k) + (I - \gamma\phi(k)\phi'(k))\tilde{q}(k)\right] - (q(k) + \phi(k)), \\ \rho(k+1) = \Pi(\rho(k)), \ k = 0, 1, 2, \ldots, \end{cases} \tag{4.20}$$

where $\phi(k) = T\bar{u}(k) = Ts(k)u(k)$, $u(k) = -\beta(q(k) + \tilde{q}(k)) + \alpha \|q(k)\| \sigma(k)$, $\sigma(k) = \Sigma(\rho(k))$. Clearly, (4.20) defines a continuous map on $\mathbb{R}^m \times \mathbb{R}^m \times \mathcal{S}$, where $\mathcal{S}$ is defined in Assumption 4.1. Besides, by Propositions 4.1 and 4.2, for any given initial relative position error $q(0)$ and estimation error $\tilde{q}(0)$, there exists a time step k_0 such that $[q'(k), \tilde{q}'(k), \rho'(k)]' \in \mathcal{G} \triangleq \tilde{\mathcal{Q}} \times \mathcal{M} \times \mathcal{S}$ for $k \geq k_0$, where $\tilde{\mathcal{Q}} = \bar{\mathcal{B}}(0, \|\tilde{q}(0)\|)$ and $\mathcal{M}$ is defined in Proposition 4.2. Therefore, without loss of generality we only need to consider the trajectory starting within $\mathcal{G}$, and it can be concluded from Propositions 4.1, 4.2 and Assumption 4.1 that $\mathcal{G}$ is positively invariant under (4.20). Moreover, $\mathcal{G}$ is a compact set by recalling Propositions 4.1 and 4.2, as well as condition i. of Assumption 4.1, and hence LaSalle's invariance principle [124] can be applied.

By Lemma 4.2, all trajectories in $\mathcal{G}$ will converge to the maximum invariant set $\bar{\mathcal{I}} \subseteq \mathcal{G}$ satisfying $\Delta V(k) \equiv 0, \forall k \in \mathbb{N}^+$, where V is the Lyapunov function defined in the proof of Proposition 4.1. We shall show that for any trajectory $\{[q'(k), \tilde{q}'(k), \rho'(k)]'\}_{k=0}^{\infty} \in \bar{\mathcal{I}}$, it must hold that $q(k) \equiv 0$. Note that in the sequel we shall abuse the notation of $q(k), \tilde{q}(k), \rho(k)$ to denote the trajectory in $\bar{\mathcal{I}}$.

Actually, it is readily seen from the proof of Proposition 4.1 that $\Delta V(k) \equiv 0$ iff $\epsilon(k) = -\phi'(k-1)\tilde{q}(k-1) \equiv 0$, which due to (4.15) also implies that $\tilde{q}(k) \equiv \tilde{q}(0)$. Below we consider $\phi'(k)\tilde{q}(0) \equiv 0$ for 3 cases to establish that $\phi'(k)\tilde{q}(0) \equiv 0$ dictates either $\phi(k) \equiv 0$ or $\tilde{q}(0) = 0$.

Case 1: $\tilde{q}(0) \neq 0$ and $\phi(k) \not\equiv 0$. In this case, we have two deductions as follows:

First, since $0 \equiv \phi'(k)\tilde{q}(0) = (q(k+1) - q(k))'\tilde{q}(0) = (\hat{q}(k+1) - \hat{q}(k))'\tilde{q}(0)$, we get that $\hat{q}'(k)\tilde{q}(0) \equiv \hat{q}'(0)\tilde{q}(0)$.

Second, if $d(k) = 0$, then $u(k) = -\beta\tilde{q}(k) = -\beta\tilde{q}(0)$, and $\phi(k) = -T\beta s(k)\tilde{q}(0)$, which follows that $\phi'(k)\tilde{q}(0) = -\beta T s(k)\|\tilde{q}(0)\|^2 \neq 0$, a contradiction. Therefore, $d(k) > 0, \forall k \in \mathbb{N}$.

On the other hand, $0 \equiv \phi'(k)\tilde{q}(0)$ also implies that $0 \equiv u'(k)\tilde{q}(0) = [-\beta\hat{q}(k) + \alpha d(k)\sigma(k)]'\tilde{q}(0)$, or equivalently $\beta\hat{q}'(0)\tilde{q}(0) \equiv \beta\hat{q}'(k)\tilde{q}(0) = \alpha d(k)\sigma'(k)\tilde{q}(0)$. Specifically, we have $d(k)\sigma'(k)\tilde{q}(0) = d(k+K)\sigma'(k+K)\tilde{q}(0)$. Recall that $\sigma(k+K) = -\sigma(k)$ in Assumption 4.1, we can further obtain that

$$[d(k) + d(k+K)]\sigma'(k)\tilde{q}(0) \equiv 0, k = 0, 1, \ldots, K-1. \tag{4.21}$$

As a consequence of $d(k) > 0$ for any k, the above can be simplified as $\sigma'(k)\tilde{q}(0) \equiv 0$. In addition, noticing that $\text{span}\{\sigma(k) : k = 0, 1, \ldots, K-1\} = \mathbb{R}^m$ in Assumption 4.1, we can find a linear combination of $\tilde{q}(0)$ as $\tilde{q}(0) = \sum_{k=0}^{K-1} a(k)\sigma(k)$, which follows by (4.21) that $\|\tilde{q}(0)\|^2 = \tilde{q}(0)' \sum_{k=0}^{K-1} a(k)\sigma(k) = 0$, another contradiction.

In summary, $\phi'(k)\tilde{q}(0) \equiv 0$ dictates that $\phi(k) \equiv 0$ or $\tilde{q}(0) = 0$.

Case 2: $\phi(k) \equiv 0$. In this case, $u(k) \equiv 0$ and $q(k) \equiv q(0)$, which yields that $d(k) \equiv d(0)$ and $\hat{q}(k) \equiv \hat{q}(0)$. Since $u(k) = -\beta\hat{q}(k) + \alpha\|q(k)\|\sigma(k) \equiv 0$, we have $\alpha d(0)\sigma(k) \equiv \beta\hat{q}(0)$. By remembering that $\text{span}\{\sigma(k) : k = 0, 1, \ldots, K-1\} = \mathbb{R}^m$ in Assumption 4.1, the only possible case is that $d(0) = 0$, namely $q(k) \equiv 0$.

Case 3: $\tilde{q}(0) = 0$. In this case, the estimation error is always 0, and the relative position dynamics is simplified to

$$q(k+1) = q(k) + Ts(k)(-\beta q(k) + \alpha d(k)\sigma(k)), \tag{4.22}$$

where $s(k)$ was defined in (4.3). It is clear that $q^* = 0$ is a globally asymptotically stable equilibrium for (4.22) by noting from (4.17) that $\Delta\tilde{D}(k+1) \leq -(\beta-\alpha)(T\alpha+1)\|q(k)\|^2$ if $\tilde{q}(0) = 0$.

In summary, we have completed the proof. ■

4.5 Further Discussion

In this section we put forth some discussions regarding the stability of the system subject to noise as well as a wider application of the algorithm for *relative docking* operations.

4.5.1 Stability Under Distance Measurement Error

In this section we consider the stability in the presence of bounded distance measurement error. Denote $\hat{d}(k) = d(k) + e(k)$ as the distance measurement at time step k, where $e(k)$ denotes the measurement error and $\|e(k)\| \leq \bar{e}$.

Moreover, denote $\hat{\zeta}(k-1) = \frac{1}{2}\left[\hat{d}^2(k) - \hat{d}^2(k-1) - \|\phi(k-1)\|^2\right]$ and $\hat{\epsilon}(k-1) = \hat{\zeta}(k-1) - \phi'(k-1)\hat{q}(k-1)$. The corresponding relative position estimator is obtained by replacing $\zeta(k-1)$ with $\hat{\zeta}(k-1)$ in (4.7) as follows:

$$\hat{q}(k) = \begin{cases} \hat{q}(k-1) + \phi(k-1) + \gamma\phi(k-1)\hat{\epsilon}(k), & k \neq 2nK; \\ \pi_{\hat{d}(k)}\left(\hat{q}(k-1) + \phi(k-1) + \gamma\phi(k-1)\hat{\epsilon}(k)\right), & k = 2nK, \end{cases} \tag{4.23}$$

where $n \in \mathbb{N}$ and K is defined in Assumption 4.1. Note that the projection $\pi_{\hat{d}(k)}(\cdot)$ in (4.7) is to help increase the convergence speed of $\tilde{q}(k)$, and its use is optional (the results in all previous propositions and theorems will still hold without this operation). In this section, it is only performed every $2K$ steps by the rule (4.23) for the ease of analysis. Straightforwardly, because of noisy distance measurement, the bounded controller will become:

$$\bar{u}(k) = \pi_U(u(k)),\ u(k) = -\beta\hat{q}(k) + \alpha\hat{d}(k)\sigma(k). \tag{4.24}$$

We present the stability result in the following theorem:

Theorem 4.2. *Assume that $\mu \triangleq \alpha/\beta < 1$ and let $\beta = \nu\gamma$, $\alpha = \mu\nu\gamma$ with $\nu < c_0/(2T)$, where c_0 is a constant depending on T, U and $\{\sigma(k)\}_{k=0}^{K-1}$. Under the adaptive estimator (4.23) and the bounded controller (4.24), the relative position error $q(k)$ satisfies $\|q(k)\| \leq 4U/\alpha$ for all k, provided that γ is sufficiently small*

and the distance measurement error is bounded by

$$\bar{e} < \frac{\mu(1-\mu)\nu}{13(\mu+1)KU}. \tag{4.25}$$

Proof. To show the stability, below we will first obtain the error dynamics, and then show the excitation of displacement $\phi(k+j)$ over $[k,\ k+2K-1]$ for large $d(k)$, and finally show the boundedness by a proper Lyapunov function.

1) Error dynamics. Without loss of generality we assume $k = 2nK$, which means that the projection operation is activated at the time step k. Hence:

$$\|\tilde{q}(k)\| \le 2\left[d(k) + \bar{e}\right]. \tag{4.26}$$

Similar to the analysis in the error-free case, the estimation error of the relative position will evolve as follows:

$$\begin{aligned}\tilde{q}(k+j+1) = &\left[I - \gamma\phi(k+j)\phi(k+j)'\right]\tilde{q}(k+j)\\ &+ \gamma\phi(k+j)\tilde{\zeta}(k+j),\ 0 \le j < 2K-1;\end{aligned} \tag{4.27}$$

where

$$\begin{aligned}\tilde{\zeta}(k+j) = &\, d(k+j+1)e(k+j+1) - d(k+j)e(k+j)\\ &+ \frac{1}{2}\left[e(k+j+1)^2 - e(k+j)^2\right].\end{aligned}$$

Note that from the definition of $\tilde{\zeta}(k+j)$, we have:

$$\|\tilde{\zeta}(k+j)\| \le \bar{e}^2 + \bar{e}\left[d(k+j+1) + d(k+j)\right] \le 2\bar{e}d(k+j) + \bar{e}^2 + \bar{e}TU. \tag{4.28}$$

For $j = 2K-1$, at step $k+j+1$ the projection operation will be activated, and by noticing (4.15) we can show that

$$\|\tilde{q}(k+j+1)\| \le \left\|[I - \gamma\phi(k+j)\phi'(k+j)]\tilde{q}(k+j) + \gamma\phi(k+j)\tilde{\zeta}(k+j)\right\|. \tag{4.29}$$

On the other hand, the relative position error will evolve as

$$\begin{aligned}q(k+j+1) = &\left[1 - T\beta s(k+j)\right]q(k+j) - T\beta s(k+j)\tilde{q}(k+j)\\ &+ T\alpha s(k+j)\left[d(k+j) + e(k+j)\right]\sigma(k+j),\end{aligned} \tag{4.30}$$

where $s(\cdot)$ was introduced in (4.3).

2) We firstly show that when $d(k)$ is sufficiently large, then $\phi(k+j)$ is excited over $[k,\ k+2K-1]$, i.e. there exists $c_0>0$ such that $\sum_{j=0}^{2K-1}\phi(k+j)\phi'(k+j)\geq c_0 I$. Hence, let us revise the control law as:

$$\begin{aligned}\bar{u}(k+j)&=\pi_U(u(k+j))=T\beta\pi_{U/\beta}(\tilde{u}(k+j)),\\ \tilde{u}(k+j)&=-\hat{q}(k+j)+\mu\hat{d}(k+j)\sigma(k+j).\end{aligned}\tag{4.31}$$

Since $\phi(t)=T\pi_U(u(t))=T\beta\pi_{U/\beta}(\tilde{u}(t))$, in the following we will examine $\hat{q}(t)$ and $\hat{d}(t)$ for $t\in[k,k+2K-1]$. Intuitively, the excitation follows from the observation that the change of $\hat{d}(t)\sigma(t)$ would dominate that of $\hat{q}(t)$ for large $d(t)$.

Denote $\gamma_1=\gamma TU$, $\gamma_2=\gamma(TU)^2$, $\Phi(k)=I-\gamma\phi(k)\phi(k)'$ and $\Phi(k+j:k)=\Phi(k+j)\Phi(k+j-1)\cdots\Phi(k)$. Note that $\|\Phi(k)\|\leq 1$ and $\|\Phi(k+j:k)-I\|\leq(1+\gamma_2)^j-1$. To show the latter, notice that:

$$\begin{aligned}\Phi(k+j:k)-I=&-\gamma\sum_{t=k}^{k+j}\phi(t)\phi'(t)+\gamma^2\sum_{\substack{t_1,t_2\in\{k,\dots k+j\}\\ t_1\neq t_2}}\phi(t_1)\phi'(t_1)\phi(t_2)\phi'(t_2)\\ &-\gamma^3\sum_{\substack{t_1,t_2,t_3\in\{k,\dots k+j\}\\ t_1\neq t_2\neq t_3}}\phi(t_1)\phi'(t_1)\phi(t_2)\phi'(t_2)\phi(t_3)\phi'(t_3)+\dots\end{aligned}$$

Hence:

$$\|\Phi(k+j:k)-I\|\leq\sum_{t=1}^{j}\binom{j}{t}\gamma^t(TU)^{2t}=\sum_{t=1}^{j}\binom{j}{t}\left[\gamma(TU)^2\right]^t=(1+\gamma_2)^j-1.$$

Thus, for $j\in[0,2K]$, it can be inferred from (4.27), (4.28) and (4.29) that

$$\begin{aligned}\|\tilde{q}(k+j)-\tilde{q}(k)\|&\leq\left[(1+\gamma_2)^j-1\right]\|\tilde{q}(k)\|\\ &\quad+\sum_{i=0}^{j-1}\gamma_1\bar{e}(\bar{e}+2d(k)+2iTU+TU)\\ &=\left[(1+\gamma_2)^j-1\right]\|\tilde{q}(k)\|+2\gamma_1\bar{e}jd(k)+\gamma_1\bar{e}j(\bar{e}+jTU)\\ &\leq g_1 d(k)+2g_0\bar{e}+2K\gamma_1\bar{e}(\bar{e}+2KTU),\end{aligned}\tag{4.32}$$

where in the first line we invoked $d(k+i)\leq d(k)+iTU$, and in the third line we notice that $\|\tilde{q}(k)\|\leq 2(d(k)+\bar{e})$ and denote $g_1=2g_0+4K\gamma_1\bar{e}$ with $g_0=$

$(1+\gamma_2)^{2K}-1$. Together with $\|q(k+j)-q(k)\| \leq 2KTU$, we have

$$\begin{aligned}\|\hat{q}(k+j)-\hat{q}(k)\| &\leq \|\tilde{q}(k+j)-\tilde{q}(k)\| + \|q(k+j)-q(k)\| \\ &\leq g_1 d(k) + g_2 \triangleq r_1,\end{aligned} \tag{4.33}$$

where $g_2 = 2KTU[1+\gamma\bar{e}(\bar{e}+2KTU)] + 2g_0\bar{e}$. On the other hand, it is clear that

$$d(k) - 2KTU - \bar{e} \leq \hat{d}(k+j) \leq d(k) + 2KTU + \bar{e}. \tag{4.34}$$

Note that from (4.31), for all $-\hat{q}(k)$, there exist $j_1 \in [0, 2K-1]$ and $j_2 = j_1 + K/2$ such that for $j \in \{j_1, j_2\}$, $\angle(\sigma(j), -\hat{q}(k)) \in [0, \pi/2]$, which entails $\|-\hat{q}(k)+\mu\hat{d}(k+j)\sigma(j)\| \geq \max\{\|-\hat{q}(k)\|,\ \|\mu\hat{d}(k+j)\sigma(j)\|\} \geq \|\mu\hat{d}(k+j)\sigma(j)\|$, in this case it can be seen that:

$$\begin{aligned}\|\tilde{u}(k+j)\| &= \|-\hat{q}(k+j)+\mu\hat{d}(k+j)\sigma(j)\| \\ &= \|-[\hat{q}(k+j)-\hat{q}(k)]-\hat{q}(k)+\mu\hat{d}(k+j)\sigma(j)\| \\ &\geq \|-\hat{q}(k)+\mu\hat{d}(k+j)\sigma(j)\| - \|\,[\hat{q}(k+j)-\hat{q}(k)]\,\| \\ &\geq \|\mu\hat{d}(k+j)\| - \|\hat{q}(k+j)-\hat{q}(k)\|\,.\end{aligned} \tag{4.35}$$

Note that the equality occurs when $\|\hat{q}(k)\| = 0$.

Substituting (4.33) and (4.34) to (4.35), we have

$$\|\tilde{u}(k+j)\| \geq \mu(d(k) - 2KTU - \bar{e}) - r_1 \triangleq r_2,\ \ j \in \{j_1, j_2\}, \tag{4.36}$$

and we have $\|\phi(k+j_1)\| = \|\phi(k+j_2)\| = TU$ if $\{\tilde{u}(k+j_1)\} \geq U$ and $\{\tilde{u}(k+j_2)\} \geq U$, which can be achieved if the following is satisfied:

$$\|\tilde{u}(k+j)\| \geq r_2 > \frac{U}{\beta},\ \ j \in \{j_1, j_2\}. \tag{4.37}$$

Also for the angle spanned by $\phi(k+j_1)$ and $\phi(k+j_2)$ to lie inside $(\varepsilon^*, \pi-\varepsilon^*)$, with $\varepsilon^* > 0$, using elementary geometry, we can find that it can be achieved if the following is satisfied

$$r_2 > (\sqrt{2}-1)r_1 = (\sqrt{2}-1)g_1 d(k) + (\sqrt{2}-1)g_2. \tag{4.38}$$

Thus a sufficient condition for both (4.37) and (4.38) can be as follows

$$r_2 > \max\left\{U/\beta, (\sqrt{2}-1)g_2\right\} + (\sqrt{2}-1)g_1 d(k). \tag{4.39}$$

Combining with (4.36) and (4.39) leads to

$$d(k) > \frac{\max\{U/\beta,\ (\sqrt{2}-1)g_2\} + g_2 + \mu(2KTU+\bar{e})}{\mu - \sqrt{2}g_1} \triangleq \bar{d}, \tag{4.40}$$

which means that if $d(t)$ is sufficiently large $\phi(t)$ is p.e. over $[k, k+2K-1]$.

3) Stability analysis. Denote $\Phi(t) = I - \gamma\phi(t)\phi(t)'$ and $\Phi(t_2 : t_1) = \Phi(t_2)\Phi(t_2 - 1)\cdots\Phi(t_1)$. It can be seen that $\|\Phi_{k+2K-1:k}\| \leq (1-\gamma c_0/2)$ for sufficiently small γ, and that $\|\Phi(t_2 : t_1)\| \leq 1$. Then by (4.27) and (4.29) it can be found that

$$\begin{aligned} \|\tilde{q}_{k+2K}\| &\leq \|\Phi_{k+2K-1:k}\|\,\|\tilde{q}(k)\| + 4K\gamma_1\bar{e}d(k) + g_3 \\ &\leq (1-\gamma c_0/2)\,\|\tilde{q}(k)\| + 4KTU\gamma\bar{e}d(k) + g_3, \end{aligned} \tag{4.41}$$

where $g_3 = 2KTU\gamma\bar{e}(\bar{e}+2KTU)$, and the second inequality follows from the excitation of $\phi(t)$ and sufficiently small γ. Furthermore, it follows from (4.30) that

$$d(k+2K) \leq [(1 - T(\beta-\alpha)s(k)) + 4KT^2U\beta\gamma\bar{e}]d(k) + T\beta 2K\,\|\tilde{q}(k)\| + g_4, \tag{4.42}$$

where $s(k) \geq U/[(\beta+\alpha)(d(k)+\bar{e})]$ and $g_4 = T^2U\beta\gamma\bar{e}(\bar{e}+2KTU) + 2KT\alpha\bar{e}$. If γ, β and $\bar{e}$ are sufficiently small, then $\eta = \min\{\gamma c_0/2 - T\beta 2K, T(\beta-\alpha)s(k) - 4KTU\gamma\bar{e}(1+T\beta)\} > 0$. If we denote $V(k) = \|\tilde{q}(k)\| + d(k)$, then it yields from (4.41) and (4.42) that

$$V_{k+2K} \leq (1-\eta)V(k) + g_3 + g_4. \tag{4.43}$$

Therefore, we know that $d(k)$ will be ultimately bounded, and hence there exists $s^* > 0$ such that $s(k) \geq s^*$ for all k.

4) Ultimate bound. Recall that $\beta = \nu\gamma$ and $\alpha = \mu\nu\gamma$. We can find small γ so that $d(0) \leq \bar{d} < (1+\varepsilon)U/\alpha$ with ε being a small number. Moreover, we have $V(k+2K) < V(k)$ in (4.43) if $V(k) > (g_3+g_4)/\eta = V^*$. Given $\nu < c_0/(2T)$ and small $\bar{e}$, we can see that $g_3 + g_4 = O(\gamma)$ and $\eta = O(\gamma)$, and hence V^* is smaller than a constant independent of γ. Hence we can choose sufficiently small

γ such that $\alpha = \mu\nu\gamma$ is sufficiently small to ensure $(1+\varepsilon)U/\alpha \geq V^*$. Therefore, if $\bar{d} < d(k_0) \leq (1+\varepsilon)U/\alpha$ with $k_0 = 2n_0K$, then $V(k_0+2K) < V(k_0) \leq 3d(k_0) + 2\bar{e}$, and we conclude that $d(k) \leq 3(1+\varepsilon)U/\alpha + 2\bar{e} \leq 4U/\alpha$ for small γ, $\bar{e}$ and $k \geq k_0$. Consequently, we find that $s(k) \geq \mu U/[3(1+\varepsilon)(1+\mu)U + \alpha(\mu+1)\bar{e}]$, and $T(\beta-\alpha)s(k) > 4KTU\gamma\bar{e}(1+T\beta)$ follows from (4.25) and small γ. ■

Remark 4.6. *The above result implies that the system stability can be retained if the distance measurement error is small. Note that the choice of γ may be dependent on the initial position error, and the upper bound $4U/\alpha$ is conservative. More investigation is needed in the future to improve the result.*

4.5.2 Relative Docking

As introduced earlier, in most real-world applications such as autonomous landing, search and rescue, it is sufficient to control the MAV to reach a proximity and then rely on visual tracking method to directly estimate the relative position. Hence, the docking objective can be revised to reaching a neighbourhood around a location that does not necessarily coincide with the landmark's position; or in other words: given a landmark arbitrarily deployed at an unknown position p^* and a desired location q^* relative to this landmark, design a control law to achieve:

$$\limsup_{k\to\infty} \|p(k) - p^* - q^*\| \leq \bar{\alpha}, \tag{4.44}$$

where $\bar{\alpha} > 0$ is a user defined constant.

To solve the above problem, we will use the same estimator (4.7), and modify the controller (4.8) as follows:

$$\bar{u}(k) = \pi_U(u(k)),\ u(k) = -\beta\left[\hat{q}(k) - q^*\right] + \alpha\sigma(k),\ \beta > 0,\ \alpha > 0. \tag{4.45}$$

Due to the similarity in (4.8) and (4.45), one would expect that similar results on stability and convergence can be obtained. Indeed if we define a new relative position state $\bar{q}(k) \triangleq p(k) - p^* - q^* = q(k) - q^*$, we can immediately proceed with the following results on stability and convergence of the system:

Proposition 4.3. *Under the estimator* (4.7) *and the bounded controller* (4.45)*, let conditions* (4.14) *and Assumption 4.1 hold. Given the initial values* $\tilde{q}(0)$*,* $\bar{q}(0)$*, there exists a constant* $\bar{M}(\tilde{q}(0))$ *satisfying the following statements:*

i. If $\bar{q}_{k(0)} \in \bar{\mathcal{M}} \triangleq \bar{\mathcal{B}}(0, \bar{M}(\tilde{q}(0)))$ *for some* k_0*, then* $\bar{q}(k) \in \bar{\mathcal{M}}$ *for* $k \geq k_0$*.*

ii. There exists a time step $k_0(\bar{q}(0), \bar{\mathcal{M}})$ *such that* $q(k_0) \in \bar{\mathcal{M}}$*.*

As a consequence, $\limsup_{k\to\infty} \|\bar{q}(k)\| \leq \bar{M}(\tilde{q}(0))$ *for any* $\bar{q}(0)$*.*

Proof. Similar to the proof of Proposition 4.2, we define $\bar{D}(k) = \|\bar{q}\|^2$ and $\Delta\bar{D}(k+1) = \bar{D}(k+1) - \bar{D}(k)$ and obtain

$$\Delta\bar{D}(k+1)/(sT) \leq -\beta(2-T\beta)\|\bar{q}\|^2 + 2(1-T\beta)(\alpha+\beta\|\tilde{q}\|)\|\bar{q}\| + 2\alpha T\beta\|\tilde{q}\| + T\beta^2\|\tilde{q}\|^2 + T\alpha^2. \tag{4.46}$$

Note that the leading coefficient of the quadratic function in (4.46) is negative due to the assumption $T\beta < 1$, hence the boundedness of $\|\bar{q}(k)\|$ can be established using the same argument in the proof of Proposition (4.2). ■

Theorem 4.3. *Under Assumption 4.1, the relative docking problem* (4.44) *can be solved by combining the adaptive estimator* (4.7) *and the bounded controller* (4.45)*, if we select proper gains to satisfy conditions* (4.14)*. Moreover the ultimate bound* $\bar{\alpha}$ *satisfies* $\bar{\alpha} \leq \alpha/\beta$*.*

Proof. Based on Proposition 4.3, we can proceed similarly as in the proof of Theorem 4.1 to invoke LaSalle's invariance principle and examine the trajectories of $\tilde{q}(k)$, $\bar{q}(k)$ in the invariant set defined by $\Delta V(k) \equiv 0$. Along the same line as in the proof of Theorem 4.1, we find that $\tilde{q}(k) \equiv 0$. Thus, the dynamics of $\bar{q}(k)$ can be simplified as $\bar{q}(k+1) = \bar{q}(k) + T\pi_U[-\beta\bar{q}(k) + \alpha\sigma(k)]$. By examining $L(k) = \|\bar{q}(k)\|^2$ and $\Delta L(k+1) = L(k+1) - L(k)$, we find that $\Delta L(k+1) < 0$ for $\|\bar{q}(k)\| > \alpha/\beta$. On the other hand, if $\|\bar{q}(k)\| \leq \alpha/\beta$, we have $\|\bar{q}(k+1)\| = \|(1-T\beta s(k))\bar{q}(k) + Ts(k)\alpha\sigma(k)\| \leq (1-T\beta s(k))\|\bar{q}(k)\| + Ts(k)\alpha \leq \alpha/\beta$. Therefore, the limit set of those trajectories starting from the invariant set is included in $\bar{\mathcal{B}}(0, \alpha/\beta)$. ■

Remark 4.7. *In practice, it can be seen that under the control law (4.45) a small ultimate bound $\bar{\alpha}$ can always be satisfied by selecting sufficiently small $\alpha > 0$ such that $\bar{\alpha} < \alpha/\beta$. Note that the condition $\alpha < \beta$ in (4.14) does not have to be enforced for the relative docking objective to be achieved.*

4.6 Simulation

In this section, we will first verify the integrated localization-navigation scheme proposed in Sections 4.3 by numerical simulation for an ideal case to verify the theoretical findings. After that, we present another simulation with corrupted measurements and target drift. Finally, another simulation on relative docking will also be presented to verify the results in Theorem 4.3.

To be consistent with the experiment setup, we choose $T = 0.1\ s$ and $U = 0.75\ m/s$ throughout our simulations. The signal $\sigma(k)$ is generated by (4.10) and (4.11) with $\rho(0) = [1,\ 0]'$, $r_1 = 1/2$, $r_2 = \sqrt{3}/2$ and $N = 96$. For each simulation we always fix the initial estimate of the relative position as $\hat{q}(0) = [0,\ 0,\ 0]'$, and the initial position of the MAV as $p(0) = [-30,\ -30,\ 1]'$.

4.6.1 Error-Free Case

In this case we are concerned with a static landmark at $p^* = [-5,\ 2,\ 10]'$, which yields an initial relative position of $q(0) = [-25,\ 32,\ -9]'$. Under the above settings, we select different set of positive constants $\gamma,\ \beta,\ \alpha$ that satisfy condition (4.14). The results are shown in Figure 4.3.

Clearly, the docking problem is solved in all 8 cases as condition (4.14) is satisfied. Comparing Figure 4.3a and Figure 4.3b, we can see that a larger estimator gain γ leads to a faster localization convergence. If we further increase the controller gain β to 5, then we observe a slower estimator convergence and a more oscillating trajectory, as shown in Figure 4.3c. This can be explained as the proportional term becomes too dominant before the relative position estimate has sufficiently converged to the true value, thus causing the trajectory to have a large detour. Finally, we increase the excitation magnitude α from 1 to 4, then we can observe that not only the fast localization can be recovered, but the docking problem can

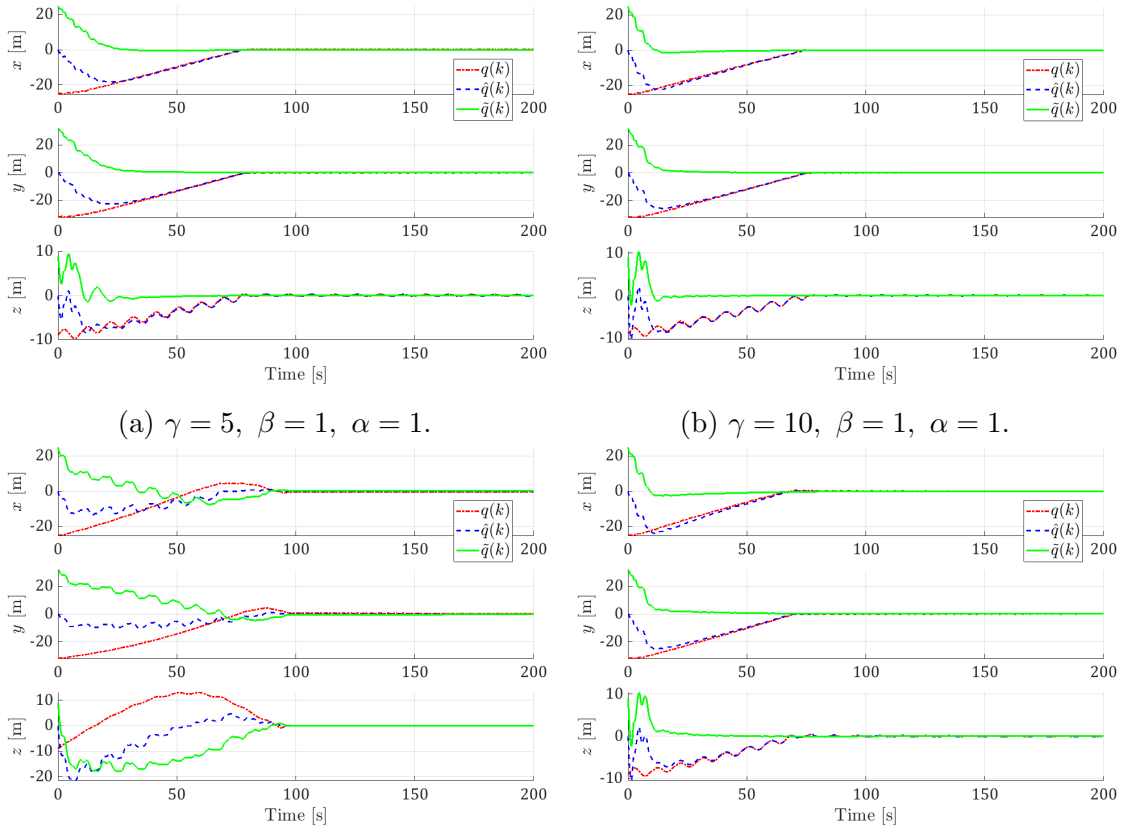

(a) $\gamma = 5,\ \beta = 1,\ \alpha = 1.$ (b) $\gamma = 10,\ \beta = 1,\ \alpha = 1.$

(c) $\gamma = 10,\ \beta = 5,\ \alpha = 1.$ (d) $\gamma = 10,\ \beta = 5,\ \alpha = 4.$

FIGURE 4.3: Performance comparison under different gains.

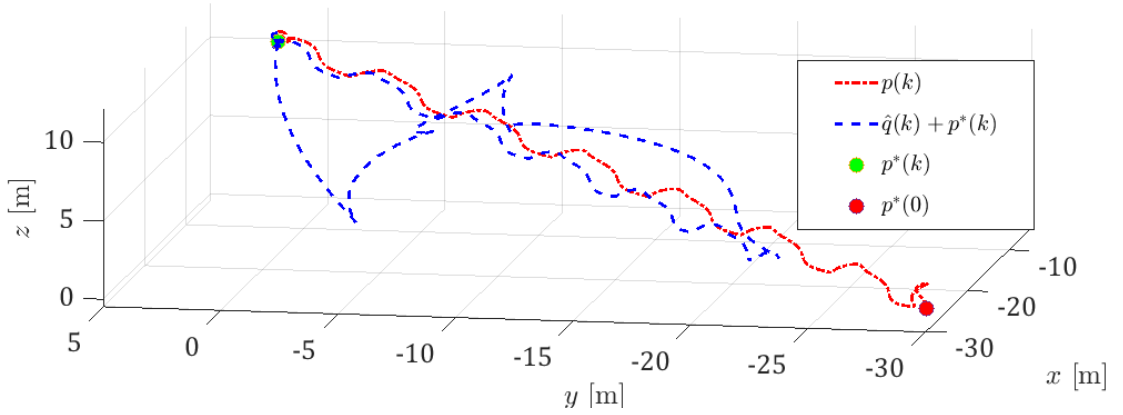

FIGURE 4.4: Trajectories of the MAV and the relative position estimates from the simulation with the gains $\gamma = 10,\ \beta = 5,\ \alpha = 4.$

also be solved fastly with a smooth trajectory, as shown in Figure 4.3d which achieves the best performance among the four cases in terms of fast localization and navigation. The 3D trajectory of the MAV in this simulation is illustrated in Figure 4.4. Note that the above process also shed some light on a proper gain tuning for better performance of the integrated scheme.

4.6.2 Corrupted Measurements and Target Drift

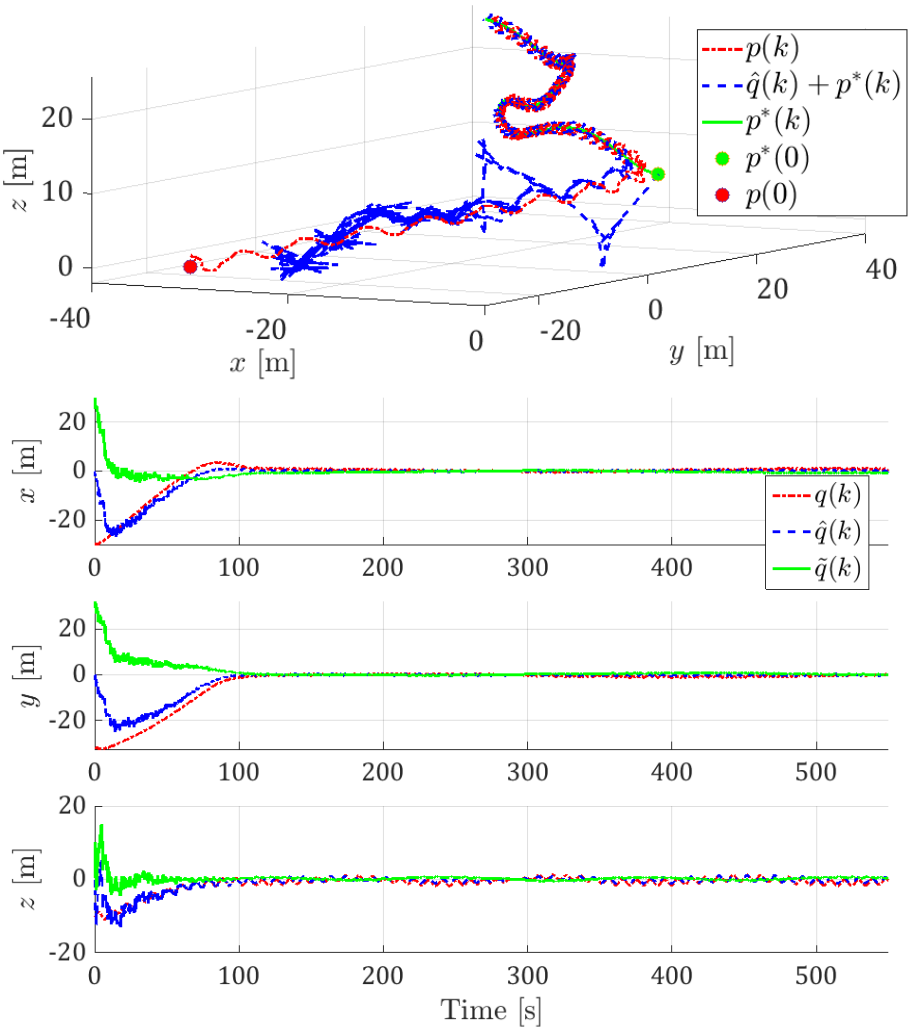

FIGURE 4.5: 3D visualization of the docking task with all possible corruptions against the ideal scenario. The initial position of the target is marked by the green circle and the MAV's initial position is marked by the red circle. The system state is shown below.

In practice certainly we cannot avoid measurement error. To investigate the robustness of the algorithm against measurement errors, we rerun the previous simulation ($\gamma = 10, \beta = 5, \alpha = 4$) with the presence of all possible errors. First, we add a zero-mean random noise with uniform distribution on the interval $[-0.1, 0.1]$ to the distance measurement. Second, we also add zero-mean noise with uniform distribution on the interval $[-0.01, 0.01]$ to each of the dimensions of displacement

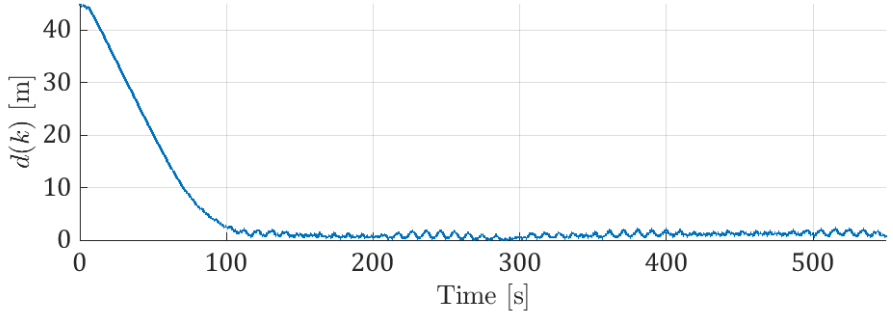

FIGURE 4.6: Distance to the drifting target with all possible measurements errors remains bounded.

measurement. Finally, the landmark is made to drift with its trajectory given as

$$p^*(k) = p^*(0) + \begin{bmatrix} 5\cos(kw) \\ 5\sin(kw) \\ \frac{5}{4}\cos(3kw) \end{bmatrix} + kT \begin{bmatrix} -0.05 \\ 0.05 \\ 0.025 \end{bmatrix}, \tag{4.47}$$

where $w = \pi/2048$ and $p^*(0) = [-5,\ 2,\ 10]'$.

It can be seen from Figure 4.5, and Figure 4.6 that the system is still stable and the MAV can still track the target similar to the ideal case, which demonstrates the robustness of the algorithm in the presence of noise and uncertainty (a drifting landmark).

4.6.3 Relative Docking

Different from the docking scenario, in relative docking scenario, α can be chosen arbitrarily according to the desired bound for the docking error $\bar{\alpha}$. Thus in this case we set $\alpha = 10$ and the maximum relative docking error $\bar{\alpha}$ can be calculated as $2m$, the relative docking position q^* is chosen as $q^* = [-20, 5, 2]'$. All other parameters are the same with the docking case.

It can be seen clearly in Figure 4.7 and Figure 4.8 that the docking error reduces to below the threshold $\bar{\alpha}$ given by Theorem 4.3.

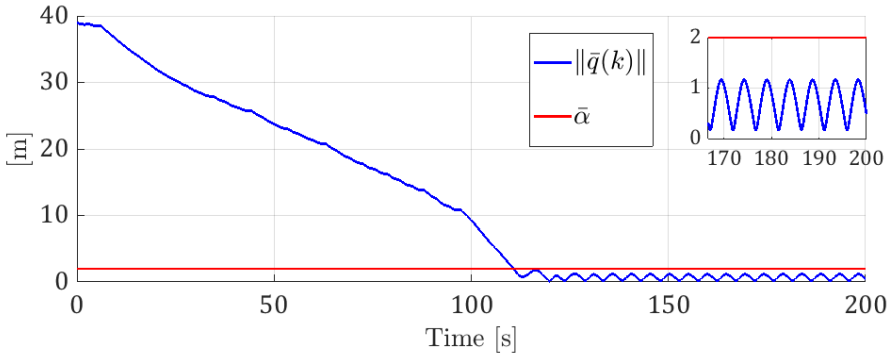

FIGURE 4.7: Relative docking error reduces to below $\bar{\alpha}^* = 2m$.

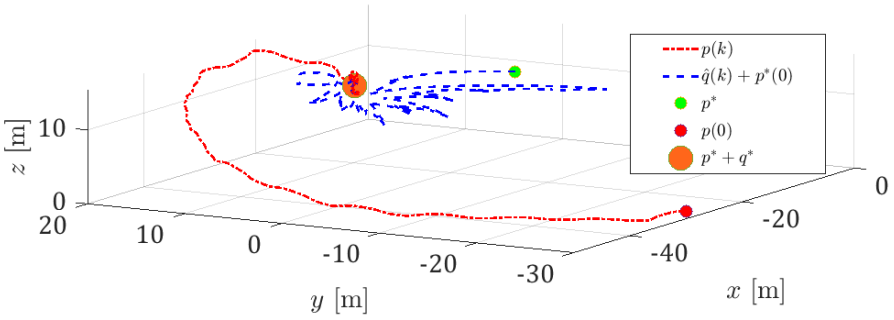

FIGURE 4.8: The MAV converge to within a proximity of $\bar{\alpha} = 2m$ around the relative docking destination $p^* + q^*$.

4.7 Experiments on Quadcopters

To further validate our theoretical findings in previous sections, in this section we implement the integrated localization-navigation scheme on quadcopters and conduct multiple tests in a GPS-less environment with the docking control law. Video recording of the experiment can be viewed at https://youtu.be/LJ8mtFIkliY.

For practical purpose, we introduce an additional parameter *terminal distance* d_ϵ, which is to prevent MAV from colliding with the landmark after successfully entering a predefined proximity around the target. In the experiment we take the terminal distance as 2 m, i.e. $d_\epsilon = 2$. The other parameters are the same as the ones used in the first simulation.

4.7.1 Experiment Setup

The algorithm is implemented in real-time on an onboard computer running Ubuntu and Robot Operating System (ROS). In our experiments, distance measurements $d(k)$ are obtained by using two UWB nodes, considering that UWB is robust to multipath and non-line-of-sight effects, and can provide a reliable long distance ranging over 100 m with an accuracy within 10 cm (as reported by the sensor's manufacturer[1]). On the other hand, odometry measurements $\phi(k)$ are obtained by fusing the output from *px4flow* optical flow sensor [2] with the measurements from an onboard altimeter and IMU using the EKF developed in Chapter 3.

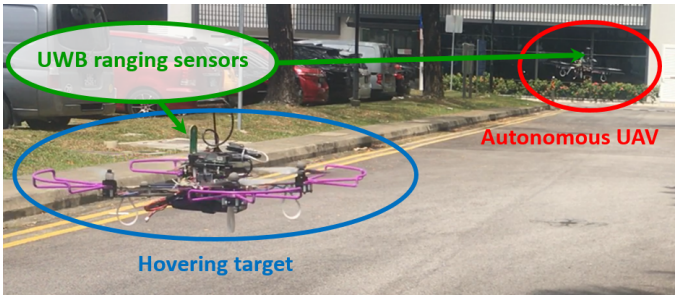

FIGURE 4.9: Experiment setup.

The flight tests were conducted in a $10m \times 50m$ runway surrounded by building blocks. As shown in Figure 4.9, one UWB node is mounted on a *target MAV (TMAV)* stably hovering at some unknown position, and the other one installed on an *autonomous MAV (AMAV)*. The AMAV is required to approach the TMAV from a distant starting point by only using distance measurements and odometry measurements. To provide ground truth for the experiment in absence of GPS, we employ the anchor-based localization system developed in our previous works [13], which is able to produce 10 cm localization accuracy. It should be emphasized that this localization information is only used as ground truth reference.

4.7.2 Experiment Results and Evaluation

A total of five tests with different starting points have been conducted to demonstrate the capability of the integrated localization-navigation scheme. As shown

[1] https://timedomain.com/products/pulson-440/
[2] https://docs.px4.io/en/sensor/px4flow.html

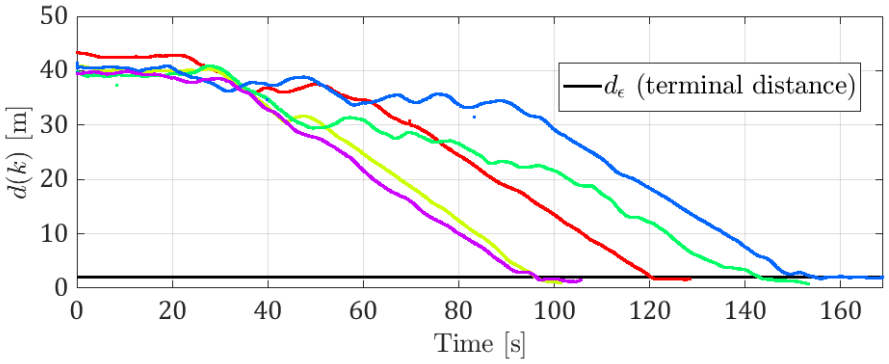

FIGURE 4.10: In all tests, the distance to TMAV is reduced to the terminal value.

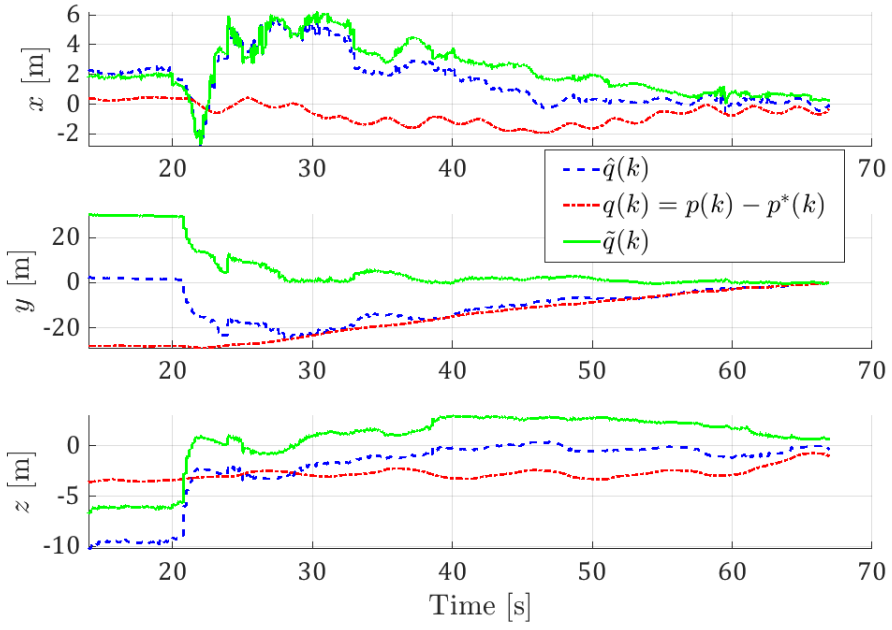

FIGURE 4.11: Relative position estimate and the *ground truth* from the anchor-based localization system.

in Figure 4.10, in all cases the distance between the MAVs decreases steadily and quickly until reaching the terminal distance.

To further examine the performance of the estimator and the controller, we select one of the flights, and plot its spatial trajectory and time evolution of the system states respectively in Figure 4.12. and Figure 4.11. As can be seen from Figure 4.12, AMAV is able to approach TMAV without much oscillation. We note that AMAV only moves within $[5, 10]$ on the x-axis during the whole journey, although starting at around 40 m away from TMAV. On the other hand, as illustrated in Figure 4.11, the relative position estimate, the error and the ground truth all converge to zero

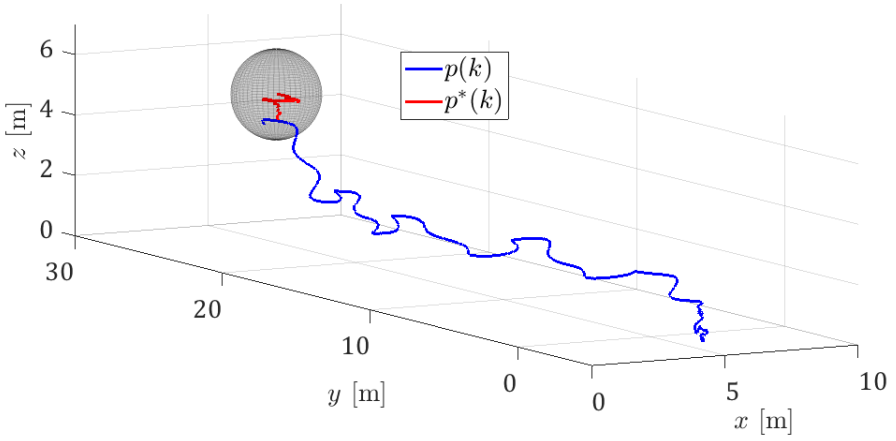

FIGURE 4.12: Spatial trajectory of AMAV as measured by the anchor-based localization system. A ball of radius 2 m is cast around the last recorded position of TMAV to indicate when the AMAV reaches the target. Video recording of this flight test can be viewed at https://youtu.be/LJ8mtFIkliY.

as AMAV approaches TMAV, which resembles the behaviour in the simulation of Figure 4.12.

In conclusion, the experiment results have shown a good and consistent performance of the proposed integrated localization-navigation scheme, and it is promising to further apply a similar integration idea to more practical scenarios.

4.8 Conclusion

In this chapter we have studied the distance-based docking problem of MAVs by using a single landmark placed at an arbitrary unknown position. An integrated estimation-control scheme that only requires distance and odometry measurements was proposed and proved to simultaneously accomplish the relative localization and navigation tasks for discrete-time integrators under bounded velocity. Simulations under different settings were conducted to show the performance and robustness of the algorithm, and the theoretical findings were also validated in a GPS-less environment by implementing the integrated scheme on quadcopters equipped with UWB and optical flow sensors.

Chapter 5

Ranging-Based Autonomous Docking of MAVs

5.1 Introduction

As having been introduced earlier, a complete *autonomous docking* process by MAV comprises of two phases: an approaching phase and a landing phase. While the landing problem can be considered mature by the use of vision, the approaching problem in GPS-denied environment still lacks a satisfactory solution. In this chapter, we will focus on resolving this issue with the insights from the previous chapters.

In Chapter 4, we have developed an adaptive estimator for the relative localization task. Notably, while it is commonly known that the estimation error under the adaptive estimator (4.7) would converge to zero exponentially fast when the observation $\phi(k)$ is designed to be p.e. (see (2.5)), no such assumption on $\phi(k)$ was made in Chapter 4, and the convergence of the estimation error was established by examining the trajectories in the invariant set defined by $V(k) \equiv 0$. However, it should be noted that the convergence was only confirmed to be asymptotic rather than exponential in the previous chapter, thus the estimation error appeared to decrease quite slowly as observed in the simulations and experiments. Indeed, it would be more desirable if the PE condition can be satisfied for a faster convergence rate of the relative localization estimate.

Following this direction, different from previous chapter where the MAV only ranges to a single landmark, in this chapter, we will assume that a set of UWB nodes can be installed on an adequately sized landing platform, and show that the PE feature can be achieved when the configuration of the anchors and the system parameters satisfy some mild conditions. Moreover, both vehicles are equipped with high-accuracy visual odometry systems [31, 63] to collect displacement measurements, which are transmitted through UWB message similar to Chapter 3. By combining the distance and displacement measurements in a similar manner as in Chapter 4, we propose a relative localization scheme based on recursive least-squares optimization, and rigorously prove the EC to the true relative position. Based on this relative position estimate, the MAV is able to efficiently fulfill the approaching and landing tasks from an initial large distance relative to the target. Extensive outdoor flight tests have been conducted to demonstrate that the MAV can approach the moving UGV from 50m away and then accurately land on a 1.5m×2m large platform.

In summary, the achievements of this chapter in comparison with previous ones can be listed as follows:

- We design a relative localization scheme by using distance measurements from sequential ranging to UWB anchors and relative displacement measurements from visual odometers. We then propose a recursive least-squares algorithm to estimate the relative position to the moving target, and show that the estimation error converges to zero exponentially fast.
- Compared with the work on Chapter 4 with long range navigation towards a static landmark, this work focuses on the cooperative docking of an MAV on a moving target, which achieves much higher flexibility for the docking task.
- In the landing phase, we fuse both visual-tracking-based relative position and range measurement using the sensor fusion technique in Chapter 3 to ensure an accurate landing maneuver on a small moving platform. We have conducted extensive indoor and outdoor experiments to show the efficacy and efficiency of the integrated UWB-vision approach from a distance up to 50m.

This chapter is organized as follows: In Section 5.2, we describe the key definitions and an overview of the integrated UWB-vision approach to solve the autonomous

docking problem with two specialized estimation-control schemes for approaching and landing tasks. In Section 5.3, we present the relative localization scheme in details along with a proof on its EC. Section 5.4 presents the results of our real flight experiments with the algorithm implemented in an autonomous docking scenario. Finally, Section 5.5 concludes the chapter.

5.2 Overview

5.2.1 Basic Definitions

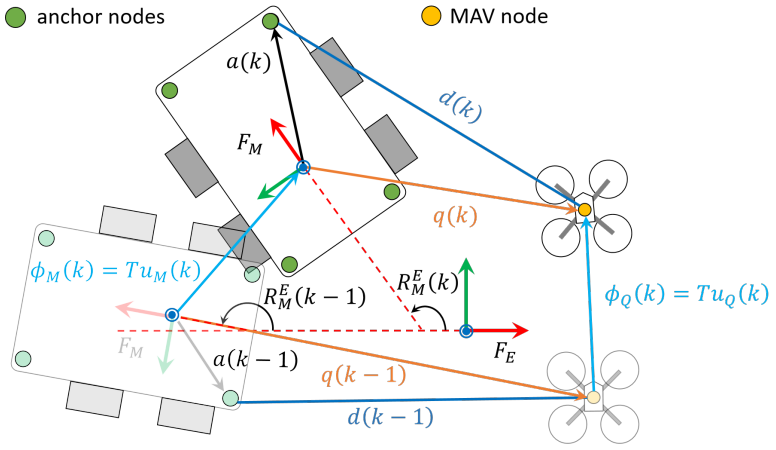

FIGURE 5.1: Visualization of the main concepts defined in Section 5.2.1.

In this section we will define some basic concepts needed for later parts in direct reference to Figure 5.1. First, we define $q(k)$ as the MAV position relative to the target with respect to an inertial frame of reference F_E (following the same convention in chapter 3, $q_{QM}^E(k)$ would be a more expressive notation, however in this chapter we would use $q(k)$ to keep the notation concise). In this work we assume that F_E is aligned with the earth's magnetic field.

In our setup, N UWB nodes a_0, a_1, ..., a_{N-1} (which also denote their coordinates in the mobile frame F_M fixed on the UGV) are installed on the UGV and another UWB node is also installed on the MAV. Henceforth, we refer to the UWB nodes on the UGV as the anchors. Note that the MAV node can only range to one anchor at a time and the ranging scheme is executed in a periodic manner as 0, 1, ..., $N-1$, 0, 1... Henceforth, we will also use $a(k)$ to denote the coordinates of the anchor a_i that is ranged to at the time step k, where explicit specification of index

i is glossed over to keep the notation simple (this detail is not used in subsequent analysis). However, when needed, it can be retrieved by the modulo operation $i = \mathrm{mod}(k, N)$.

As illustrated in Figure 5.1, at time kT with T being the sampling period, the following measurements can be obtained: for the MAV, it can measure the distance $d(k)$ to only one of the UWB nodes on the UGV, and its own displacement vector $\phi_Q(k)$ since the last time step $k-1$ from a visual odometer; for the UGV, it can measure its displacement vector $\phi_M(k)$ and the orientation $R_M^E(k)$ with respect to F_E using its own visual inertial odometry system, and send them to the MAV.

In reference to Figure 5.1, we also define $u_Q(k) = \frac{1}{T}\phi_M(k)$, $u_M(k) = \frac{1}{T}\phi_M(k)$ as the average velocity of the MAV and the UGV respectively from time step $k-1$ to k. Similarly, we treat the change from $R_M^E(k-1)$ to $R_M^E(k)$ as a rotation around an axis $l(k)$ from time step $k-1$ to k with an average angular rate $\omega(k)$, as illustrated in Figure 5.2.

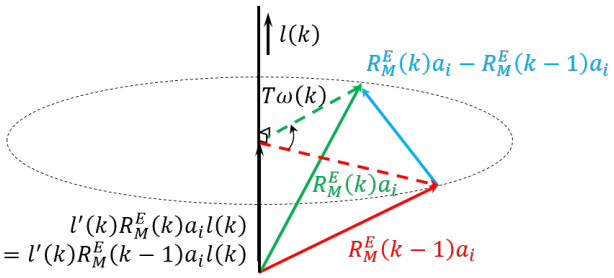

FIGURE 5.2: Characterization of the rotation rate: between two time steps, the frame F_M rotates by an angle $T\omega(k)$ around the axis $l(k)$. For a vector a_i that is fixed in F_M, its coordinates in the inertial frame F_E at time steps $k-1$ and k will be $R_M^E(k-1)a_i$ and $R_M^E(k)a_i$, respectively. It can be seen that $\left\|R_M^E(k)a_i - R_M^E(k-1)a_i\right\| \leq 2\left\|a_i\right\| \left|\sin(T\omega(k)/2)\right| \leq T\left\|a_i\right\| \left|\omega(k)\right|$. The equality occurs when a_i is orthogonal to $l(k)$.

5.2.2 Estimation-Control Schemes

5.2.2.1 Approaching

In this section we will describe the main ideas for accomplishing the approaching task in direct reference to Figure 5.3.

Firstly, the MAV will rely on an optical flow as the main feedback for stable flight control. Note that this optical flow measurement is fused with IMU and

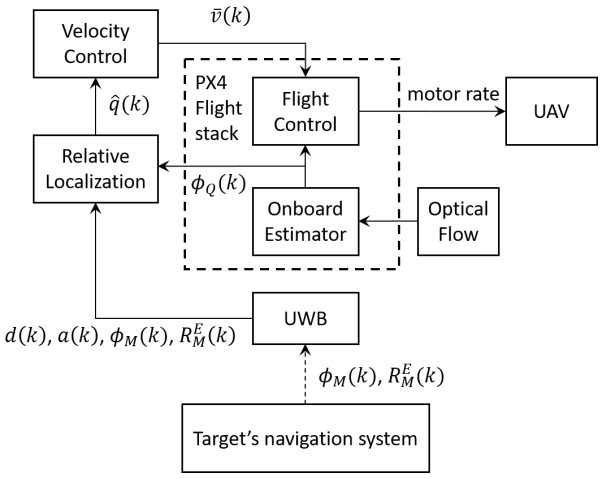

FIGURE 5.3: The estimation-control scheme in the approaching phase. See Section 5.2.2.1 for more details.

other onboard measurements in an EKF-based *onboard estimator* similar to that in Chapter 3 to obtain the displacement measurement $\phi_Q(k)$.

Secondly, the target's orientation $R_M^E(k)$ and displacement measurement $\phi_M(k)$ (which is obtained from some navigation system mounted on the target, e.g SLAM or visual-inertial odometry) will be sent to the MAV via the same UWB ranging message.

Finally, with the information $d(k)$, $a(k)$, $\phi_Q(k)$, $\phi_M(k)$, $R_M^E(k)$, a recursive least-squares optimization algorithm will be employed to provide an estimate $\hat{q}(k)$ of the relative position $q(k)$. Based on this estimate, a velocity command $\bar{v}(k)$ is calculated and sent to the onboard flight controller to drive the MAV towards the target. Specifically, $\bar{v}(k)$ is generated by the following simple negative feedback control rule with saturation:

$$\bar{v}(k) = \frac{U_Q}{\max\{U_Q, K_p \|\hat{q}(k)\|\}} \left[-K_p \hat{q}(k)\right], \tag{5.1}$$

where $U_Q > 0$ is the maximum speed desired for the MAV and $K_p > 0$ is the proportional gain.

5.2.2.2 Landing

As the MAV approaches the platform and the optical flow may become unreliable (we found that normal asphalt surface yields more accurate displacement measurement than the landing pad's black and white surface), we will switch to a different estimate-control scheme for more efficient and accurate landing. Specifically, upon the first detection of the visual marker, we will transition to the landing phase where optical flow data is disabled, then both vision and UWB measurements are fused with IMU data in the onboard estimator to facilitate a position-based control rule, which is detailed below.

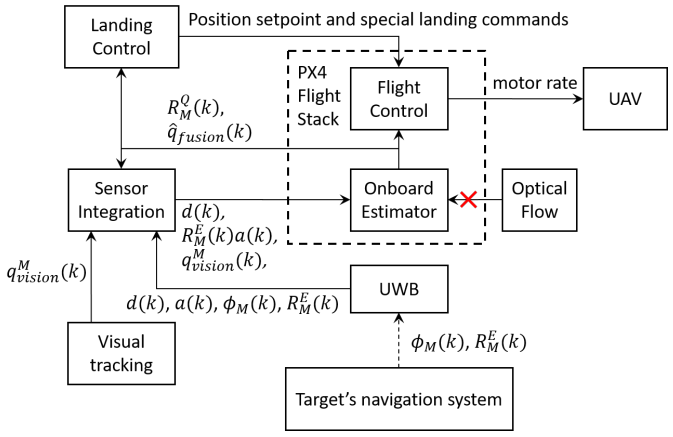

FIGURE 5.4: The estimation-control scheme in the landing phase. See Section 5.2.2.2 for more details.

As seen from Figure 5.4, we use the position $q_{vision}^M(k)$ of the MAV with respect to the target's body frame F_M as the new source of feedback in place of the optical flow. After retrieving $q_{vision}^M(k)$ from visual tracking information, we can obtain $R_M^E(k)q_{vision}^M(k)$ as an observation of the relative position $q(k)$, and fuse it into the onboard estimator to generate the relative position estimate $\hat{q}_{fusion}(k)$. Moreover, to make up for temporary losses of vision, we also fuse distance measurement into the onboard estimator by invoking the observation model $d(k) = \left\|q(k) - R_M^E(k)a(k)\right\|$ in the same manner with the EKF-based fusion scheme in Chapter 3.

Finally, using the onboard estimator estimate $\hat{q}_{fusion}(k)$ of the relative position $q(k)$, the flight control unit can drive the MAV to the center of the target. We impose that the MAV will only descend when $\hat{q}_{fusion}(k)$ is within a proximity of the center and automatically cut off the throttle when the altitude is below a threshold.

5.3 Relative Localization Algorithm

In this section we will discuss the derivation of the recursive least-squares estimation algorithm along with the theoretical analysis of the convergence.

First, some standard assumptions will be stated.

5.3.1 Assumptions

To ensure a unique solution for the cost function defined in the later parts, it is necessary that there are sufficient anchors whose coordinates are linearly independent. In other words, the anchors must not be co-linear in 2D case, or co-planar in 3D case, which is more formally stated as follows:

Assumption 5.1. *For $q(k) \in \mathbb{R}^m$, $m \in \{2, 3\}$, there exist $k_1, \ldots\ k_m \in \{1, 2, \ldots N\}$ such that* $\text{rank}[b(k_1) \ldots\ b(k_m)] = m$, *where $b(k_i) \triangleq a(k_i) - a(k_i - 1)$ and $a(N) \equiv a_0$.*

Since both MAV and UGV are physical systems, we also assume that the average relative velocity $u(k) \triangleq u_Q(k) - u_M(k)$ and the target's rotation rate $\omega(k)$ are all bounded:

Assumption 5.2. *There exist positive constants U and Ω such that $\|u(k)\| \leq U$ and $|\omega(k)| \leq \Omega$ for all k.*

Remark 5.1. *The aforementioned constraints can also be enforced via some control laws with saturation as in (5.1). Moreover, to successfully catch up with the UGV, the maximum speed of the MAV should be higher than that of the UGV.*

In section 4.4, we will study the EC of the relative localization algorithm under the condition that the sampling period T is sufficiently small, specifically:

$$T < \frac{g(B^*)}{\sqrt{m}[U + (2N-1)a_M\Omega]},\ \hat{q}(k) \in \mathbb{R}^m, \tag{5.2}$$

where $a_M = \max_{0 \leq i \leq N-1} \|a_i\|$ (a_i is the coordinate of anchor i as defined in section 5.2.1), m, U and Ω are defined in Assumptions 5.1, 5.2, $g(B) = \varsigma_M(B) - \sqrt{\varsigma_M^2(B) - \varsigma_m^2(B)}$ and $B^* = \arg\max_{B \in \mathcal{B}} g(B)$, where $\mathcal{B} = \{B = [b_{k_1} \ldots b_{k_m}] : k_1 \ldots k_m \in \{1, 2, \ldots N\}\}$.

5.3.2 Parametric Model

Note that in this section we simplify the notation $R_M^E(k)$ as $R(k)$. By recalling the definitions defined in Section 5.2.1 and Figure 5.1, we can verify the following relationship between $q(k)$ and the measurements $d(k)$, T, $u(k)$, $R(k)$ and $a(k)$:

$$d^2(k) = [q(k-1) + Tu(k) - R(k)a(k)]' [q(k-1) + Tu(k) - R(k)a(k)], \tag{5.3}$$
$$d^2(k-1) = [q(k-1) - R(k-1)a(k-1)]' [q(k-1) - R(k-1)a(k-1)]. \tag{5.4}$$

Noticing that $R'(k)R(k) = I$, one can expand the right hand side of the previous equations and obtain the following

$$\begin{aligned} d^2(k) - d^2(k-1) = &\|q(k-1)\|^2 + T^2\|u(k)\|^2 + \|a(k)\|^2 \\ &+ 2Tu'(k)q(k-1) - 2a'(k)R'(k)q(k-1) \\ &- 2Tu'(k)R(k)a(k) \\ &- \|q(k-1)\|^2 - \|a(k-1)\|^2 \\ &+ 2a'(k-1)R'(k-1)q(k-1) \\ = &T^2\|u(k)\|^2 + \|a(k)\|^2 - \|a(k-1)\|^2 \\ &- 2Tu'(k)R(k)a(k) \\ &+ 2[Tu(k) - R(k)a(k) + R(k-1)a(k-1)]' q(k-1). \end{aligned} \tag{5.5}$$

From this relationship, denote the following quantities

$$\begin{aligned} \zeta(k) = \frac{1}{2}\Big[&d^2(k) - d^2(k-1) - T^2\|u(k)\|^2 \\ &- \|a(k)\|^2 + \|a(k-1)\|^2 + 2Tu'(k)R(k)a(k)\Big], \end{aligned} \tag{5.6}$$
$$\varphi(k) = Tu(k) - R(k)a(k) + R(k-1)a(k-1). \tag{5.7}$$

Thus, by comparing (5.5), (5.6), and (5.7) we can obtain a similar parametric model as in Chapter 4:

$$\zeta(k) = \varphi'(k)q(k-1). \tag{5.8}$$

5.3.3 Cost Function and Estimation Update Law

With the parametric model (5.8), let us define $\hat{q}(k)$ as the estimate of $q(k)$ that minimizes the following cost function:

$$\begin{aligned} J(k) = \frac{1}{2}\sum_{i=1}^{k}\beta_f^{k-i}\big[\zeta(i)-\varphi(i)'(\hat{q}(k)-\sum_{j=i}^{k}Tu(j))\big]^2 \\ +\frac{1}{2}\beta_f^k\big[\hat{q}(k)-\sum_{j=1}^{k}Tu(j)-\hat{q}(0)\big]'\Gamma^{-1}(0)\big[\hat{q}(k)-\sum_{j=1}^{k}Tu(j)-\hat{q}(0)\big], \end{aligned} \tag{5.9}$$

where $\hat{q}(0)$ is the initial value of $\hat{q}(k)$, $\Gamma(0)$ is a positive definite matrix, and $\beta_f < 1$ is a positive constant.

By solving $\dfrac{\partial J(k)}{\partial \hat{q}(k)} = 0$, we obtain the estimator of $\hat{q}(k)$ as follows:

$$\begin{cases} \epsilon(k) = \zeta(k) - \varphi'(k)\hat{q}(k-1), & \text{(5.10a)} \\ \mathit{\Gamma}(k) = \dfrac{1}{\beta_f}\left[\mathit{\Gamma}(k-1) - \dfrac{\mathit{\Gamma}(k-1)\varphi(k)\varphi'(k)\mathit{\Gamma}(k-1)}{\beta_f+\varphi'(k)\mathit{\Gamma}(k-1)\varphi(k)}\right], & \text{(5.10b)} \\ \hat{q}(k) = \hat{q}(k-1) + Tu(k) + \mathit{\Gamma}(k)\varphi(k)\epsilon(k), & \text{(5.10c)} \end{cases}$$

where $0 < \beta_f < 1$, $\mathit{\Gamma}(k) \in \mathbb{R}^{m\times m}$ and $\mathit{\Gamma}(0) = \gamma I$ with $\gamma > 0$.

Remark 5.2. *The aforementioned cost function and algorithm are inspired by the least-squares-based optimization technique with the forgetting factor in the adaptive control literature [123]. However this method is usually used to estimate an unknown constant parameter θ that takes the place of $q(k)$ in (5.8). Here, the algorithm is modified for the case of a time-varying parameter whose rate of change is measurable through $u(k)$. Furthermore, compared with the gradient-based method proposed used in Chapter 4, we make full use of all historical data, which not only improves convergence rate, but also robustness to outliers.*

Remark 5.3. *A 3D implementation of algorithm (5.10) requires that the anchor nodes have variable heights relative to the platform, which can be unnecessarily inconvenient in most practical scenarios. To avoid this issue, we implement a 2D version of algorithm (5.10) in our experiment by removing the vertical component from the distance measurement (since UWB sensor only measures the distance between two points in 3D space). More specifically, if we denote $d^U(k)$ as the*

distance directly measured by the UWB sensors, $d^L(k)$ as the altitude of the MAV relative to the ground as measured by some altimeter sensors, and h as the height of the platform, we can obtain $\sqrt{(d^U(k))^2-(d^L(k)-h)^2}$ as the "horizontal" distance to the anchor. This value is then used as $d(k)$ in algorithm (5.10).

5.3.4 Convergence of Estimation Error

The EC theorem is stated as follows,

Theorem 5.1. *Let Assumptions 5.1 and 5.2 hold. Under condition (5.2), there exist $\alpha_1>0$ and $\alpha_2>0$ such that $\varphi(k)$ satisfies the PE condition as follows:*

$$\rho_1 I \leq \Phi(n) \triangleq \sum_{k=n}^{n+N-1} \varphi(k)\varphi'(k) \leq \rho_2 I,\ \forall n \geq 1. \tag{5.11}$$

As a consequence, the relative position estimate $\hat{q}(k)$ will converge to the true value $q(k)$ exponentially fast under the update law (5.10).

Proof. We firstly note that $\Phi(n)=\sum_{k=n}^{n+N-1}\varphi(k)\varphi'(k)$ is a summation of $\varphi(k)\varphi'(k)$ over an interval N (N is the number of anchors). Since $\varphi(k)=Tu(k)-R(k)a(k)+R(k-1)a(k-1)$ and $a(k)$ takes value from a_0 to a_{N-1} periodically, it incurs no loss of generality to only show (5.11) for $\Phi(1)$. Below we will show $\rho_1 I \leq \Phi(1) \leq \rho_2 I$ by two steps.

1) $\Phi(1) \leq \rho_2 I$. Equivalently, we will show that there exists $\rho_2>0$ such that $x'\Phi(1)x \leq \rho_2$ for any unit vector x. By recalling (5.7) it holds that

$$\varphi(k) = R_0 b(k) + c(k), k = 1, 2, \ldots, N, \tag{5.12}$$

where $b(k)=a(k)-a(k-1)$ and $c(k)=Tu(k)+(R_0-R(k))a(k)+(R(k-1)-R_0)a(k-1)$. By recalling Assumption 5.2 as well as $\|R(k)a_i-R(k-1)a_i\| \leq T\|a_i\|\,|\omega(k)|$ in Figure 5.2, we get that

$$\begin{aligned}\|c(k)\| &\leq TU + Ta_M N\Omega + Ta_M(N-1)\Omega \\ &\leq T[U+(2N-1)a_M\Omega] \triangleq c(T).\end{aligned} \tag{5.13}$$

Direct computation shows that

$$\begin{aligned} x'\Phi(1)x &\leq \sum_{k=1}^{N}(\|b(k)\|^2 + 2\|c(k)\|\,\|b(k)\|^2 + \|c(k)\|^2) \\ &\leq N(2a_M + c(T))^2 \triangleq \rho_2, \end{aligned} \tag{5.14}$$

where we used $\|R_0'x\| = \|x\| = 1$, (5.13), and $\|b(k)\| \leq 2a_M$, as well as the Cauchy-Swartz inequality. Thus $\Phi(1) \leq \rho_2 I$.

2) $\Phi(1) \geq \rho_1 I$. Equivalently, we will show that there exists $\rho_1 > 0$ such that $x'\Phi(1)x \geq \rho_1$ for any unit vector x. Let us select $b_{k_1}, \ldots b_{k_n}$ satisfying Assumption 5.1, and denote $B = [b_{k_1} \ldots b_{k_n}]$. We have $\Phi(1) \geq \varphi_{k_1}\varphi_{k_1}' + \cdots + \varphi_{k_n}\varphi_{k_n}'$. Direct computation shows that

$$\begin{aligned} x'\Phi(1)x &\geq \|x'R_0B\|^2 - 2x'CB'R_0'x + \|C'x\|^2 \\ &\geq \varsigma_m^2(B) - 2\varsigma_M(B)\|C'x\| + \|C'x\|^2, \end{aligned} \tag{5.15}$$

where $\varsigma_m(B)$ and $\varsigma_M(B)$ are respectively the smallest and the largest singular values of B, and $C = [c_{k_1} \ldots c_{k_n}]$. Note that $\varsigma_M(B) \geq \varsigma_m(B) > 0$ by Assumption 5.1. Clearly, it suffices to show that $\varsigma_m^2(B) - 2\varsigma_M(B)\|C'x\| + \|C'x\|^2 \geq \rho_1$ for some $\rho_1 > 0$. Noticing that $\|C'x\| \leq \sqrt{n}c(T)$, we can see that if $\rho_1 < \varsigma_m^2(B)$, then the above can be achieved with $c(T) \leq (\varsigma_M(B) - \sqrt{\varsigma_M^2(B) - \varsigma_m^2(B)})/\sqrt{n}$. Taking $B = B^*$ in (5.2), we have shown that $\Phi(1) \geq \rho_1 I$.

By combining 1) and 2) we obtain the PE condition of $\varphi(k)$. To study the convergence rate, let us denote $\tilde{q}(k) \triangleq \hat{q}(k) - q(k)$ as the estimation error. By comparing (5.10a) and (5.8), we have $\epsilon(k) = -\varphi'(k)\tilde{q}(k-1)$. By substituting this into (5.10c) and subtracting both sides by $q(k)$, one has $\tilde{q}(k) = A(k)\tilde{q}(k-1)$, where $A(k) \triangleq I - \Gamma(k)\varphi(k)\varphi(k)'$. Combining with (5.10b), we can prove the EC of $\tilde{q}(k)$ along a similar line as in the Theorem 1 of [125]. ■

5.4 Experiment

In this part we will first describe our experiment setup and then present and comment on the main experimental results. Note that the algorithm presented in

Section 5.3 is implemented in a 2D scenario as explained in Remark 5.3. The video recording of our tests can be viewed at https://youtu.be/08yU9LqLTto.

5.4.1 Experiment Setup

Our system is implemented on a hexacopter frame equipped with a *PX4 Autopilot*[1] flight controller computer, which also provides IMU measurements. A down-facing camera is mounted below the MAV to provide color images with a resolution of 320 × 240 pixel at 60Hz, hosted by an Intel NUC Core i7 Mini Computer. A laser range finder is used to directly measure the relative altitude (we assume that the platform's elevation from the ground is insignificant). Optical flow sensor[2] is used for velocity estimation. We refer to our previous works [13, 70] for a detailed description of the operation principle, advantages and limitations of UWB.

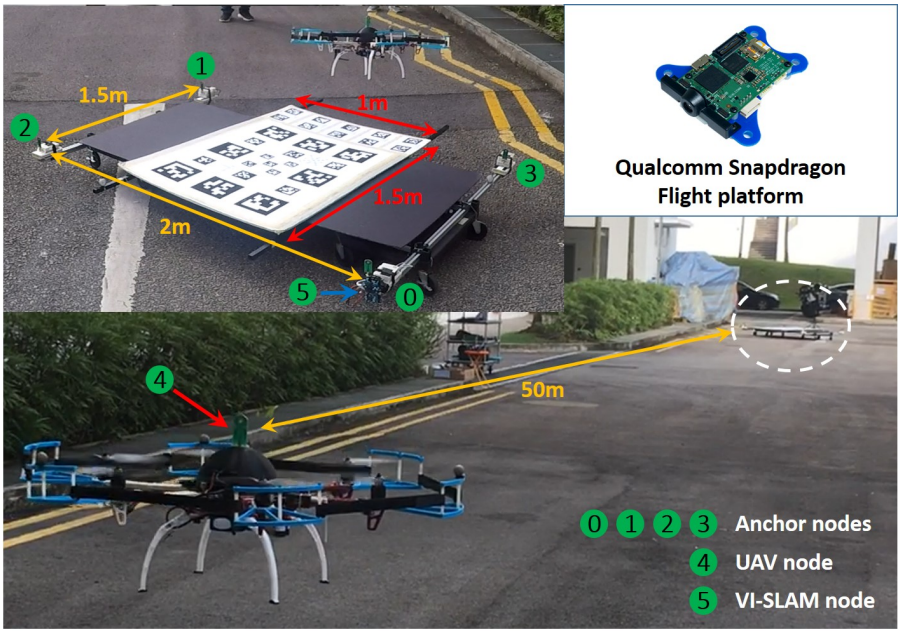

FIGURE 5.5: Experimental setup: four anchor nodes are mounted on a flat mobile platform. The ranging sequence from the MAV node (4) is indicated by the number associated with each anchor in the figure (0-3). VI-SLAM node (5) is attached to anchor node (0), with the camera facing forward.

The landing platform is equipped with four UWB sensors attached to four corners of a 2m×1.5m rectangle at the same height level, one Qualcomm Snapdragon Flight board[3] attached to one of the anchors facing forward to provide VI-SLAM data,

[1] http://px4.io
[2] https://docs.px4.io/en/sensor/px4flow.html
[3] https://developer.qualcomm.com/hardware/qualcomm-flight

and one landing pad with markers on top. In this chapter, we use a visual tracking technique based on AprilTag 2 [126] with a specifically designed pattern consisting of tags with various sizes to keep the visual features within the camera's FOV at both far and close distances, as shown in Figure 5.5. As the MAV descends on the landing pad, larger tags will eventually leave the camera's FOV, while smaller ones towards the centre become detectable. Despite these considerations, we do not assume that the landing pad is always within the camera's FOV. Thus, visual position from AprilTag, UWB range measurements, and inertial data from the flight controller's IMU are fused together in the landing phase to ensure continuing relative localization and tracking for precise landing.

5.4.2 Results and Analysis

Three sets of experiments are carried out to investigate the performance of the system in different scenarios.

5.4.2.1 Static Target

In the first set of experiments, a total of five flight tests were carried out in an 6m×6m indoor area with an overhead motion capture system to record the positions of the target as well as the MAV for ground truth. Due to the limited size of the testing area, we tested the algorithm with a static platform. However, in each test, we rotated the platform to a different direction before the MAV started flying. After this, the MAV was controlled manually to take off and move around the target for some time to record the relative position estimate at different directions. Then, the autonomous mode was enabled and the MAV began executing the aforementioned estimation-control schemes to approach and land on the platform.

TABLE 5.1: RMS error and SD of relative position estimates (unit: m).

Exp.	rms($\tilde{q}_x$)	rms($\tilde{q}_y$)	sd($\tilde{q}_x$)	sd($\tilde{q}_y$)
1	0.1348	0.2317	0.0956	0.1197
2	0.1677	0.1639	0.0976	0.1391
3	0.1561	0.1216	0.1198	0.0819
4	0.1717	0.0968	0.1349	0.0827
5	0.1685	0.0995	0.0619	0.0575

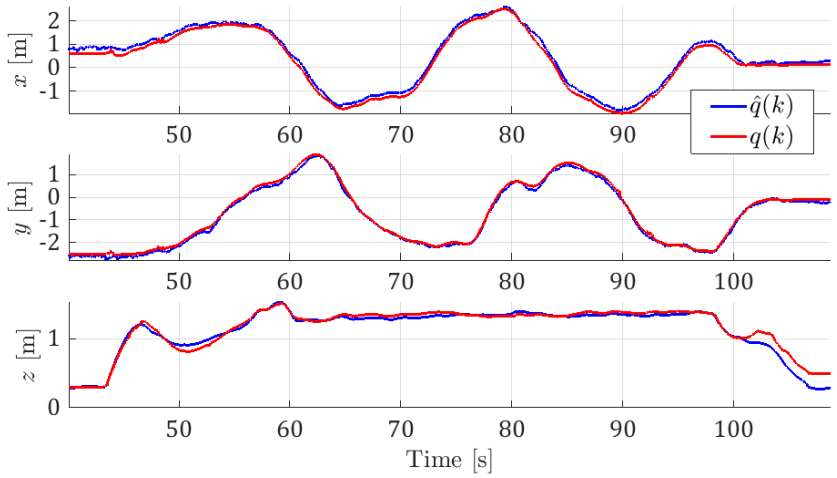

FIGURE 5.6: Relative position estimate and ground truth in an indoor experiment (the vertical estimate is obtained directly from the laser's range finder measurement, hence we can see some small offset during the landing phase at the end due to the height of the UGV relative to the ground).

We collected the data of all five experiment results and made some analyses. Table 5.1 shows the RMS and SD values of the relative position error. Figure 5.6 shows the relative position estimate together with the ground truth of one flight test. It can be seen that the average error in the position estimate is around 20 cm, which is obviously adequate for the docking operation.

5.4.2.2 Moving Target

In the second set of experiments, so called chasing experiments, five more flight tests were conducted in an outdoor environment. In these tests, the MAV took off at some distance from the target and was switched to autonomous mode to chase after the moving platform. In Figure 5.7, we show the trajectories of both the target and the MAV in one of these tests. Note that $p_M^E(k)$ denotes the UGV's planar trajectory as measured by its visual odometry system in the frame F_E. Thus the MAV's estimated trajectory can be visualized by adding the relative position estimate $\hat{q}(k)$ to $p_M^E(k)$.

As no ground truth is available in this outdoor scenario, we use the distance measurement to represent the successful pursuit and landing on the target of the MAV. Figure 5.8 shows the distance measurements to the four anchors on the target in all five tests. It can be seen that from a far distance, as the MAV successfully lands on the target, all of the distances decrease to approximately 1.25m, which corresponds

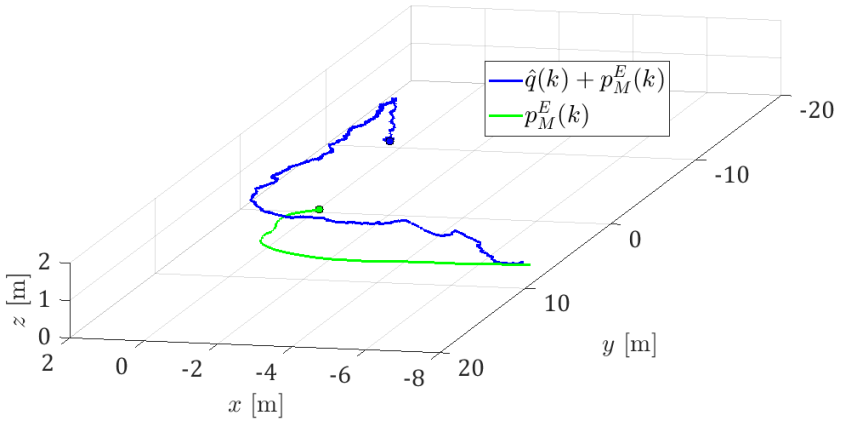

FIGURE 5.7: Trajectories of the MAV and the target relative to the starting point of the target. The starting point of each trajectory is marked by a solid circle. A successful landing can be observed at the end of the trajectories as they coincide.

to a landing spot at the center of the 2m×1.5m platform with 4 anchors at the corners.

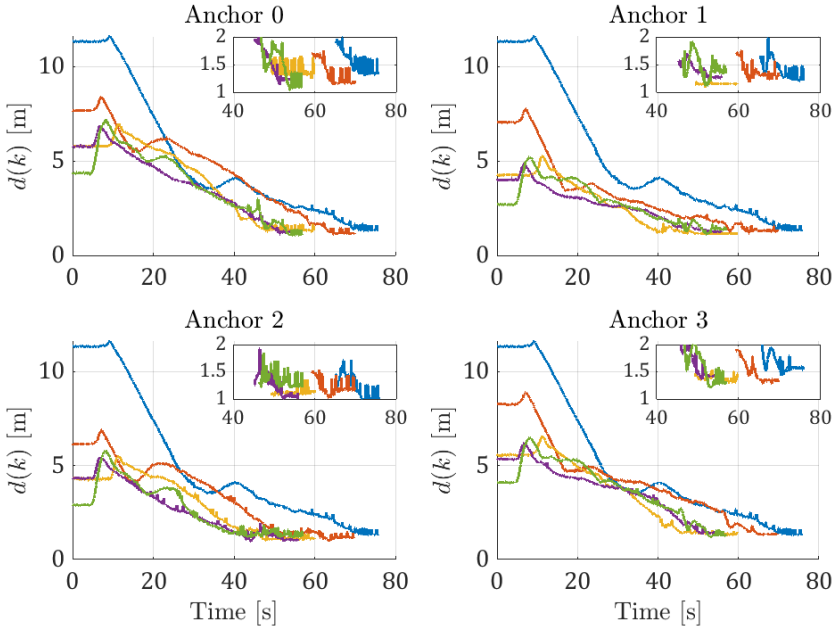

FIGURE 5.8: Distances from the MAV to the 4 anchors as measured by UWB in the second set of experiments (the measurements in the same experiment use the same color for each subplot). From some starting position, all distances reduce to 1.25 m in the end, which reflects the successful docking task.

5.4.2.3 Distant Static Target

In the final set of experiments, to validate the extent to which MAV can approach the platform, we moved the MAV to a location that is 50 m from the starting position. The platform was kept static in this case. As can be seen in Figure 5.9, all of the distances still decrease to approximately 1.25 m, which verifies the capability of the MAV to approach and land on the target from about 50m away. We are confident that the method can still work at a much longer distance.

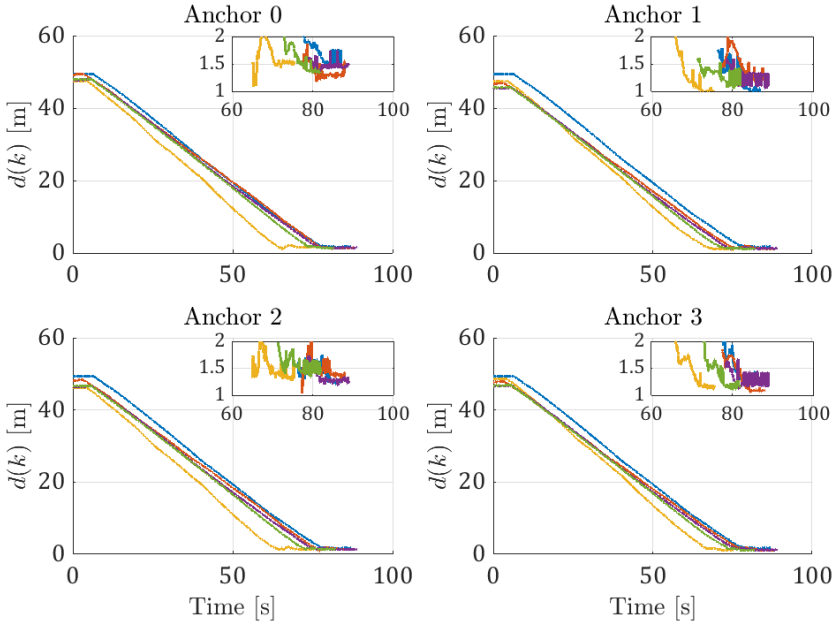

FIGURE 5.9: Distances from the MAV to the 4 anchor as measured by UWB in the third set of experiments. From 50 m away, all distances reduce to 1.25 m in the end, which reflects the successful docking task.

5.5 Conclusions

In this chapter we have combined the key findings in the two previous chapters to develop a system to achieve autonomous docking capability for a quadcopter using distance and displacement measurements. Our technique complements the conventional vision-based landing techniques with a flexible relative localization scheme to allow the MAV to approach the target without the use of any external positioning information. Real-world experiments were conducted to demonstrate the efficacy of the proposed scheme.

Chapter 6

Distance-Based Cooperative Relative Localization for Leader-following MAVs

6.1 Introduction

In this chapter, we will turn our focus to multi-MAV systems. As a first step, we will investigate a basic distributed simultaneous relative localization and control of multiple MAVs under the following premise: given a group of MAVs, design a estimation-control scheme for the MAV to follow the leader without relying on external localization information. To fulfill such cooperative operation of multi-MAV systems, we will again employ the relative localization technique leveraging distance and displacement measurements developed in the last two chapters. Note that in Chapter 4, the estimation error was shown to be asymptotically convergent by invoking the LaSalle's invariance principle and examining all possible trajectories in the invariant set. On the other hand, in Chapter 5, a similar estimator was developed and the estimation error was shown to be e.c. thanks to the PE feature achieved by the strategic installation of the anchor nodes on the target. In this chapter, we will again seek to achieve the PE condition by the development of *specialized* MAVs called *orbiters*. Specifically, the MAVs are separated into two groups as *orbiters* and *followers*: the orbiters are to track the leader with a predefined periodic trajectory that satisfies a PE condition, and the followers are to track

a pre-defined setpoint relative to the leader. We first study the basic case when there exist one orbiter and one follower. For the orbiter which can communicate with and range to the leader, we design a corresponding estimation-control law by using distance and displacement measurements, and show that both the localization error and the tracking error would converge to zero exponentially fast. For the follower which can communicate with and range to the other two MAVs, we design similar estimation-control laws and achieve similar EC results. The extension to a general hierarchy system is also discussed.

Several contributions are made when compared with previous works [73, 74, 103, 110, 114, 115]. Most importantly, the proactive introduction of the orbiter enables the PE condition by maintaining a predefined trajectory, which aids the cooperative localization for all the following MAVs and results in EC of both localization and tracking errors. Moreover, while previous works required quite a few types of continuous-time measurements, we propose a discrete-time relative localization algorithm using only discrete-time distance and displacement measurements that can be directly obtained from practical sensors. Finally, real-life experiments have been conducted to validate the proposed method.

This chapter is organized as follows: we first focus on a basic structure of three MAVs, by formulating the problem in Section 6.2, presenting the estimation and control laws of the cooperative relative localization scheme in Section 6.3, and conducting the convergence analysis in Section 6.4. Then we discuss the extension of this basic structure to a general hierarchical structure in Section 6.5. Simulation and experiment results are respectively provided in Sections 6.6 and 6.7 to validate the theoretical findings and demonstrate the practicality of the proposed algorithm. We conclude the chapter in Section 6.8.

6.2 Problem Formulation

Note that in this chapter, we may refer to the MAVs in general as agents. As introduced earlier, we will first consider a basic structure with 3 agents labelled as 0, 1, and 2. Agent 0 is called the *leader* which serves as a reference point, to which all other agents will estimate their relative positions via a cooperative localization scheme. Moreover, agent 1 is referred to as the *orbiter* and agent 2 as the *follower*.

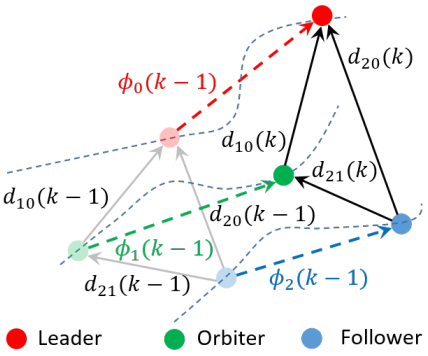

FIGURE 6.1: An illustration of the collaborative ranging and communication scheme executed by three agents: at time kT agent 1 measures the distance $d_{10}(k)$ to agent 0 and receives agent 0's displacement $\phi_0(k-1)$ via the UWB communication; on the other hand, agent 2 would obtain such measurements from both agent 0 and agent 1.

The ranging and communication relationships between these agents are illustrated in Figure 6.1. Note that we call agent j as a neighbour of agent i if either agent can range to the other.

Below, we will give the detailed definitions of some basic concepts before stating our objectives.

6.2.1 Basic Definitions

6.2.1.1 Dynamic Model

Denote $p_i(k) \in \mathbb{R}^m$ as the position of agent i in some fixed frame of reference at time kT, where T is the sampling period. We also denote $\bar{u}_i(k)$ as the velocity of agent i, and assume that it has the following discrete-time single integrator dynamics with maximum velocity $\bar{U}_i$:

$$p_i(k+1) = p_i(k) + T\bar{u}_i(k), \ \|\bar{u}_i(k)\| \leq \bar{U}_i < \infty, \ \forall k. \tag{6.1}$$

6.2.1.2 Sensing Models

For an agent i, it can obtain the relative distance to a neighbour agent j as follows:

$$d_{ij}(k) = \|p_i(k) - p_j(k)\|. \tag{6.2}$$

In addition, we assume that each agent can obtain the displacement measurement of itself and its neighbours (via communication) to calculate the relative displacement:

$$\phi_{ij}(k) \triangleq \phi_i(k) - \phi_j(k),\ \ \phi_i(k) \triangleq p_i(k+1) - p_i(k). \tag{6.3}$$

Remark 6.1. *While the estimation methods in previous works require at least three types of continuous-time measurements (distance, derivative of distance, and relative velocity as in [74]; or distance, relative velocity, and relative acceleration as in [110]), our method only requires two types of discrete-time measurements that can be directly obtained from generic sensors. Morover, in continuous-time formulation, the requirement on acceleration and/or velocity from neighbours implies that an agent needs to know the instantaneous control input of its neighbour, which is not very practical. In comparison, it can be seen from (6.3) that in the absence of noise and disturbance, the displacement measurement at the time step k is equal to the control input at the previous step $k-1$, which is essentially different from communicating instantaneous control input in [74] and [110].*

6.2.2 Relative Localization and Tracking Objectives

Define the relative position between two agents i and j at time kT as $q_{ij}(k) \triangleq p_i(k) - p_j(k)$. Moreover, denote $\hat{q}_{ij}(k)$ as the estimate of $q_{ij}(k)$, and the relative *localization error* as $\tilde{q}_{ij}(k) \triangleq \hat{q}_{ij}(k) - q_{ij}(k)$. The relative localization and tracking objectives are stated as follows: given predefined relative position setpoints q_{10}^* and $q_{20}^* \in \mathbb{R}^m$, as well as a predefined trajectory $\{\sigma(k)\}_{k=0}^{\infty} \subset \mathbb{R}^m$, design a set of update laws for $\hat{q}_{i0}(k)$ and $\bar{u}_i(k)$ so that the following can be achieved:

$$\lim_{k\to\infty} \|\tilde{q}_{i0}(k)\| = \lim_{k\to\infty} \|\hat{q}_{i0}(k) - q_{i0}(k)\| = 0,\ \ \forall i; \tag{6.4}$$

$$\lim_{k\to\infty} \|q_{10}(k) - q_{10}^* - \sigma(k)\| = 0; \tag{6.5}$$

$$\lim_{k\to\infty} \|q_{20}(k) - q_{20}^*\| = 0. \tag{6.6}$$

Henceforth, we refer to $\bar{q}_{10}(k) \triangleq q_{10}(k) - q_{10}^* - \sigma(k)$ and $\bar{q}_{20}(k) \triangleq q_{20}(k) - q_{20}^*$ as the *tracking error*.

In the sequel, for the aforementioned agents, as well as those in an extended system that will be introduced in Section 6.5, we will show that all localization errors are

e.c., i.e. there exist constants $\tilde{\eta}_{i0} > 0$ and $\tilde{\lambda}_{i0} \in (0, 1)$, whose values depend on the initial localization and tracking errors $\tilde{q}_{j0}(0)$ and $\bar{q}_{j0}(0)$ of all agents j, such that $\|\tilde{q}_{i0}(k)\| \leq \tilde{\eta}_{i0}\tilde{\lambda}_{i0}^{k}$ for all $k \in \mathbb{N}$. Based on the EC of the localization error, tracking errors can also be shown to be e.c.

Remark 6.2. *The use of the setpoint q_{i0}^{*} in (6.5) and (6.6) resembles a geometric formation control scheme; however, this resemblance only holds for the followers, but not the orbiters which are to track the leader with a predefined trajectory instead of at a setpoint.*

Remark 6.3. *In chapter 4, $\sigma(k)$ was required to be generated from an autonomous process due to the use of the LaSalle's Invariant Principle, which addresses asymptotic stability of autonomous system. As such we had to design a process that ensures $\sigma(k)$ satisfies Assumption 4.1 regardless of initial condition $\sigma(0)$. However, in this work this requirement is no longer required and $\sigma(k)$ can be chosen as a time-dependent periodic process with finite period and a minimum level of excitation. More details of this are given in Section 6.2.3.*

6.2.3 Main Assumptions

We adopt the following assumptions in this problem:

Assumption 6.1. *There exist $N \in \mathbb{N}^{+}$ and $\rho \in \mathbb{R}^{+}$ such that $\sigma(k+N) = \sigma(k)$ and $\max_{W \in \mathcal{W}} g(W) = \rho > 0$, where*

$$g(W) \triangleq \varsigma_M(W) - \sqrt{\varsigma_M^2(W) - \varsigma_m^2(W)}; \tag{6.7}$$

$$\mathcal{W} = \big\{W \triangleq [\Delta\sigma(k_1) \ \dots \ \Delta\sigma(k_m)] \in \mathbb{R}^{m\times m} : \\ 0 \leq k_1 < \cdots < k_m \leq N-1, \ \det(W) \neq 0\big\}; \tag{6.8}$$

$$\Delta\sigma(k) = \sigma(k+1) - \sigma(k), \ \forall k \in \mathbb{N}. \tag{6.9}$$

Assumption 6.2. *At time k, agent i can obtain the relative position setpoint q_{j0}^{*} and the position estimate $\hat{q}_{j0}(k-1)$ of the neighbour agent j, as well as the team velocity command $v(k) \triangleq \bar{u}_0(k)$ from the leader.*

Remark 6.4. *Assumption 6.1 is motivated by a practical interpretation of the PE condition. Specifically, to achieve PE in the displacement of the orbiters, we employ a periodic trajectory $\{\sigma(k)\}_{k=0}^{\infty}$ so that the set of predetermined displacements*

$\{\Delta\sigma(k)\}_{k=0}^{\infty}$ will consist of recurring bases of $\mathbb{R}^m$ for every N steps. By finding the basis W with the largest level of excitation ρ, we can choose proper parameters in the tracking control law to preserve the PE condition, which will be shown in Theorem 6.1.

Remark 6.5. *The team velocity $v(k) \triangleq \bar{u}_0(k)$ stipulated in Assumption 6.2 is to coordinate the movement of the MAV team. In practice this can be implemented by using the broadcast mode of UWB, or by using a predefined trajectory running in the software program of all agents [17]. Note that it also implies that at time k, all agents can calculate the displacement of the leader from the value of team velocity in the previous time step, i.e. $T\bar{u}_i(k-1)$.*

6.3 Integrated Localization-Navigation

In this section we shall design an estimator for the relative localization and a controller for the navigation task. Specifically, the estimator and the controller are constructed by adaptive control techniques, which depends on the following parametric model for agents i and j:

$$\phi'_{ij}(k)q_{ij}(k) = \zeta_{ij}(k), \tag{6.10}$$

where $\zeta_{ij}(k)$ is a scalar observation combining the distance and displacement measurements as follows:

$$\zeta_{ij}(k) \triangleq \frac{1}{2}[d_{ij}^2(k+1) - d_{ij}^2(k) - \|\phi_{ij}(k)\|^2]. \tag{6.11}$$

6.3.1 Orbiter

Based on the model (6.10), we can calculate the innovation $\epsilon_{10}(k)$ and update the relative position estimate of the orbiter as follows:

$$\begin{cases} \epsilon_{10}(k) \triangleq \zeta_{10}(k) - \phi'_{10}(k)\hat{q}_{10}(k), & \text{(6.12a)} \\ \hat{q}_{10}(k+1) = \hat{q}_{10}(k) + \phi_{10}(k) + \dfrac{\gamma\phi_{10}(k)\epsilon_{10}(k)}{\mu_\nu^2(\gamma\phi_{10}(k))}, & \text{(6.12b)} \end{cases}$$

where $\gamma > 0$ and $\mu_\nu(\cdot)$ is a normalizing function defined as follows:

$$\mu_\nu(x) \triangleq \sqrt{\max\{\nu, \|x\|^2\}/\nu}, \ \nu \in (0, 2). \tag{6.13}$$

Based on the above estimate, the control input is designed as

$$\begin{cases} \bar{u}_1(k) = \pi_U\left(u_1(k)\right) + T^{-1}\Delta\sigma(k) + v(k), & \text{(6.14a)} \\ u_1(k) = -\beta\left(\hat{q}_{10}(k) - q_{10}^* - \sigma(k)\right), & \text{(6.14b)} \end{cases}$$

where $\beta > 0$ and $\pi_U(\cdot)$ is the projection operation defined in (4.3).

Remark 6.6. *Note that the control law (6.14) is executed before the estimation law (6.12). The control input $\bar{u}_1(k)$ is generated at time step k from the relative position estimate $\hat{q}_{10}(k)$, which is updated from the measurements $d_{10}(k)$, $d_{10}(k-1)$ and $\phi_{10}(k-1)$ that are available at time k. On the other hand, the estimate $\hat{q}_{10}(k+1)$ is based on the measurements at time step $k+1$, which are available after the control $\bar{u}_1(k)$ has been executed.*

6.3.2 Follower

Notice the following parametric model for the follower:

$$\begin{aligned} \zeta_{21}(k) &= \phi_{21}'(k)q_{21}(k), \\ \zeta_{20}(k) &= \phi_{20}'(k)q_{20}(k) = [\phi_{21}(k) + \phi_{10}(k)]'q_{20}(k) \\ &= \phi_{21}'(k)[q_{21}(k) + q_{10}(k)] + \phi_{10}'(k)q_{20}(k) \\ &= \phi_{21}'(k)q_{21}(k) + \phi_{21}'(k)q_{10}(k) + \phi_{10}'(k)q_{20}(k), \\ \zeta_{20}(k) - \zeta_{21}(k) &= \phi_{10}'(k)q_{20}(k) + \phi_{21}'(k)q_{10}(k). \end{aligned}$$

Thus we can calculate the innovation $\epsilon_{20}(k)$ using available measurements and the orbiter's estimate to update the relative position estimate of the follower as follows:

$$\begin{cases} \epsilon_{20}(k) \triangleq \zeta_{20}(k) - \zeta_{21}(k) - \phi_{10}'(k)\hat{q}_{20}(k) - \phi_{21}'(k)\hat{q}_{10}(k), & \text{(6.15a)} \\ \hat{q}_{20}(k+1) = \hat{q}_{20}(k) + \phi_{20}(k) + \dfrac{\gamma\phi_{10}(k)\epsilon_{20}(k)}{\mu_\nu^2(\gamma\phi_{10}(k))}. & \text{(6.15b)} \end{cases}$$

The control input of the follower is designed as follows:

$$\begin{cases} \bar{u}_2(k) = \pi_U\left(u_2(k)\right) + v(k), & \text{(6.16a)} \\ u_2(k) = -\beta(\hat{q}_{20}(k) - q^*_{20}). & \text{(6.16b)} \end{cases}$$

Remark 6.7. *For the orbiter, the control law $\bar{u}_1(k)$ consists of three terms: the first one is the tracking term $\pi_U(u_i(k))$, the second one is the p.e. velocity $T^{-1}\Delta\sigma(k)$, and the third one is the team velocity $v(k)$. The control law $\bar{u}_2(k)$ of the follower forgoes the p.e. velocity term. Note that we use the projection $\pi_U(\cdot)$ in the tracking term for two purposes. First, it is to ensure that the control input does not exceed the maximum speed $\bar{U}_i$, since the bound for $u_i(k)$ cannot be predetermined, which is different from the team velocity and the p.e. velocity. Clearly, if $\|v(k)\| \leq U_0$ and $T^{-1}\|\Delta\sigma(k)\| \leq U_\sigma$, the projection $\pi_U(\cdot)$ is invoked to guarantee that $\|\bar{u}_i(k)\| < U_0 + U_\sigma + U \leq \bar{U}_i$ with $U \leq \bar{U}_i - U_0 - U_\sigma$. Second, the use of $\pi_U(\cdot)$ also ensures that $u_i(k)$ does not cancel out the p.e. components of $\Delta\sigma(k)$ (see Remark 6.4), as will be explained in more details in Section 6.4 and the proof of Theorem 6.1.*

Remark 6.8. *The rationale of naming agents* 1 *and* 2 *as orbiter and follower can be inferred from the proposed control laws. Specifically, by employing the control law (6.14), agent* 1 *is tasked with maintaining a p.e. trajectory $\sigma(k)$ as shown in Theorem 6.2. With the access to the p.e. displacement measurements from the orbiter, agent* 2 *can achieve EC for its position estimates as shown in Theorem 6.1, which leads to the asymptotic tracking of the leader at the setpoint as shown in Theorem 6.2.*

6.4 Convergence Analysis

In this section we shall study the convergence of localization error and tracking error respectively for the orbiter and the follower. Before getting into the details, let us gather all the parameters used in the estimation and control laws along with their conditions for convenience in reference:

$$\begin{cases} \nu \in (0, 2), \gamma > 0; & \text{(6.17a)} \\ U > 0,\ \beta \in (0,\ 1/T); & \text{(6.17b)} \\ \rho^* \triangleq \rho - \sqrt{m}TU > 0. & \text{(6.17c)} \end{cases}$$

Remark 6.9. *Note that conditions (6.17a) and (6.17b) are required to respectively ensure the stability of the estimator and the controller. In addition, ρ is the level of excitation for the trajectory $\sigma(k)$ defined in Assumption 4.1, and condition (5.2) is to preserve its p.e. characteristics in the presence of the tracking term $\pi_U(u_i(k))$ in the subsequent control law (6.14a). Thanks to this PE feature, the stable estimators and controllers can achieve EC.*

Let us move on to examining the convergence of the system. Notice that $q_{10}(k+1) = q_{10}(k) + \phi_{10}(k)$, $\tilde{q}_{10}(k) = \hat{q}_{10}(k) - q_{10}(k)$ and $\epsilon_{10}(k) = -\phi'_{10}(k)\tilde{q}_{10}(k)$. Substituting these to (6.12b) we find that the relative localization error has the following dynamics:

$$\tilde{q}_{10}(k+1) = \left[I - \frac{\gamma\phi_{10}(k)\phi'_{10}(k)}{\mu_\nu^2(\gamma\phi_{10}(k))} \right] \tilde{q}_{10}(k). \tag{6.18}$$

Moreover, after recalling (6.14b) and that $q_{10}(k+1) = q_{10}(k) + T\bar{u}_1(k)$, the tracking error $\bar{q}_{10}(k) = q_{10}(k) - q^*_{10} - \sigma(k)$ can be described by the following dynamics:

$$\bar{q}_{10}(k+1) = \bar{q}_{10}(k) + T\pi_U(u_1(k)). \tag{6.19}$$

For the follower, the dynamics of the localization error $\tilde{q}_{20}(k) = \hat{q}_{20}(k) - q_{20}(k)$ and the tracking error $\bar{q}_{20}(k) = q_{20}(k) - q^*_{20}$ can be similarly found respectively as:

$$\tilde{q}_{20}(k+1) = A(k)\tilde{q}_{20}(k) + B(k), \tag{6.20}$$

$$\bar{q}_{20}(k+1) = \bar{q}_{20}(k) + T\pi_U\left(u_2(k)\right), \tag{6.21}$$

where $A(k)$ and $B(k)$ are defined as:

$$A(k) = I - \mu_\nu^{-2}(\gamma\phi_{10}(k))\gamma\phi_{10}(k)\phi'_{10}(k), \tag{6.22}$$

$$B(k) = -\mu_\nu^{-2}(\gamma\phi_{10}(k))\gamma\phi_{10}(k)\phi'_{20}(k)\tilde{q}_{10}(k). \tag{6.23}$$

6.4.1 Localization Error Convergence

The EC of the relative localization error is established in the following theorem.

Theorem 6.1. *Under Assumptions 6.1, 6.2 and condition (6.17), $\phi_{10}(k)/\mu_{10}(k)$, $\mu_{10}(k) \triangleq \mu_\nu(\gamma\phi_{10}(k))$ is p.e., i.e.:*

$$S(n) \triangleq \sum_{k=n}^{n+N-1} \frac{\phi_{10}(k)\phi_{10}'(k)}{\mu_{10}^2(k)} \geq \rho^* I,\ \forall n \in \mathbb{N}^+. \tag{6.24}$$

As a result, under the estimation laws (6.12) and (6.15), the estimation errors $\tilde{q}_{10}(k)$ and $\tilde{q}_{20}(k)$ are e.c.

Proof. From (6.3), (6.14) and recalling that $v(k) = \bar{u}_0(k)$, we get that

$$\phi_{10}(k) = \Delta\sigma(k) + T\bar{v}_1(k),\ \bar{v}_1(k) = \pi_U\left(u_1(k)\right). \tag{6.25}$$

Clearly, (6.25) implies that $\|\phi_{10}(k)\| \leq TU + \delta_\sigma$, where $\delta_\sigma = \max\limits_{k\in\mathbb{N}^+}\{\|\Delta\sigma(k)\|\} = \max_{0\leq k\leq N-1}\{\|\Delta\sigma(k)\|\}$ holds as a result of the periodicity in Assumption 6.1. Therefore, we have

$$1/\mu_{10}(k) \geq \mu^* \triangleq 1/(\max\{\nu, \gamma(TU+\delta_\sigma)^2\}/\nu) > 0.$$

Consequently, $S_{10}(n) \geq \sum_{k=n}^{n+N-1}(\mu^*)^2\phi_{10}(k)\phi_{10}'(k) \triangleq (\mu^*)^2\Phi(n : n+N-1)$; moreover, by the periodicity we only need to check $\Phi(0 : N-1) \triangleq \Phi$, and the PE condition (6.24) holds if there exists $\rho_1 > 0$ such that $\Phi \geq \rho_1 I > 0$. Equivalently, we need to show that there exists $\rho_1 > 0$ such that for any unit vector $x \in \mathbb{R}^m$, it holds that $x'\Phi x \geq \rho_1$. Indeed, for any $W = [\Delta\sigma(k_1)\,\Delta\sigma(k_2)\,\ldots\,\Delta\sigma(k_m)] \in \mathcal{W}$, we can find that

$$\begin{aligned} x'\Phi x &\geq x'\sum_{j=1}^{m}\Big[\Delta\sigma(k_j)\Delta\sigma'(k_j) + T\Delta\sigma(k_j)\bar{v}_1'(k_j) \\ &\qquad + \bar{v}_1(k_j)\Delta\sigma'(k_j) + T^2\bar{v}_1(k_j)\bar{v}_1'(k_j)\Big]x \\ &= \|W'x\|^2 + 2T\langle V'x, W'x\rangle + T^2\|V'x\|^2 \\ &\geq \varsigma_m^2 - 2T\varsigma_M\|V'x\| + T^2\|V'x\|^2, \end{aligned} \tag{6.26}$$

where $V = [\bar{v}_1(k_1),\ \bar{v}_1(k_2)\ \ldots\ \bar{v}_1(k_m)]$, $\varsigma_m = \varsigma_m(W)$, and $\varsigma_M = \varsigma_M(W)$. Therefore, it suffices to let $\varsigma_m^2 - 2T\varsigma_M\|V'x\| + T^2\|V'x\|^2 > \rho_1 > 0$ for all unit vectors $x \in \mathbb{R}^m$, which can be satisfied by $T\|V'x\| \leq \varsigma_M - \sqrt{\varsigma_M^2 - (1-\rho_2)\varsigma_m^2}$ with $\rho_1 = \rho_2\varsigma_m^2$ and $\rho_2 \in (0,1)$. Moreover, note that $\|V'x\| \leq \|V\| \leq \sqrt{m}U$ and the arbitrariness of

$\rho_2 \in (0,1)$, we only need that

$$T\sqrt{m}U < \varsigma_M - \sqrt{\varsigma_M^2 - (1-\rho_2)\varsigma_m^2}.$$

Finally, as W is arbitrary, we can select W^* to maximize the right hand side of the above inequality as given in (6.17c).

2) With the PE condition (6.24), we can apply Lemma 4.1.1 of [123] to obtain the EC of $\tilde{q}_{10}(k)$ under the dynamics (6.18). Furthermore, considering the dynamics (6.20) of $\tilde{q}_{20}(k)$, as the term $B(k)$ is e.c. due to the EC of $\tilde{q}_{10}(k)$, we conclude that $\tilde{q}_{20}(k)$ is also e.c. ■

6.4.2 Tracking Error Convergence

Based on Theorem 6.1, we can show the EC of the tracking error in the following theorem:

Theorem 6.2. *Under Assumptions 6.1, 6.2 and condition (6.17), the estimation and control laws (6.12), (6.15), (6.14), (6.16) ultimately ensure that*

$$\lim_{k\to\infty} \|\bar{q}_{i0}(k)\| = 0, \ i = 1, 2. \tag{6.27}$$

Moreover, the convergence rate is exponential.

Proof. By (6.19) and (6.21) we can obtain

$$\bar{q}_{i0}(k+1) = [1 - T\beta s_i(k)]\, \bar{q}_{i0}(k) - T\beta s_i(k)\tilde{q}_{i0}(k), \tag{6.28}$$

where $s_i(k)$ and $u_i(k)$ are given by

$$u_i(k) = -\beta(\bar{q}_{i0}(k) + \tilde{q}_{i0}(k)), \ s_i(k) = s_U(u_i(k)). \tag{6.29}$$

We will show the existence of $\bar{K}(\|\bar{q}_{i0}(0)\|, \|\tilde{q}_{i0}(0)\|)$ such that the dynamics (6.28) is simplified to the following:

$$\bar{q}_{i0}(k+1) = (1 - T\beta)\bar{q}_{i0}(k) - T\beta\tilde{q}_{i0}(k), \ k > \bar{K}. \tag{6.30}$$

Let us denote $D_i(k) = \|\bar{q}_{i0}(k)\|^2$ and consider its rate of change $\Delta D_i(k) = D_i(k+1) - D_i(k)$. Substituting (6.28) to $\Delta D_i(k)$, one has (henceforth we may omit the time argument k and the subscripts where it is inferable from the context):

$$\begin{aligned}\Delta D &= [\bar{q} - T\beta s(\bar{q}+\tilde{q})]'[\bar{q} - T\beta s(\bar{q}+\tilde{q})] - \bar{q}'\bar{q} \\ &\leq T\beta s[-a\|\bar{q}\|^2 + \varepsilon(k)],\end{aligned} \tag{6.31}$$

where $a \triangleq 2 - T\beta$ and $\varepsilon(k) \triangleq T\beta s\|\tilde{q}\|^2 + 2(1+T\beta s)\|\bar{q}\|\|\tilde{q}\|$. By noticing that $\|\bar{q}\|$ increases at most linearly fast while $\|\tilde{q}\|$ is e.c., it can be seen that ε is also e.c. Thus, there exist some positive constants $\eta > 0$ and $\lambda \in (0,1)$ such that $\max\{\|\tilde{q}(k)\|, \varepsilon(k)\} \leq \eta\lambda^k$. Hence we get that $\max\{\|\tilde{q}(k)\|, \varepsilon(k)\} \leq \delta \triangleq \min\{\frac{U}{4\beta}, \frac{aU^2}{(4\beta)^2}\}$ for all $k \geq K^* \triangleq \lceil \ln(\delta/\eta)/\ln(\lambda)\rceil$.

We now seek to show that there exists $\bar{K} \geq K^*$ such that $\|\bar{q}(k)\| \leq \frac{U}{2\beta}$. Indeed, for all $k > K^*$ if $\|\bar{q}(k)\| > \frac{U}{2\beta}$, from (6.31) we have $\Delta D < T\beta s\left(-a\frac{U^2}{(2\beta)^2} + \varepsilon(k)\right) \leq \frac{-3T\beta saU^2}{(4\beta)^2} < 0$ and $\|\bar{q}(k+1)\| < \|\bar{q}(k)\|$, which follows that

$$\|\bar{q}(k)\| < \bar{Q} \triangleq \max\left\{\frac{U}{2\beta}, \|\bar{q}(0)\| + K^*TU\right\}, \ \forall k \geq K^*. \tag{6.32}$$

Thus $s > s^* \triangleq U/\max\{U, \beta(\bar{Q}+\delta)\}$ which leads to $\Delta D < \Delta D^* \triangleq \frac{-3T\beta s^* aU^2}{(4\beta)^2} < 0$. Hence, there exists $\bar{K} < K^* + \left\lceil \frac{1}{|\Delta D^*|}\left[\bar{Q}^2 - \frac{U^2}{(2\beta)^2}\right]\right\rceil$ such that $\left\|\bar{q}(\bar{K})\right\| \leq \frac{U}{2\beta}$. As a result, we have $\beta\left\|\bar{q}(\bar{K}) + \tilde{q}(\bar{K})\right\| \leq \beta\left(\frac{U}{2\beta} + \frac{U}{4\beta}\right) = \frac{3U}{4} < U$, which leads to $s(\bar{K}) = 1$ by (6.29). Substituting this and $\left\|\bar{q}(\bar{K})\right\| \leq \frac{U}{2\beta}$ and $\left\|\tilde{q}(\bar{K})\right\| \leq \frac{U}{2\beta}$ in (6.28), we obtain

$$\begin{aligned}\left\|\bar{q}(\bar{K}+1)\right\| &\leq (1-T\beta)U/(2\beta) + T\beta U/(4\beta) \\ &= U/(2\beta) - TU/4 \leq U/(2\beta).\end{aligned}$$

By induction we conclude that $\|\bar{q}(k)\| \leq \frac{U}{2\beta}$ and $s(k) = 1$ for all $k \geq \bar{K}$. Then the dynamics (6.28) will become (6.30). Since $1 - T\beta < 1$ we can see that $\|\bar{q}(k)\| \leq \bar{Q}\bar{\lambda}^{k-\bar{K}} = \bar{Q}\bar{\lambda}^{-\bar{K}}\bar{\lambda}^k \triangleq \bar{\eta}\bar{\lambda}^k$ for all $k \geq 0$. ■

6.5 Extension

In this section, we discuss the extension of the basic structure by adding new agents with similar leader-following objectives. For each newly added agent, we would design the corresponding estimation and control laws depending on whether it is an orbiter or a follower. An illustration for such extension can be seen in Figure 6.3 in the simulation.

First, consider a new agent j which is an orbiter (e.g. node 4 in Figure 6.3). It can connect to either the leader or a follower i, and the following estimation and control laws can be used to track agent i, using the relative setpoint $q^*_{ji} \triangleq q^*_{j0} - q^*_{i0}$:

$$\begin{cases} \epsilon_{ji}(k) \triangleq \zeta_{ji}(k) - \phi'_{ji}(k)\hat{q}_{ji}(k), & \text{(6.33a)} \\ \hat{q}_{ji}(k+1) = \hat{q}_{ji}(k) + \phi_{ji}(k) + \dfrac{\gamma\phi_{ji}(k)\epsilon_{ji}(k)}{\mu^2_\nu(\gamma\phi_{ji}(k))}, & \text{(6.33b)} \\ \hat{q}_{j0}(k+1) = \hat{q}_{ji}(k+1) + \hat{q}_{i0}(k) + \phi_{i0}(k), & \text{(6.33c)} \\ \bar{u}_j(k) = \pi_U\left(u_j(k)\right) + T^{-1}\Delta\sigma(k) + v(k), & \text{(6.33d)} \\ u_j(k) = -\beta\left(\hat{q}_{ji}(k) - q^*_{ji} - \sigma(k)\right). & \text{(6.33e)} \end{cases}$$

Second, consider a new agent x which is a follower (e.g. agent 5 in Figure 6.3). It will need to connect to an orbiter y and another follower/leader agent z. Similar to Section 6.3.2, we can obtain the following parametric model and scalar observation for the new follower:

$$\zeta_{xz}(k) - \zeta_{xy}(k) = \phi'_{yz}(k)q_{xz}(k) + \phi'_{xy}(k)q_{y0}(k) - \phi'_{xy}(k)q_{z0}(k).$$

The following estimation and control laws are given to the new follower to track agent z, using the relative setpoint $q^*_{xz} \triangleq q^*_{x0} - q^*_{z0}$:

$$\begin{cases} \epsilon_{xz}(k) = \zeta_{xz}(k) - \zeta_{xy}(k) - \phi'_{yz}(k)\hat{q}_{xz}(k) - \phi'_{xy}(k)\hat{q}_{y0}(k) + \phi'_{xy}(k)\hat{q}_{z0}(k), & \text{(6.34a)} \\ \hat{q}_{xz}(k+1) = \hat{q}_{xz}(k) + \phi_{xz}(k) + \dfrac{\gamma\phi_{yz}(k)\epsilon_{xz}(k)}{\mu^2_\nu(\gamma\phi_{yz}(k))}, & \text{(6.34b)} \\ \hat{q}_{x0}(k+1) = \hat{q}_{xz}(k+1) + \hat{q}_{z0}(k) + \phi_{z0}(k), & \text{(6.34c)} \\ \bar{u}_x(k) = \pi_U\left(u_x(k)\right) + v(k), & \text{(6.34d)} \\ u_x(k) = -\beta\left(\hat{q}_{xz}(k) - q^*_{xz}\right). & \text{(6.34e)} \end{cases}$$

Remark 6.10. *Note that extra estimation laws* (6.33c) *and* (6.34c) *have been introduced to estimate the agent's relative position to the leader when it is not connected to the leader. The reason why these laws are necessary can be observed from the perspective of agent 5 in Figure 6.3, which needs to localize itself relative to agent 3 with the aid of agent 4. However, agent 4 does not have any information related to agent 3, hence we need to set a common reference point for all agents, which is the leader.*

Hence, we can keep adding new agent to network using either set of estimation and control laws, depending on the role assigned to it. Similar to the analysis of the basic structure in Section 6.4, we can define the localization and tracking errors of the newly added agents as $\tilde{q}_{ji}(k) \triangleq \hat{q}_{ji}(k) - q_{ji}(k)$, $\bar{q}_{ji}(k) \triangleq \bar{q}_{ji}(k) - q^*_{ij} - \sigma(k)$, $\tilde{q}_{xz}(k) \triangleq \hat{q}_{xz}(k) - q_{xz}(k)$, $\bar{q}_{xz}(k) \triangleq \bar{q}_{xz}(k) - q^*_{xz}$. The following theorem establishes the EC of the localization and estimation error for each added agent under this extension scheme:

Theorem 6.3. *Let Assumptions 6.1, 6.2 and condition* (6.17) *hold, and assume that the agents 0, 1, 2 form a basic structure under the estimation-control laws* (6.12), (6.15), (6.14), (6.16). *Then for any newly added orbiter or follower, the estimation and control laws* (6.12) *ensure that all localization and tracking errors* $\tilde{q}_{ji}(k)$, $\tilde{q}_{j0}(k)$, $\bar{q}_{ji}(k)$, $\tilde{q}_{xz}(k)$, $\tilde{q}_{x0}(k)$, $\tilde{q}_{xz}(k)$ *are e.c.*

Proof. We only consider the case when a new orbiter is added, and the other case of a follower can be shown similarly. Note that the dynamics of localization error $\tilde{q}_{ji}(k)$ for this orbiter will be similar to (6.18). Moreover, $\phi_{ji}(k) = T\pi_U(u_j(k)) + \Delta\sigma(k) - T\pi_U(u_i(k))$, where $\pi_U(u_i(k)) = \pi_U(-\beta\bar{q}_i(k) - \beta\tilde{q}_i(k))$ converges to 0 exponentially fast since both localization and tracking errors of agent i are e.c. Thus, there exists K_{ji} such that $\sqrt{m}T(U + \pi_U(u_i(k))) \leq \rho$ for all $k \geq K_{ij}$ and $\phi_{ji}(k)$ is p.e., and $\tilde{q}_{ji}(k)$ becomes e.c.

Note that from (6.33c) we have $\tilde{q}_{j0}(k+1) = \tilde{q}_{ji}(k+1) + \tilde{q}_{i0}(k)$. Since $\tilde{q}_{ji}(k)$ and $\tilde{q}_{i0}(k)$ are e.c., $\tilde{q}_{j0}(k)$ is also e.c., which induces the e.c. localization error of other agents added later.

Also, from (6.33d) and (6.33e) we obtain the following tracking error dynamics:

$$\bar{q}_{ji}(k+1) = [1 - T\beta s_j(k)]\,\bar{q}_{ji}(k) - T\beta s_j(k)\tilde{q}_{ji}(k) + T\bar{v}_i(k),$$

where $\bar{v}_i(k) = -\pi_U(u_i(k))$ and $s_j(k) = s_U(u_j(k))$. Since $\bar{v}_i(k)$ is e.c., so is $\tilde{q}_{ji}(k)$, thus the dynamics of $\bar{q}_{ji}(k+1)$ evolves similarly to (6.28). Hence we can repeat the same procedure in the proof of Theorem 6.2 to establish the EC of $\bar{q}_{ji}(k)$. ■

6.6 Simulation

In this section we will verify the theoretical findings by numerical simulation for a network of six agents as shown in Figure 6.3. Here we focus on a simple 2D scenario. However, the algorithm can also be applied in the 3D case by choosing a p.e. trajectory $\sigma(k)$ as in Chapter 4.

The values of the parameters are taken as follows:

$$
\begin{aligned}
&T = 0.096,\ U = 0.25,\ \gamma = 2,\ \nu = 1.5743,\ \beta = 2.5;\\
&\hat{q}_{i,j}(0) = [0, 0]',\ \forall i, j \in \{0, 1, 2, 3, 4, 5\};\\
&p_0(0) = [10,\ 0]',\ p_1(0) = [6,\ 2]',\ p_2(0) = [1,\ 4]';\\
&p_3(0) = [3,\ 8]',\ p_4(0) = [6,\ 8]',\ p_5(0) = [3,\ 2]';\\
&q^*_{10} = [-2,\ -2]',\ q^*_{20} = [-2,\ 2],\ q^*_{30} = [-4,\ 0]';\\
&q^*_{40} = [-6,\ 2]',\ q^*_{50} = [-6,\ -2]';\\
&\sigma(k) = [\sin(k\pi/48),\ -0.75\sin(k\pi/24)]';\\
&v(k) = \bar{u}_0(k) = f(k+1) - f(k),\\
&f(k) = [x(k), 9e^{-0.5x(k)}\sin(0.75x(k)) + 1.25x(k)]',\\
&x(k) = k \times 8/202.752.
\end{aligned}
$$

The simulation spans from $k = 0$ to $k = 2112$. After computing and comparing all matrices $W \in \mathcal{W}$, we can find that $\rho = \max_{W\in\mathcal{W}}(g(W)) \approx 0.083916$ and $\sqrt{2}TU \approx 0.033941$, thus condition (6.17c) is satisfied. Moreover, as $T\beta \approx 0.25 < 1$, by Theorems 6.1 and 6.2, both localization and tracking errors converge to zero exponentially fast, which is indeed reflected in Figure 6.2.

The trajectories of all agents are shown in Figure 6.3. As we can see, all the followers are initially far away from the leader, but as time progresses, they are able to track the leader and finally approach the desired relative setpoints q^*_{i0}. The orbiters can also track the leader while executing the p.e. motion, as shown by the green lines.

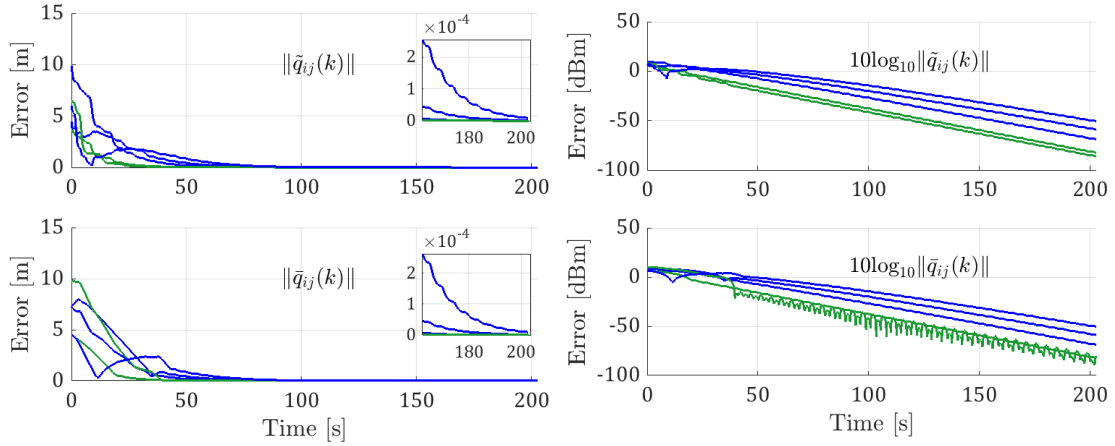

(a) Linear scale.

(b) Logarithmic scale.

FIGURE 6.2: Localization error and tracking error of the agents in linear and logarithmic scales. The subscript ij takes value from 10, 20, 32, 42, 53. We use the green color to distinguish the localization and tracking errors of the two orbiters from those of the followers. As seen in the zoomed-in plots and the logarithmic plots, we can confirm that all errors converge to zero exponentially fast.

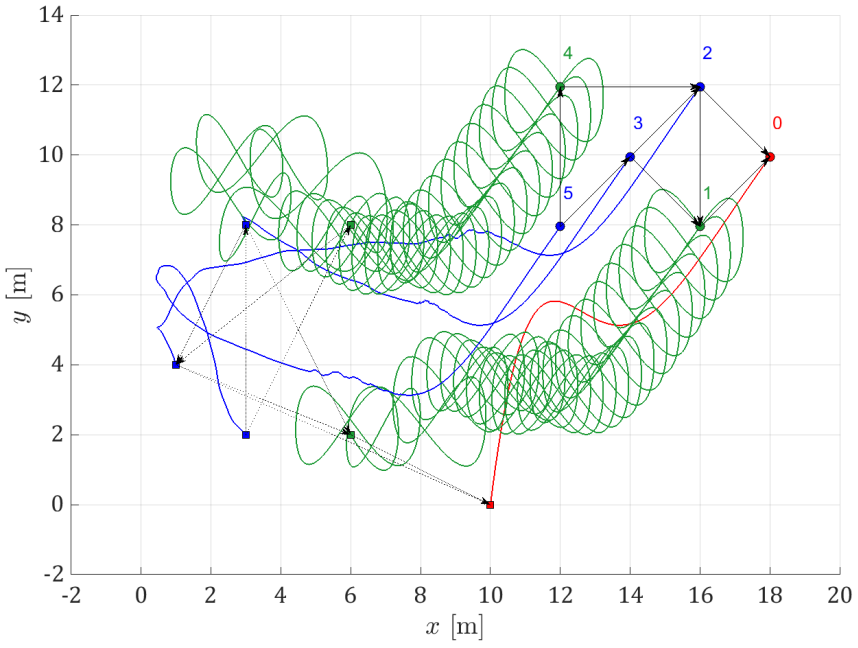

FIGURE 6.3: A network of 6 agents with one leader (red), two orbiters (green), three followers (blue) and their trajectories. The direction of the arrows is interpreted similarly as in Figure 6.1. The square markers indicate the initial positions, and the round ones are for the final positions in simulation.

6.7 Experiment

In this section we implement our algorithm in real world condition to further validate the theoretical results. Video recording of the flight tests can be viewed at: https://youtu.be/df25A4jRDO8. Three MAVs are employed to form a basic structure in this case. A set of high accuracy commercial UWB ranging sensors[1] are employed to provide both distance measurements and the communication network. To obtain the displacement measurements, data from inexpensive commercial optical flow sensors [63] are fused with IMU and magnetometer data by using the PX4 flight stack. The displacement information is also sent to the neighbour agents along with the UWB messages.

Note that before communication, the optical flow measurements are to be calibrated to the corresponding local inertial frame (for convenience we initialize the MAVs with the same orientation for all the inertial frames, otherwise we can use the absolute orientation in reference to the earth's magnetic field).

The algorithm is implemented on ROS. All the parameters in the estimation and control laws, as well as the PE trajectory, are the same as in the simulation. The relative position setpoints are chosen as $q_{10}^* = [1, -2.5]'$ and $q_{20}^* = [0.25, 2]'$, which are also used in the deployment and the initialization of the relative position estimates. This accurate initialization is to avoid the unpredictable behavior by MAVs, e.g. flying outside of the testing area or colliding with each other.

The orbiter and the follower are controlled to take off manually and then switch to the autonomous mode when the velocity control command $\bar{u}_i(k)$ is executed to maintain the relative position with the leader. For safety, the leader is manually controlled, and its velocity is broadcast to all agents. An overhead Vicon[2] motion capture system is used to record the trajectories of the agents for ground truth. These data are only recorded for offline analysis and not used in the flight test.

A total of 5 flight tests have been conducted. To quantify the performance of the relative localization scheme, we compare the onboard estimates calculated in each flight test with ground truth from Vicon, then calculate the root mean square (RMS) and standard deviation (SD) of the estimation error in all flight tests (see T1 columns in Table 6.1 and Table 6.2).

[1] http://www.timedomain.com/products/pulson-440/
[2] https://www.vicon.com

TABLE 6.1: RMS and SD values of the relative localization error of the orbiter from onboard and offboard estimation processes (unit: m).

Exp.	$\text{rms}(\tilde{q}_{10,x})$			$\text{rms}(\tilde{q}_{10,y})$			$\text{sd}(\tilde{q}_{10,x})$			$\text{sd}(\tilde{q}_{10,y})$		
	T1	T2	T3	T1	T2	T3	T1	T2	T3	T1	T2	T3
1	.259	.123	.212	.816	.535	.592	.255	.123	.201	.386	.175	.280
2	.325	.128	.347	.671	.353	.622	.325	.097	.347	.393	.121	.397
3	.259	.123	.553	.816	.535	.656	.255	.123	.457	.386	.175	.365
4	.803	.115	.590	.940	.523	.944	.676	.112	.564	.380	.208	.492
5	.803	.154	.770	.227	.280	.250	.333	.094	.323	.223	.131	.226

TABLE 6.2: RMS and SD values of the relative localization error of the follower from onboard and offboard estimation processes (unit: m).

Exp.	$\text{rms}(\tilde{q}_{20,x})$			$\text{rms}(\tilde{q}_{20,y})$			$\text{sd}(\tilde{q}_{20,x})$			$\text{sd}(\tilde{q}_{20,y})$		
	T1	T2	T3	T1	T2	T3	T1	T2	T3	T1	T2	T3
1	.183	.106	.189	.800	.302	.689	.178	.045	.181	.428	.194	.351
2	.488	.255	1.047	.388	.198	.527	.475	.148	.990	.275	.152	.399
3	.183	.106	.312	.800	.302	.338	.178	.045	.275	.428	.194	.202
4	.422	.400	.636	1.102	.173	1.233	.403	.212	.600	.712	.120	.967
5	.238	.221	.239	.513	.111	.386	.221	.130	.207	.324	.111	.310

At the first look, we found that the localization error is typically around 1 m in either direction. After examining the data, we suppose that this error could be attributed to the measurement errors. To verify this reasoning, we collected data from the Vicon motion capture system (millimeter accuracy) and carried out an "offboard" rerun of the estimation algorithm with *Vicon-derived displacement* and the original UWB distance measurements. The RMS and SD of the estimation error are reported under the T2 columns in Table 6.1 and Table 6.2. Indeed, it can be seen that almost all RMS and SD values on the offboard estimation error show significant improvement (except a slight increase in the RMS and SD values of $\tilde{q}_{20}(k)$ in dataset 3, which is due to the temporary corruption of Vicon data when the MAV flew over the boundary of the testing area). Moreover, as shown in Figure 6.4, with better displacement measurements, the offboard relative position estimates are quite close to the true value.

Furthermore, we conducted a similar offboard rerun with the *Vicon-derived distance* and the original displacement measurements and reported the RMS and SD values of the estimation errors under T3 columns in Table 6.1 and Table 6.2. It can be seen that no significant improvement is shown in this offboard estimation process. This

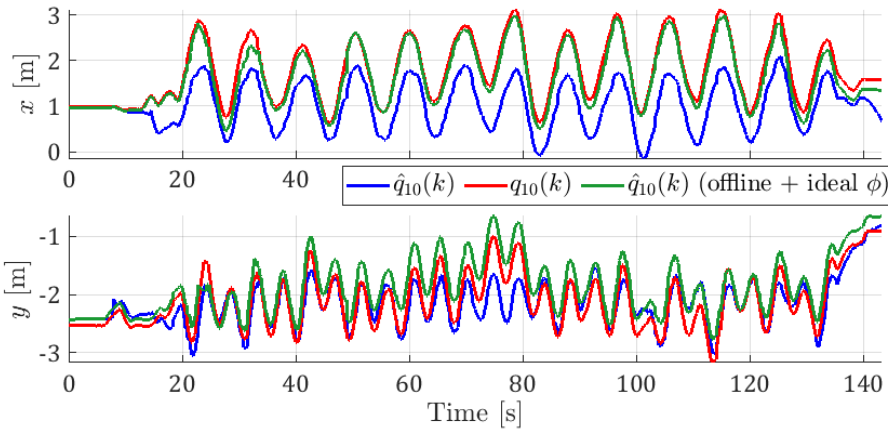

(a) Relative position estimates and the ground truth of the orbiter.

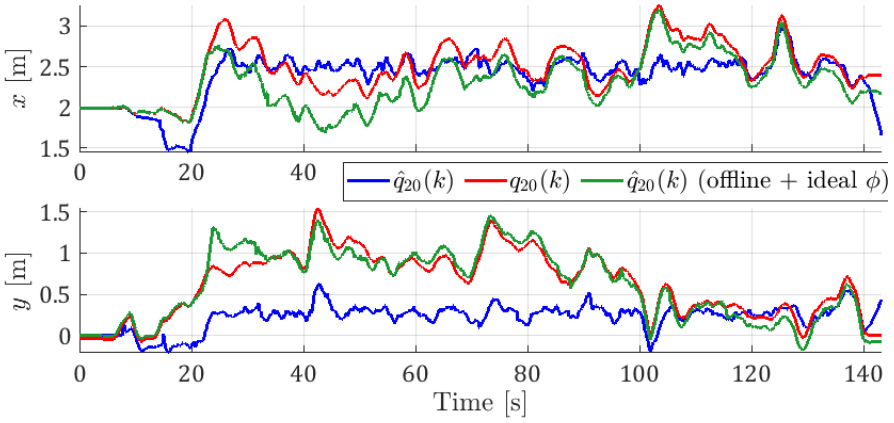

(b) Relative position estimates and the ground truth of the follower.

FIGURE 6.4: Time evolution of the onboard and offboard relative position estimates of the orbiter and the follower compared with ground truth.

can be attributed to the fact the UWB ranging sensor is already quite accurate, and not much improvement can be gained from better ranging accuracy.

Therefore, we infer that the quality of the displacement measurements plays a major role in deciding the accuracy of the relative localization scheme. For improvement in the future, better visual odometry methods should be used instead of the current optical flow sensor, which is prone to error and the lack of features on the ground. Nevertheless, in all flight tests, we find that the orbiter and follower are able to track the leader with the orbiter performing the predefined trajectory around the setpoint, demonstrating the efficacy of the relative localization and leader-following control scheme in GPS-less environments. Figure 6.5 shows some snapshots of our flight tests in indoor and outdoor conditions.

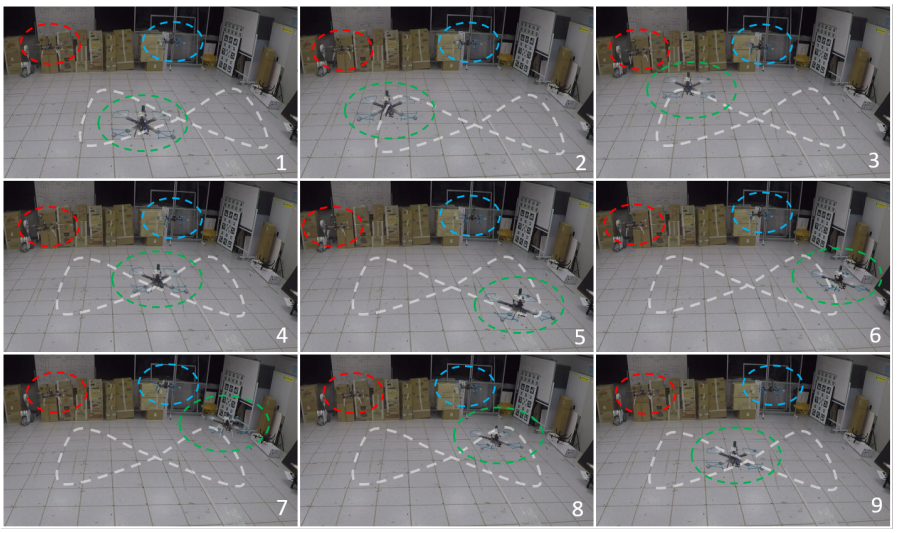

(a) Indoor flight.

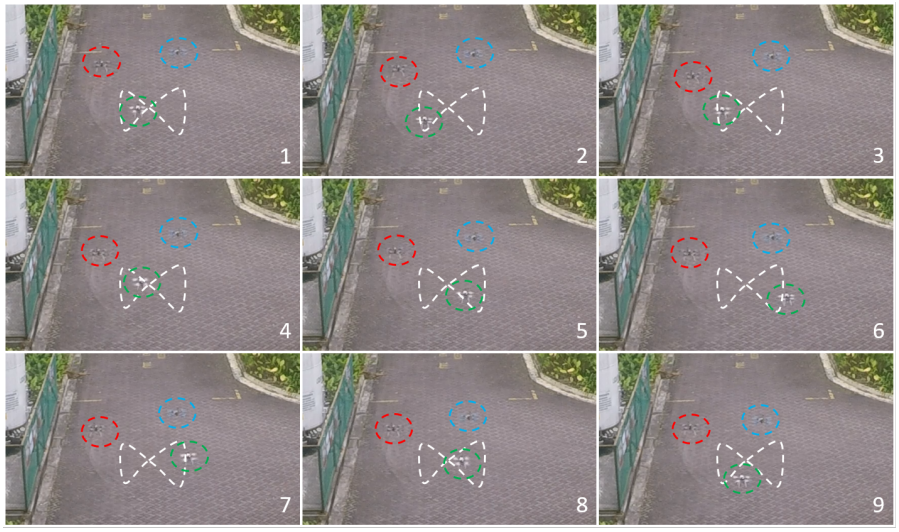

(b) Outdoor flight.

FIGURE 6.5: Snapshots of flight tests on real quadcopters. The leader is marked by the red circle, the orbiter by the green circle and the follower by the blue circle. The p.e. trajectory is visualized by the white curve. Video recording of these tests can be viewed at https://youtu.be/df25A4jRD08.

6.8 Conclusion

In this chapter we have proposed a cooperative scheme to achieve simultaneous relative localization and tracking control for a group of leader-following MAVs. Our method only requires distance and displacement measurements from onboard sensors and basic communication capability between the MAVs. Rigorous analysis has been conducted to establish the parametric conditions for the convergence of the localization and tracking errors. The theoretical findings were verified by

simulation results, and successful implementation has demonstrated the efficacy of the proposed scheme.

Chapter 7

Persistently-Excited Adaptive Relative Localization and Time-Varying Formation of MAV Swarms

7.1 Introduction

In the previous chapter, we have integrated the distance-displacement based relative localization technique into a cooperative relative localization and leader-following scheme. As we only focused on tracking task, the proposed control laws only employ the relative position estimate from a single neighbour. However, in a more general cooperative scheme, agents could have multiple neighbours, thus, the relative localization and control laws should be extended to incorporate the information from all of these neighbours, where the key issue here is still how to ensure the PE condition on the relative displacement measurement, so that the relative position estimation error with each neighbour can still converge to zero. In the previous chapter we have employed a scheme with specialized orbiter agents for this purpose. In practice one would like to minimize the number of orbiters, as they tend to consume more energy in tracking a p.e. trajectory and possibly communicating with multiple followers. In this chapter, we will investigate a different approach where the requirement of maintaining the PE condition will be distributed to all

agents. Specifically, we will study the integration of the distance-displacement-based method into a formation paradigm called *time-varying formation*. In this paradigm, as the formation is defined by time-varying trajectories, we can design these trajectories so that the relative displacement between the agents satisfy the PE condition and still achieve relative localization with EC, which induces the EC of the formation error. Hence, we refer to this approach PEARL-TVF (*Persistently Excited Adaptive Relative Localization and Time-Varying Formation*).

Besides generalizing the topology, in the previous chapter, we have also assumed that the leader's velocity is known to all agents. While this can be achieved by some broadcast-based communincation techniques, or predefined trajectory running in the software program of all agents [17], in practice some discrepancy or unexpected control input by the leader may arise. Thus, in this chapter, we also formulate this as an unpredictable input of the leader and show that the time-varying formation can be achieved with an ultimately bounded error that closely matches the predicted bound thanks to the use of directed acyclic topology (which can be obtained from some hierarchical decomposition scheme [127]).

The contributions of this chapter are threefold. First, we propose an effective and efficient integration scheme for relative localization and time-varying formation, where the time-varying formation objective and the relative localization objective are inherently reinforcing each other. Second, we consider discrete-time dynamics with bounded inputs, which maximizes the compatibility of the proposed scheme with practical implementation. Specifically, the discrete-time formulation waives the requirement of the derivative of distance measurements in previous works [111], which is difficult to obtain in practice. Finally, we also study the steady-state formation error bound for a leader with nondeterministic input (unmodeled dynamics), and provide an explicit error bound which is dependent on the network topology, the input bound, and the control gain. Note that the nondeterministic input is unpredictable and can be seen as a bounded unknown disturbance, and the coordination problem under input saturation and external disturbance is rarely investigated in the literature, except a few papers [128, 129] which studied output regulation with a known disturbance dynamic model. Different from the above works which employed small gain approach to avoid saturation and can only achieve semi-global stability, we address the saturation in the analysis which saves

the trouble of gain tuning and achieves global stability. Also, it is worth mentioning that the predicted error bound matches closely with the simulation result.

This chapter is organized as follows: after providing the basic definitions and the problem formulation in Section 7.2, we present the localization and control laws in Section 7.3. The convergence results and analyses are then provided in Section 7.4. Numerical simulations and physical implementations are conducted in Section 7.5 to validate the theoretical findings. We conclude this chapter in Section 7.6.

7.2 Preliminaries and Problem Formulation

In this section we shall put forth some basic definitions before formulating the problem under consideration.

7.2.1 Topology

For a leader-follower network of $n+1$ agents, let us describe the sensing and communication within the network by a directed graph $G = \{\bar{V}, \bar{E}\}$. Specifically, $\bar{V} = \{0, 1, 2 \dots n\}$ is the node set, $\bar{E} = \{(i,j) \colon i, j \in \bar{V}, i \neq j\}$ is the edge set where $(i,j) \in \bar{E}$ if agent i can obtain measurements from agent j. $N_i = \{j : (i,j) \in \bar{E}\}$ is the neighbour set of agent i. We assign agent 0 as a leader which has no neighbours, and denote the set of followers by $V = \bar{V} \backslash \{0\}$. A path from node i_1 to node i_l is defined as $(i_1, i_2, \dots, i_l)$ where $(i(k), i(k+1)) \in \bar{E}$ for $k = 1, \dots, l-1$, and it is a cycle if $i_1 = i_l$. G is called a *directed acyclic graph* (DAG) if it has no cycle. The leader 0 is said to be globally reachable if there exists a path from any other node to 0. We use $a_{ij} \geq 0$ to model the connection weight between two agents i and j, and $a_{ij} > 0$ iff $(i,j) \in \bar{E}$. In this work, we adopt the following standard assumption for a leader-follower multi-agent system:

Assumption 7.1. *The leader 0 is globally reachable, and* $\sum_j a_{ij} = 1$ *for any* $i \in V$.

7.2.2 Agent Dynamics and Measurements

Assume that the agents' positions in some common frame of reference F_E are modeled by the following discrete-time dynamics with bounded velocity:

$$\begin{cases} p_0(k+1) = p_0(k) + T\bar{u}_0(k) + Tv_0(k); \\ p_i(k+1) = p_i(k) + T\bar{u}_i(k),\ \forall i \in V; \\ \|\bar{u}_i(k)\| \leq \bar{U}_i,\ \forall i \in \bar{V}, \|v_0(k)\| \leq U_0; \end{cases} \tag{7.1}$$

where $p_i(k) \in \mathbb{R}^m$ denotes the position of agent i at time kT, T is the sampling period, and U_0, $\bar{U}_i > 0$ are some user-defined maximum velocities. Note that the leader's input consists of two terms: $\bar{u}_0(k)$ denotes a predetermined input to track a reference trajectory; $v_0(k)$ denotes a situational input generated in real-time to address the environmental change, e.g. obstacle avoidance, which is unpredictable and not available to followers. Accordingly, we refer to the leader as a *deterministic leader* if $v_0(k) \equiv 0$, and *nondeterministic leader* if $v_0(k) \not\equiv 0$.

At time step k, we assume that agent i can measure the self-displacement $\phi_i(k+1)$, the distance $d_{ij}(k)$ to its neighbour j, and receive $\phi_j(k+1)$ sent from the neighbour j to calculate relative displacement $\phi_{ij}(k+1)$. These quantities are formally defined as follows:

$$\begin{cases} d_{ij}(k) = \|p_i(k) - p_j(k)\|, & \text{(7.2a)} \\ \phi_i(k) = p_i(k+1) - p_i(k), & \text{(7.2b)} \\ \phi_{ij}(k) = \phi_i(k) - \phi_j(k), j \in N_i. & \text{(7.2c)} \end{cases}$$

7.2.3 Problems

Relative Localization: At time kT, denote the relative position between agents i and j as

$$q_{ij}(k) = p_i(k) - p_j(k). \tag{7.3}$$

Moreover, denote $\hat{q}_{ij}(k)$ as an estimate of $q_{ij}(k)$, and $\tilde{q}_{ij} \triangleq \hat{q}_{ij}(k) - q_{ij}(k)$ as the *relative localization error*. Based on the measurements in (7.2), we aim to design an estimator for $\hat{q}_{ij}$ to achieve the following convergence:

$$\lim_{k\to\infty} \|\tilde{q}_{ij}(k)\| = 0,\ \forall (i,j) \in \bar{E}. \tag{7.4}$$

Time-Varying Formation: Let us assign each agent $i \in \bar{V}$ a reference trajectory $\Sigma_i = \{\sigma_i(k)\}_{k=0}^{\infty}$ and define the formation error as follows:

$$\bar{q}_i(k) \triangleq \bar{p}_i(k) - \bar{p}_0(k), \ \bar{p}_i(k) \triangleq p_i(k) - \sigma_i(k). \tag{7.5}$$

The time-varying formation is achieved if the following convergence is achieved for any $i \in V$:

$$\limsup_{k\to\infty} \|\bar{q}_i(k)\| = \begin{cases} 0, & v_0(k) \equiv 0, \quad (7.6a) \\ Q_i(G, U_0) \in \mathbb{R}^+, & v_0(k) \not\equiv 0, \quad (7.6b) \end{cases}$$

where Q_i is a positive constant depending on the network topology and the upper bound U_0 of $\|v_0(k)\|$.

To efficiently solve the relative localization and time-varying formation problems, we consider a case when the formation setpoints $\sigma_i(k)$ between neighbouring agents satisfy the following PE condition:

Assumption 7.2. *For any $(i,j) \in \bar{E}$, there exist $\gamma_{ij,2} \geq \gamma_{ij,1} > 0$ and $K_{ij}, n_{ij} \in \mathbb{N}$ such that $\forall l \geq n_{ij}$, there exists $\kappa_{ij}(l) \subseteq \{l, l+1, \ldots, l+K_{ij}-1\}$ satisfying*

$$\gamma_{ij,1} I \leq \sum_{k\in\kappa_{ij}(l)} \Delta\sigma_{ij}(k)\Delta\sigma'_{ij}(k) \leq \gamma_{ij,2} I, \tag{7.7}$$

where $\Delta\sigma_{ij}(k) = [\sigma_i(k+1) - \sigma_i(k)] - [\sigma_j(k+1) - \sigma_j(k)]$.

Remark 7.1. *The characterization of the PE condition in Assumption 7.2 is slightly more general than in Chapter 6. Essentially, we require that for every K_{ij} consecutive steps, there exist some steps where the relative reference velocity $\Delta\sigma_{ij}(k)$ satisfies condition (7.7), i.e. "persistently spans $\mathbb{R}^m$". This condition can be satisfied straightforwardly, but not necessarily, by selecting appropriate periodic relative time-varying trajectories $\sigma_{ij}(k)$ with K_{ij} as the period of $\Delta\sigma_{ij}(k)$, which was the approach used in the previous chapter. In time-varying formation, such periodic motions occur in several scenarios where the agents move in a loop for surveillance and patrol, as well as target capture [130, 131]. Furthermore, other than pre-defined periodic motions, the PE steps can be negotiated ahead online by neighbouring agents.*

7.3 Integrated Estimation-Control Laws

In this part, we propose the distributed estimation and control laws to solve the relative localization and time-varying formation problems by employing adaptive control techniques.

7.3.1 Relative Localization Estimator

For each agent $i \in V$ and $j \in N_i$, it can be checked that $\zeta_{ij}(k) \triangleq \frac{1}{2}[d_{ij}^2(k+1) - d_{ij}^2(k) - \|\phi_{ij}(k)\|^2] = \phi_{ij}'(k)q_{ij}(k)$. Thus, we employ a relative localization method similar to (5.10) in Chapter 5 to estimate the relative position $q_{ij}(k)$ as follows:

$$\begin{cases} \epsilon_{ij}(k) = \zeta_{ij}(k) - \phi_{ij}'(k)\hat{q}_{ij}(k) = -\phi_{ij}'(k)\tilde{q}_{ij}(k), & \text{(7.8a)} \\ \Gamma_{ij}(k+1) = \dfrac{1}{\beta_f}\left[\Gamma_{ij}(k) - \dfrac{\Gamma_{ij}(k)\phi_{ij}(k)\phi_{ij}'(k)\Gamma_{ij}(k)}{\beta_f + \phi_{ij}'(k)\Gamma_{ij}(k)\phi_{ij}(k)}\right], & \text{(7.8b)} \\ \hat{q}_{ij}(k+1) = \hat{q}_{ij}(k) + \phi_{ij}(k) + \Gamma_{ij}(k+1)\phi_{ij}(k)\epsilon_{ij}(k), & \text{(7.8c)} \end{cases}$$

where $\Gamma_{ij}(k) \in \mathbb{R}^{m\times m}$ with $\Gamma_{ij}(0) > 0$, and $\beta_f \in (0,1)$ is a forgetting factor.

7.3.2 Formation Controller

Based on the relative position estimate $\hat{q}_{ij}(k)$ and $\sigma_j(k)$ communicated from $j \in N_i$, the distributed control law $\bar{u}_i(k)$ is designed as follows:

$$\bar{u}_i(k) = \pi_{U_i}\left(u_i(k)\right) + T^{-1}\Delta\sigma_i(k),\ U_i \in (0, \bar{U}_i); \tag{7.9}$$

$$u_i(k) = -\beta\textstyle\sum_j a_{ij}\left(\hat{q}_{ij}(k) - \sigma_{ij}(k)\right);\ \beta < 1/T, \tag{7.10}$$

$$\Delta\sigma_i(k) = \sigma_i(k+1) - \sigma_i(k),\ \sigma_{ij}(k) = \sigma_i(k) - \sigma_j(k),\ \forall\ i,j \in \bar{V}. \tag{7.11}$$

Note that $u_0(k) \equiv 0$ as $N_0 = \emptyset$.

Remark 7.2. *Note that the notion of the global frame F_E is only introduced for convenience in formulation. From (7.9) and (7.10), we see that the control $\bar{u}_i(k)$ only consists of $\Delta\sigma_i(k)$, which is a differentiation, and $u_i(k)$, which only involves relative terms. Thus if one changes the global frame F_E to another arbitrary frame $F_{E'}$, all relative position estimates and control inputs will remain the same, i.e the system is invariant to the choice of reference frame.*

7.4 Convergence Analysis

7.4.1 Convergence of Relative Localization Error

Under Assumption 7.2, select small T to satisfy that

$$T\sqrt{\mathcal{K}_{ij}}(U_i + U_j) < \gamma_{ij,1},\ \forall (i,j) \in \bar{E}, \tag{7.12}$$

where $\mathcal{K}_{ij} = \max_{l \geq n_{ij}}\{\kappa_{ij}(l)\} \leq K_{ij}$. We can show the EC of the relative position estimate on each edge in the following theorem.

Theorem 7.1. *Under Assumption 7.2 and the condition (7.12), given $(i,j) \in \bar{E}$, the relative displacement $\phi_{ij}(k)$ satisfies the following PE condition for any $l \geq n_{ij}$:*

$$\rho_{ij,1} I \leq \sum_{k \in \kappa_{ij}} \phi_{ij}(k)\phi_{ij}'(k) \leq \rho_{ij,2} I, \tag{7.13}$$

where $\rho_{ij,1} = [\gamma_{ij,1} - T\sqrt{\mathcal{K}_{ij}}(U_i + U_j)]^2$ and $\rho_{ij,2} = [\gamma_{ij,2} + T\sqrt{\mathcal{K}_{ij}}(U_i + U_j)]^2$. As a result, the estimation error $\tilde{q}_{ij}(k)$ converges to 0 exponentially fast under the estimation law (7.8).

Proof. Given $(i,j) \in \bar{E}$, denote $v_{ij}(k) = \pi_{U_i}(u_i(k)) - \pi_{U_j}(u_j(k)) - v_j(k)$, where $v_j(k) = 0$ if $j \neq 0$. We can see from (7.2b), (7.2c) and (7.10) that

$$\phi_{ij}(k) = \Delta\sigma_{ij}(k) + T v_{ij}(k). \tag{7.14}$$

To show (7.13), it is equivalent to show that for any unit vector x, it holds that $x'Sx \in [\rho_{ij,1}, \rho_{ij,2}]$ with $S = \sum_{k \in \kappa_{ij}} \phi_{ij}(k)\phi_{ij}'(k)$. Denote

$$W = [\Delta\sigma_{ij}(k_1), \Delta\sigma_{ij}(k_2), \ldots, \Delta\sigma_{ij}(k_{|\kappa_{ij}|})],$$
$$V = [v_{ij}(k_1), v_{ij}(k_2), \ldots, v_{ij}(k_{|\kappa_{ij}|})];\ k_1, k_2, \cdots \in \kappa_{ij}.$$

Direct computation shows that

$$x'Sx = \|W'x\|^2 + 2T\langle W'x, V'x\rangle + T^2\|V'x\|^2.$$

Let $w = \|W'x\|$ and $v = \|V'x\|$. Since $-wv \leq \langle W'x, V'x\rangle \leq wv$ by Cauchy-Schwartz inequality, we have $x'Sx \in [(w - Tv)^2, (w + Tv)^2]$. Note that $v \leq$

$\sqrt{|\kappa_{ij}|}(U_i + U_j)$ as a result of $\|v_{ij}(k)\| \leq U_i + U_j$, and the condition (7.7) implies that $w \in [\gamma_{ij,1}, \gamma_{ij,2}]$. Therefore, it holds under the condition (7.12) that $x'Sx \in [\gamma_{ij,1}^2, \gamma_{ij,2}^2]$, which is equivalent to (7.13).

The relative position evolves by $q_{ij}(k+1) = q_{ij}(k) + \phi_{ij}(k)$. Combining this with (7.8c) and (7.8a), the localization error $\tilde{q}_{ij}(k) \triangleq \hat{q}_{ij}(k) - q_{ij}(k)$ is dictated by $\tilde{q}_{ij}(k+1) = \left[I - \Gamma_{ij}(k)\phi_{ij}(k)\phi_{ij}'(k)\right]\tilde{q}_{ij}(k)$. With the PE condition on $\phi_{ij}(k)$, the EC of this system can be proved along the same line as in Theorem 1 of [125]. ■

7.4.2 Convergence of Time-Varying Formation Error

Based on the convergence of $\hat{q}_{i,j}(k)$ in the last section, here we will solve the time-varying formation problem respectively for a deterministic leader and a nondeterministic leader, by examining the formation error for each follower i. To this end, we first rewrite $u_i(k)$ in (7.10) as

$$u_i(k) = -\beta \sum_j a_{ij}(\bar{q}_i(k) - \bar{q}_j(k) + \tilde{q}_{ij}(k)), \tag{7.15}$$

where we used the equations $\hat{q}_{ij} = q_{ij} + \tilde{q}_{ij}$ and $q_{ij} - \sigma_{ij} = \bar{p}_i - \bar{p}_j = \bar{q}_i - \bar{q}_j$ from (7.3) and (7.5). Then the dynamics of the formation error can be found as

$$\begin{aligned} \bar{q}_i(k+1) &= \bar{q}_i(k) + \pi_{U_i}\left(u_i(k)\right) - Tv_0(k) \\ &= \bar{q}_i(k) - T\beta s_i(k)\sum_j a_{ij}(\bar{q}_i(k) - \bar{q}_j(k)) - \varepsilon_i(k) - Tv_0(k), \end{aligned} \tag{7.16}$$

where $s_i(k) = s_{U_i}(u_i(k))$ and $\varepsilon_i(k) = T\beta s_i(k)\sum_j a_{ij}\tilde{q}_{ij}(k)$.

Let us put forth the following condition and some extra definitions to be used in the next theorems on convergence of the formation error:

$$0 < T(U_i + U_0)^2 / \left[2(U_i - U_0)\right] < U_i/\beta, \ \forall i \in V. \tag{7.17}$$

Moreover, define $C = [c_{ij}] \in \mathbb{R}^{n\times n}$ and $\hat{C} = C^{-1} = [\hat{c}_{ij}]$ by

$$c_{ij} = \begin{cases} 1, & i = j \in V, \\ -a_{ij}, & i \neq j \in V. \end{cases} \tag{7.18}$$

Note that C is invertible under Assumption 7.1 (Lemma 2.1, [132]). Now the convergence of formation error can be stated in the following theorem:

Theorem 7.2. *Let Assumptions 7.1 and 7.2 hold, and select T by the condition (7.12). If $v_0(k) \equiv 0$, then the time-varying formation problem (7.6a) is solved with EC under the estimator (7.8) and the controller (7.10).*

Proof. With $v_0(k) \equiv 0$, we can simplify (7.16) as

$$\bar{q}_i(k+1) = \alpha_i(k)\bar{q}_i(k) + \sum_{j\neq 0} \alpha_{ij}(k)\bar{q}_j(k) - \varepsilon_i(k), \tag{7.19}$$

where $\alpha_{ij}(k) = T\beta s_i(k)a_{ij}$, and $\alpha_i(k) = 1 - \sum_j \alpha_{ij}(k) = 1 - T\beta s_i(k)$. Note that the summation in (7.19) excludes the leader as $\bar{q}_0(k) \equiv 0$ by definition, and hence

$$c_i(k) \triangleq \alpha_i(k) + \sum_{j\neq 0} \alpha_{ij}(k) = 1 - \alpha_{i0}(k) \leq 1. \tag{7.20}$$

Accordingly, we can define a matrix $A(k) \in \mathbb{R}^{n\times n}$ whose (i,i)-th entry is given by $\alpha_i(k)$, and the non-diagonal (i,j)-th entry is given by $\alpha_{ij}(k)$. Clearly, $A(k)$ is a nonnegative matrix with each row sum $c_i(k) \leq 1$. Now we can establish the EC of $\bar{q}_i$ after showing its boundedness.

1) Boundedness of $\bar{q}_i$: $\varepsilon_i(k)$ is e.c. as a result of Theorem 7.1 and $s_i(k) \in (0,1]$. Thus, there exist $e > 0$ and $\lambda \in (0,1)$ such that $\|\varepsilon_i(k)\| \leq e\lambda^k$ for all $i \in V$. Denote $b(k) = [\|\bar{q}_1(k)\|, \ldots, \|\bar{q}_n(k)\|]'$. By applying the triangle inequality to (7.19) for each i we get the following componentwise inequality

$$b(k+1) \leq A(k)b(k) + \mathbf{1}e\lambda^k, \tag{7.21}$$

where $\mathbf{1} \in \mathbb{R}^n$ is a vector of ones. Noticing that $A(k)\mathbf{1} \leq \mathbf{1}$, it is clear that

$$b(k) \leq b(0) + \mathbf{1}e\sum_{l=0}^{k+1} \lambda^l \leq b(0) + \mathbf{1}\frac{e}{1-\lambda},$$

which is the required boundedness.

2) EC of $\bar{q}_i$: By the boundedness we can immediately get from (7.15) that u_i is bounded, and there exists $s_* \in (0,\ 1)$ so that $s_i(k) \geq s_*$. Consequently, we have $T\beta s_* a_{ij} \leq \alpha_{ij}(k) \leq T\beta a_{ij}$. Below we will show the convergence based on (7.21).

For each follower i, let the shortest path from i to the leader be of length l_i. Accordingly, we can classify the followers into different groups S_l, so that $l_i = l$ for $i \in S_l$. Assume that $l \leq L$ and denote $Q(k) = \max_i \|\bar{q}_i(k)\|$. We shall show that for any $i \in S_l, l = 1, \ldots, L$, there exists $\eta_{i,l} \in (0,1)$ such that

$$\|\bar{q}_i(k+d)\| \leq \eta_{i,l} Q(k) + e \sum_{t=k}^{k+d-1} \lambda^t,\ d \in [l, L]. \tag{7.22}$$

Thus, by letting $\eta = \min_{i,l} \eta_{i,l} \in (0,1)$ we can obtain

$$Q(k+L) \leq \eta Q(k) + e \sum_{t=k}^{k+L-1} \lambda^t, \tag{7.23}$$

which implies the EC of $\bar{q}_i$.

To show (7.22), we first note that (7.21) implies that

$$b(k+d) \leq A(k+d-1:k)b(k) + \mathbf{1}e \sum_{t=k}^{k+d-1} \lambda^t, \tag{7.24}$$

where $A(k+d-1:k)$ is recursively defined as $A(k_2:k_1) = A(k_2)A(k_2-1:k_1)$ if $k_2 \geq k_1$, otherwise $A(k_2:k_1) = I$. Denote $A_i(k+d-1:k)$ as the i-th row of $A(k+d-1:k)$. Comparing (7.24) with (7.22), it suffices to show that $A_i(k+d-1:k)\mathbf{1} \leq \eta_{i,l}$, where $A_i(k+d-1:k)\mathbf{1}$ is the i-th row sum of $A(k+d-1:k)$.

For $i \in S_1$, it is clear that $A_i(k)\mathbf{1} = c_i(k) = 1 - \alpha_{i0}(k) \triangleq \eta_{i,1}(k) < 1$. To compute $A_i(k+1:k)\mathbf{1}$, note that $A(k)\mathbf{1} \leq \gamma_i(k)$, where $\gamma_i(k) \in \mathbb{R}^n$ is obtained by replacing the i-th entry of $\mathbf{1}$ with $\eta_{i,1}(k)$. Let us first consider the following two cases:

1) $\alpha_{i0}(k) \leq \alpha_{i0}(k+1)$, which gives:

$$\begin{aligned}
A_i(k+1:k)\mathbf{1} \leq A_i(k+1)\gamma_i(k) &= \alpha_i(k+1)\eta_{i,1}(k) + \sum_{j\neq 0} \alpha_{ij}(k+1) \\
&= [1 - \sum_j \alpha_{ij}(k+1)]\eta_{i,1}(k) + \sum_{j\neq 0} \alpha_{ij}(k+1) \\
&= \eta_{i,1}(k) - [1 - \alpha_{i0}(k)] \sum_j \alpha_{ij}(k+1) + \sum_{j\neq 0} \alpha_{ij}(k+1) \\
&\leq \eta_{i,1}(k) - \alpha_{i0}(k+1)[1 - \sum_j \alpha_{ij}(k+1)] \\
&= \eta_{i,1}(k) - \alpha_{i0}(k+1)\alpha_i(k+1) \leq \eta_{i,1}(k).
\end{aligned}$$

2) $\alpha_{i0}(k) > \alpha_{i0}(k+1)$, in this case since $\alpha_{i0}(k) = 1 - \eta_{i,1}(k)$ we have $\eta_{i,1}(k) < 1 - \alpha_{i0}(k+1)$. Hence:

$$\begin{aligned} A_i(k+1:k)\mathbf{1} &\leq A_i(k+1)\gamma_i(k) \\ &< \alpha_i(k+1)[1-\alpha_{i0}(k+1)] + \sum_{j\neq 0}\alpha_{ij}(k+1) \\ &= 1 - \alpha_{i0}(k+1) - \alpha_i(k+1)\alpha_{i0}(k+1) \\ &= \eta_{i,1}(k+1) - \alpha_{i0}(k+1)\alpha_i(k+1) \leq \eta_{i,1}(k+1). \end{aligned}$$

By inference and induction we can show (7.22) for $l = 1$ and $\eta_{i,1} = 1 - T\beta s_* a_{i0}$.

For $j \in S_2$ which is connected to an agent $i \in S_1$ but not to the leader, it follows from $A(k)\mathbf{1} \leq \gamma_i(k)$ that

$$\begin{aligned} A_j(k+1:k)\mathbf{1} &\leq \alpha_{ji}(k+1)\eta_{i,1}(k) + 1 - \alpha_{ji}(k+1) \\ &= 1 - \alpha_{ji}(k+1)[1-\eta_{i,1}(k)] \triangleq \eta_{j,2}(k+1) < 1. \end{aligned}$$

Consequently we get that $A_j(k+1:k)\mathbf{1} \leq \gamma_{j,i}(k+1)$ where $\gamma_{j,i}(k+1) \in \mathbb{R}^n$ is obtained by replacing the j-th entry of $\gamma_i(k)$ with $\eta_{j,2}(k+1)$. Moving on, we find that

$$\begin{aligned} A_j(k+2:k)\mathbf{1} &\leq \alpha_j(k+2)\eta_{j,2}(k+1) + \alpha_{ji}(k+2)\eta_{i,1}(k) + 1 - \alpha_{ji}(k+2) - \alpha_j(k+2) \\ &= 1 - \alpha_{ji}(k+2)\alpha_{i0}(k) - \alpha_j(k+2)\alpha_{ji}(k+1)\alpha_{i0}(k) \\ &\leq 1 - (T\beta s_*)^2 a_{ji}a_{i0} \triangleq \eta_{j,2}. \end{aligned}$$

Switching j to i, we can show (7.22) for $l = 2$ and $\eta_{i,2} = 1 - (T\beta s_*)^2 a_{ij}a_{j0}$.

We can continue the above analysis and obtain $\eta_{i,l} = 1 - (T\beta s_*)^l a_{i,i_1}\cdots a_{i_{l-1},i_l}$, where $i_l = 0$ and $(i,i1),\ldots,(i_{l-1},i_l)$ is the shortest path from i to 0. If we define $a_* = \min\{a_{ij} : (i,j) \in \bar{E}\}$, then we can take $\eta = 1 - (T\beta s_* a_*)^L$. ■

Theorem 7.3. *Under Assumptions 7.1 and 7.2, let the conditions (7.12) and (7.17) hold. Also, assume that G has no cycles, i.e. G is DAG. For a non-deterministic leader, the time-varying formation problem (7.6b) can be solved by the estimator (7.8) and the controller (7.10) with the ultimate bound Q_i given by $Q_i = \sum_j |\hat{c}_{ij}|U_0/\beta$.*

Proof. For each follower i, let the longest path from i to the leader be of length l_i. Accordingly, we can classify the followers into different groups H_l, so that $l_i = l$ for $i \in H_l$. Also, denote $H_0 = \{0\}$. Since there is no loop, it holds that $N_i \subseteq \bigcup_{l=0}^{i-1} H_i$ for any $i \in H_l, l \geq 1$. Below we analyze the ultimate bound in sequence of H_l.

1) For the agent $i \in H_1$ which has the only neighbour of the leader, it follows by replacing $a_{i0} = 1$ in (7.16) that

$$\bar{q}_i(k+1) = [1 - T\beta s_i(k)]\bar{q}_i(k) - T[\beta s_i(k)\tilde{q}_{i0}(k) + v_0(k)]. \tag{7.25}$$

Under the condition (7.17), we will show that $s_i(k) = 1$ for sufficiently large k, and (7.25) becomes

$$\bar{q}_i(k+1) = (1 - T\beta)\bar{q}_i(k) - T[\beta\tilde{q}_{i0}(k) + v_0(k)]. \tag{7.26}$$

To begin, let us define $D_i(k) = \|\bar{q}_i(k)\|^2$ and examine $\Delta D_i(k) = D_i(k+1) - D_i(k)$ (henceforth, we may omit the subscripts i, ij, $i0$ and the time step k when they can be easily inferred). From (7.25) one can obtain

$$\begin{aligned}
\Delta D &= (\bar{q} + Tsu - Tv)'(\bar{q} + Tsu - Tv) - \bar{q}'\bar{q} \\
&= T\left[T(s^2\|u\|^2 - 2su'v + \|v\|^2) + 2\bar{q}'(su - v)\right] \\
&= T\left[T(\hat{s}^2\|\hat{u}\|^2 - 2\hat{s}\hat{u}'v + \|v\|^2) + 2\bar{q}'(\hat{s}\hat{u} - v) + \varepsilon\right],
\end{aligned}$$

where $\hat{s} = U_i/\max\{U_i, \|\hat{u}\|\}$ with $\hat{u} = -\beta\bar{q}$, and $\varepsilon = (su - \hat{s}\hat{u})'[Tsu + T\hat{s}\hat{u} - 2Tv + 2\bar{q}]$. In the sequel we shall find the ultimate bound of $\bar{q}$ by examining when $\Delta D \leq 0$.

We firstly show that ε is e.c. Actually, as $\|Tsu + T\hat{s}\hat{u} - 2Tv + 2\bar{q}\| \leq 2[T(U_i + U_0) + \|\bar{q}\|]$ only grows at most linearly fast by (7.25), it suffices to show the EC of $su - \hat{s}\hat{u} = s(u - \hat{u}) - (\hat{s} - s)\hat{u}$. For the first term, we have $\|s(u - \hat{u})\| \leq \beta\|\tilde{q}\|$ which is e.c. For the second term, due to the EC of $\|\tilde{q}\|$, we can take $\beta\|\tilde{q}\| < U_i/2$ and find that $\max\{U_i, \|u\|\} \geq \max\{U_i, \beta\|\bar{q}\|\} - \beta\|\tilde{q}\| > 0$ for sufficiently large k. Then we can see that

$$\begin{aligned}
s - \hat{s} &= U_i/\max\{U_i, \|u\|\} - U_i/\max\{U_i, \|\hat{u}\|\} \\
&\leq \frac{U_i\beta\|\tilde{q}\|}{(\max\{U_i, \beta\|\bar{q}\|\} - \beta\|\tilde{q}\|)\max\{U_i, \beta\|\bar{q}\|\}} \\
&\leq [U_i\beta\|\tilde{q}\|]/[(U_i/2)U_i] = 2\beta\|\tilde{q}\|/U_i,
\end{aligned}$$

which implies that $|s-\hat{s}|$ is e.c. Since $\|\hat{u}\| = \beta\|\bar{q}\|$ grows at most linearly fast, we can achieve the EC of $|su-\hat{s}\hat{u}|$. In summary, for any $\varepsilon^* > 0$, there exists $K^* = K^*(\|\bar{q}(0)\|, \|\tilde{q}(0)\|, \varepsilon^*)$ such that $|\varepsilon| \le \varepsilon^*$ for $k \ge K^*$.

Below we shall show that $\hat{s} = 1$ in finite time, and we firstly consider $\hat{s} < 1$.

If $\hat{s} < 1$, then $\|\bar{q}\| > U_i/\beta$, $\hat{s} = U_i/\|\hat{u}\|$ and

$$\begin{aligned}\Delta D &\le T\Big[T(U_i + 2U_iU_0 + U_0^2) - 2\bar{q}'\Big(\frac{U_i}{\|\bar{q}\|}\bar{q} + v\Big) + |\varepsilon|\Big] \\ &\le T\left[T(U_i+U_0)^2 - 2(U_i-U_0)U_i/\beta + \varepsilon^*\right] \triangleq \delta(\varepsilon^*).\end{aligned}$$

Based on the condition (7.17), we can find a small ε^* so that $\delta(\varepsilon^*) < 0$. Therefore, $\Delta D \le \delta(\varepsilon^*) < 0$ after some time steps. Hence $\|\bar{q}\|$ will reduce to U_i/β in finite time, and we can proceed to $\hat{s} = 1$ in the next case.

If $\hat{s} = 1$, then $\|\bar{q}\| \le U_i/\beta$ and it holds that

$$\begin{aligned}\Delta D &\le T\big[(T\beta-2)\beta\|\bar{q}\|^2 + 2(1-T\beta)U_0\|\bar{q}\| + TU_0^2 + |\varepsilon|\big] \\ &= -T\big[((2-T\beta)\|\bar{q}\| + TU_0)(\beta\|\bar{q}\| - U_0) - |\varepsilon|\big].\end{aligned}$$

For $\beta\|\bar{q}\| > (U_i+U_0)/2 > U_0$, the above becomes

$$\Delta D \le -\frac{T}{2}\big[(1/\beta - T/2)(U_i+U_0) + TU_0\big](U_i-U_0) + T|\varepsilon|.$$

Similar to the previous case, we can show that there exists $K = K(\|\bar{q}(0)\|, \|\tilde{q}(0)\|)$ such that $\beta\|\bar{q}(K)\| \le (U_i+U_0)/2$.

At the same time, K can also be taken sufficiently large so that $\beta\|\tilde{q}(k)\| \le (U_i - U_0)/4$ for $k \ge K$, which follows that $\|u(K)\| = \beta\|\bar{q}(K) + \tilde{q}(K)\| \le (3U_i + U_0)/4 < U$, and (7.26) holds for $k = K$. Furthermore, we have $\beta\|\bar{q}(K+1)\| \le (U_i+U_0)/2 - T\beta(U_i-U_0)/4$, and hence $\|u(K+1)\| = \beta\|\bar{q}(K+1) + \tilde{q}(K+1)\| < (3U_i+U_0)/4 < U_i$. By induction we conclude that (7.26) holds for $k \ge K$, and the ultimate bound U_0/β can be established by noticing that $\tilde{q}(k)$ converges to 0. Thus, the following is achieved:

$$\limsup_{k\to\infty}\|\bar{q}_i(k)\| \le U_0/\beta,\ i \in H_1. \tag{7.27}$$

2) Moving on to $i \in H_2$ where $N_i \subseteq H_0 \cup H_1$. Define $r_i(k) = \sum_j a_{ij}[\bar{q}_i(k) - \bar{q}_j(k)]$, then we have $u_i(k) = -\beta\big[r_i(k) + \sum_j a_{ij}\tilde{q}_{ij}(k)\big]$, and the dynamics of $r_i(k)$ can be

derived from the above and (7.16) as

$$r_i(k+1) = (1 - T\beta s_i(k))r_i(k) - \varepsilon_i(k) - f_i(k), \tag{7.28}$$

where $\varepsilon_i(k)$ converges to 0 exponentially fast, and $f_i(k) = T\sum_j a_{ij}\bar{u}_j(k)$. Since $\limsup_{k\to\infty} \|\bar{u}_j(k)\| \leq U_0$ follows as a result of (7.27), we have $\limsup_{k\to\infty} \|f_i(k)\| \leq TU_0$. Following a similar analysis in 1), we can also maintain that $\limsup_{k\to\infty} \|r_i(k)\| \leq U_0/\beta$ for $i \in H_2$.

3) From H_3 onwards, we can repeat the same steps and conclude that $\limsup_{k\to\infty} \|r_i(k)\| \leq U_0/\beta$. Note that $r(k) = (C \otimes I)\bar{q}(k)$, where $\otimes$ denotes the Kronecker product, $\bar{q}(k) \triangleq [\bar{q}'_{10}(k), \ldots \bar{q}'_{n0}(k)]'$, $r(k) \triangleq [r'_1(k), \ldots r'_n(k)]'$, and C is defined in (7.18). Since $\bar{q}(k) = (C^{-1} \otimes I)r(k)$, we immediately get

$$\limsup_{k\to\infty} \|\bar{q}_i(k)\| \leq \sum_j |\hat{c}_{ij}| U_0/\beta. \tag{7.29}$$

We have completed the proof. ■

Remark 7.3. *Given $U_i > U_0$, (7.17) can be easily satisfied by small T or β. The requirement $U_i > U_0$ is also intuitively meaningful: if we see the upper bound U_0 of the nondeterministic input $v_0(k)$ as the maximum uncertainty, then the maximum control effort U_i must be larger than U_0 to overcome the uncertainty for global stability, otherwise $v_0(k)$ may cancel out $\bar{u}_i(k)$ and destabilize the system.*

Remark 7.4. *As can be seen in the proof, for a follower i connected to the leader, the left-hand side of (7.17) is the ultimate error bound for $\beta > 0$ and $U_i > U_0$, while the right-hand side is a scaled input bound of agent i. Consequently, (7.17) ensures that the saturation will be waived in finite time. In a DAG where followers can be categorized into different layers according to the longest path to the leader, the condition (7.17) ensures that each agent is able to overcome the maximum uncertainty induced by previous layers and achieve the global ultimate error bound. Note that here we address input saturation directly, instead of using the small gain approach which can only guarantee semi-global stability [128, 129].*

Remark 7.5. *Note that given any digraph satisfying Assumption 7.1, a hierarchical decomposition [127] can be used to identify a DAG G^* of the original graph, and the relative localization law (7.8c) can be applied to all edges (i, j) in the original graph, while the control input for each agent can be calculated using the*

information from its neighbors on G^* only. It can be seen that under this approach, we can still obtain $\lim_{k\to\infty} \|\tilde{q}_{ij}(k)\| = 0,\ \forall (i,j) \in \bar{E}$ at exponential rate and $\limsup_{k\to\infty} \|\bar{q}_i(k)\| = Q_0,\ \forall i \in V$, i.e. there is no compromise on the convergence and boundedness of the localization and formation errors. Indeed, in a networked system, the direct use of the DAG compared to a general digraph can offer multiple advantages. First, for the leader-following consensus, it has been shown in [133, 134] that the existence of cycles definitely degrades the convergence performance. Second, reducing the topology to DAG via some hierarchical decomposition technique would also help reduce the amount of communication needed in the network, while still guaranteeing the convergence and stability of the localization and formation errors. In this work we gloss over the hierarchical decomposition and study the stability of the system under DAG directly. For this special topology, we can see in the subsequent simulation that the global bound is almost as exactly as predicted by Theorem 7.3. The effect of loops in the topology is deferred to future investigations.

7.5 Simulation and Experiments

In this section we seek to verify the theoretical results using both numerical simulations and physical implementations. Video recording of the simulations and experiments in this section can be viewed at https://youtu.be/0MUBlM8vNGY.

7.5.1 Numerical Simulations

First. two simulations with 196 agents under the same DAG topology (see Figure 7.1) are presented to validate the theoretical findings of Theorems 7.1, 7.2 and 7.3 in this part.

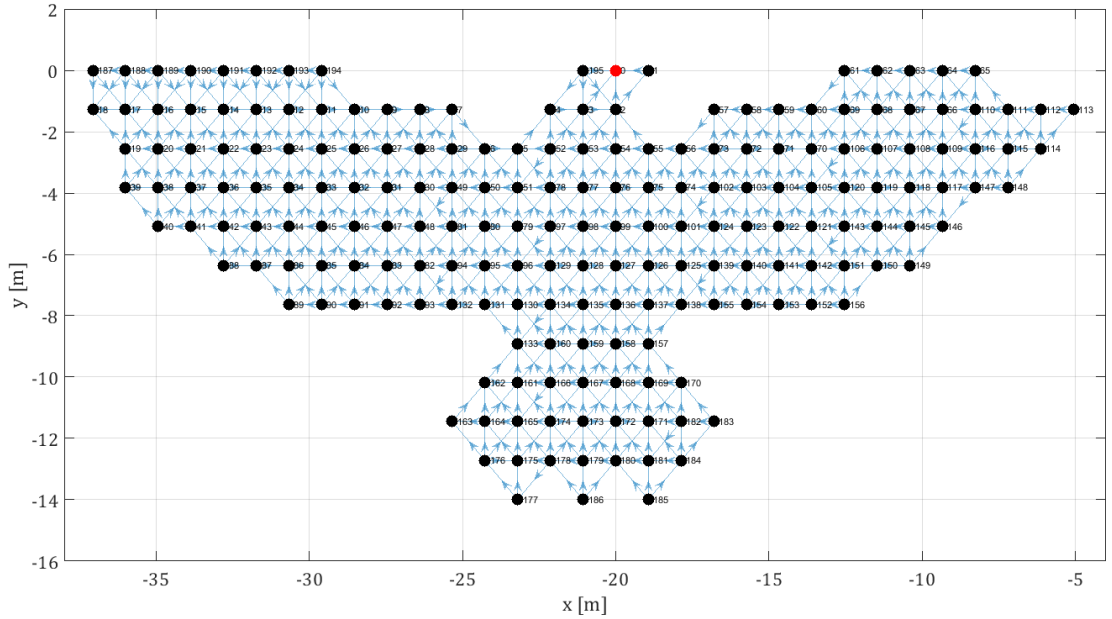

FIGURE 7.1: A swarm of 196 agents with DAG topology in a desired formation. The leader is indicated by the red dot.

The user-defined parameters and other values are chosen as follows:

$$
\begin{aligned}
&a_{ij} = 1/\left|N_i\right|, \ \forall (i,j)\bar{E}, \ i \in V; \\
&\Gamma_{ij}(0) = I, \ \forall (i,j) \in \bar{E}; \ \hat{q}_{ij} = 0, \ \forall (i,j) \in V; \ \beta_f = 0.9; \\
&T = 0.125; \ \beta = 7; U_i = 0.4, \ \forall i \in V; \\
&\sigma_i(k) = R(\psi(k)) \left(q_i^* + [-20 \ 0]'\right); \\
&R(\psi) = \begin{bmatrix} \cos\psi & -\sin\psi \\ \sin\psi & \cos\psi \end{bmatrix}, \ \psi(k) = \frac{-5\pi k}{32}; \\
&v_0(k) = \frac{1}{T}\left[f(k+1) - f(k)\right]; \ f(k) = \frac{10}{\sqrt{2}} \begin{bmatrix} \cos\left(\frac{\pi}{2048}\right) & \sin\left(\frac{\pi}{2048}\right) \end{bmatrix}; \\
&p_i(0) = 5 \begin{bmatrix} \cos\left(2\pi i/\left|\bar{G}\right|\right) \\ \sin\left(2\pi i/\left|\bar{G}\right|\right) \end{bmatrix}, \ \forall i \in \bar{V}.
\end{aligned}
$$

In this time-varying formation scheme, we choose $\sigma_i(k) = R(\psi(k))(q_i^* + [-20, 0]')$ where $R(\psi(k))$ is a periodic time-varying rotation matrix and q_i^* is the coordinate of agent i in Figure 7.1. We can verify (7.12) by direct computations with K_{ij} being the period of $R(\psi(k))$. As such, the PE condition is satisfied. It should be noted that the definition of $\sigma_i(k)$ based on a closed-form time-varying rotation

matrix here is just for convenience. In practice $\sigma_i(k)$ can be chosen as any sequence of setpoints so long as the PE condition is satisfied.

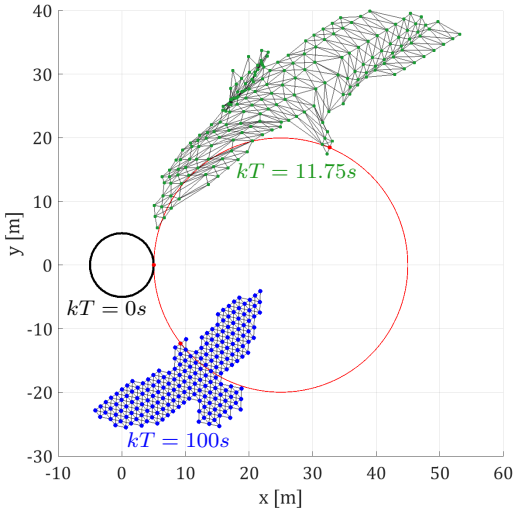

(a) Snapshots of the swarm system at three different time instances with a deterministic leader.

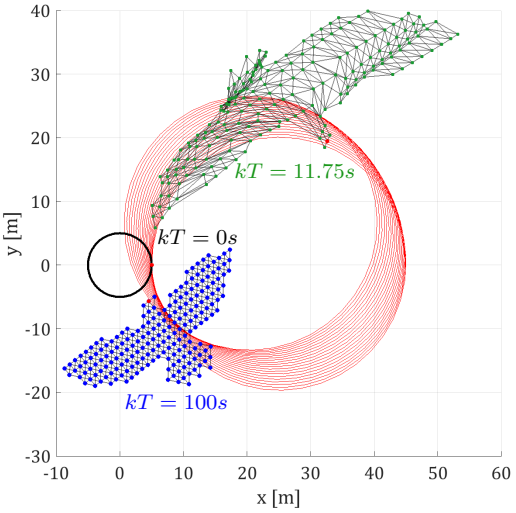

(b) Snapshots of the swarm system at three different time instances with a nondeterministic leader.

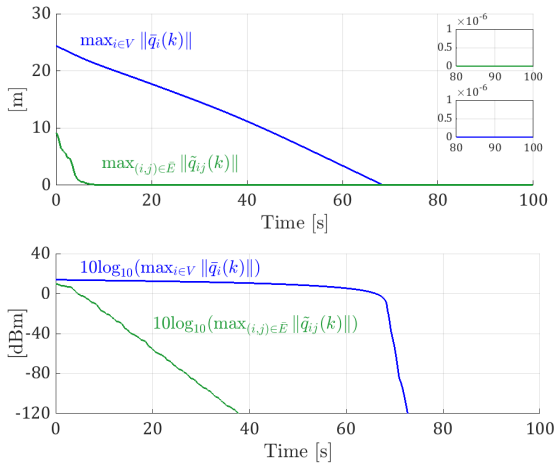

(c) Convergence of relative localization and time-varying formation errors (plotted at linear and logarithmic scales) confirms the predictions of Theorems 7.1 and 7.2.

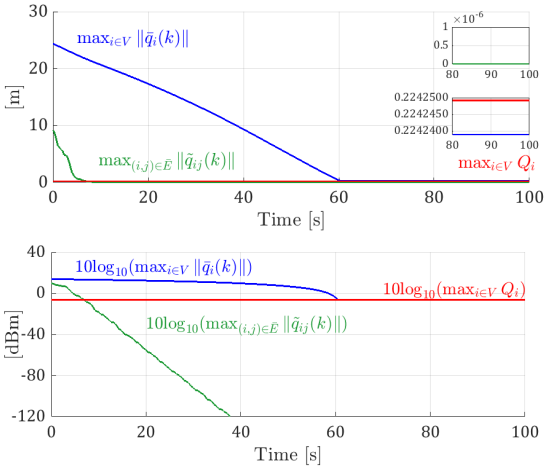

(d) Convergence of relative localization and time-varying formation errors (plotted at normal and logarithmic scales) confirms the predictions of Theorems 7.1 and 7.3.

FIGURE 7.2: Simulation of the swarm system in the deterministic and nondeterministic cases under DAG. The leader's trajectory through time is plotted by the red path in Figure 7.2a and Figure 7.2b. The positions of the followers at an intermediate time step and the final step are respectively marked with green dots and blue dots. The leader's positions at these steps are always marked with the red dot.

Thanks to the guarantee on PE condition, the localization errors converge to 0 exponentially fast, as seen in Figure 7.2c for the deterministic leader case and Figure 7.2d for the nondeterministic leader case. As predicted by Theorem 7.2, the

formation error is also observed to be e.c. in Figure 7.2c. For the nondeterministic leader case, we first find U_0 from the choice of $v_0(k)$ in Figure 7.2b, and then verify the condition (7.17). In Figure 7.2d we compare the maximum ultimate formation error bound with $\max_i Q_i$, and it can be seen that the predicted $\max_i Q_i$ is almost identical with the simulation result. Animated plots of these simulations as well as others with different topologies and formation shapes can be viewed at https://youtu.be/0MUBlM8vNGY.

Note that for the deterministic case, the topology can contain cycles. Thus, we rerun the simulation with a deterministic leader but the connections between the followers are now made undirected. Specifically, we add an edge (j, i) to the graph for every edge (i, j) in the original topology if both i and j are followers. As can be seen in Figure 7.3a, the predictions by Theorem 7.1 and 7.2 still hold. However, from Figure 7.3b, we can clearly see that the convergence rate of the formation error has been significantly reduced, which is in accordance with Remark 7.5. Indeed, other simulations with different topologies and choices of the reference trajectories $\sigma_i(k)$ yield the same result on the reduced convergence rate compared with DAG.

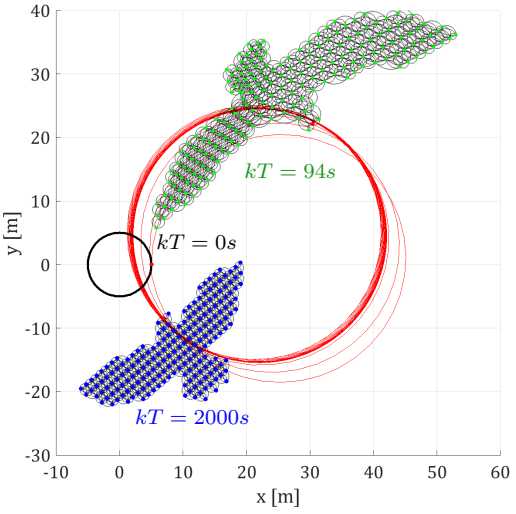

(a) Snapshots of the swarm system at three different time instances with a deterministic leader and multiple cycles.

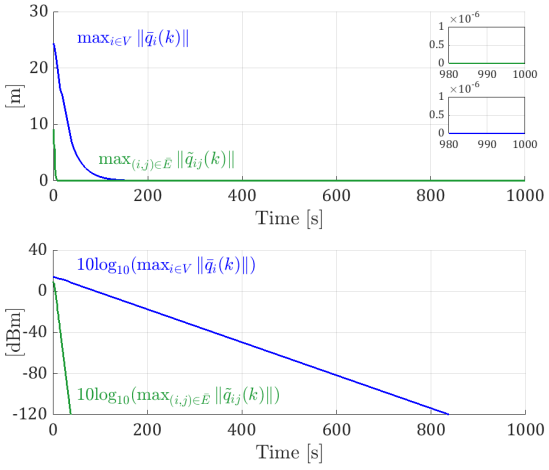

(b) Convergence of RL and TVF errors confirms predictions of Theorems 7.1 and 7.2. However the rate of convergence of formation error has significantly reduced compared to the DAG topology in Figure 7.2.

FIGURE 7.3: Simulation of the swarm system in the deterministic case with cycles in the topology. The leader's trajectory through time is plotted by the red path in Figure 7.3a.

7.5.2 Experiment on Quadcopters

The proposed PEARL-TVF scheme is further verified by implementation on three quadrotors in an indoor testing area. The quadrotors are enumerated by 0, 1, 2 and the edge set is chosen as $\bar{E} = \{(1,0),(2,0),(2,1)\}$. A set of high accuracy UWB ranging sensors [13, 70] is used for both distance measurements and communication between the quadrotors. The quadrotors are tracked by a motion capture system and the tracking information is fused with onboard IMU and optical flow measurements to obtain position estimates with 1cm accuracy. This is then used to calculate the displacement and communicated over the UWB network. The estimation and control signals are updated locally by each quadrotor every 100 ms in synchronization with the UWB network.

The user-defined parameters and other values are chosen as follows:

$$
\begin{aligned}
&T = 0.1s;\ \beta = 5;\ U_i = 0.25, \forall i \in V;\ \beta_f = 0.9;\\
&\Gamma_{ij}(0) = I, \forall (i,j) \in \bar{E};\ a_{10} = 1,\ a_{20} = a_{20} = 1/2;\\
&\sigma_0(k) = [0,\ 0]',\ \sigma_1(k) = -\sigma_2(k) = -\frac{7}{4}\left[\cos(\frac{\pi k}{72}),\ \sin(\frac{\pi k}{72})\right]';\\
&q_{10}(0) = -q_{20}(0) = [-2,\ 0]';\\
&\hat{q}_{10}(0) = -\hat{q}_{20}(0) = \frac{1}{2}\hat{q}_{21}(0) = [-0.75,\ 0]'.
\end{aligned}
$$

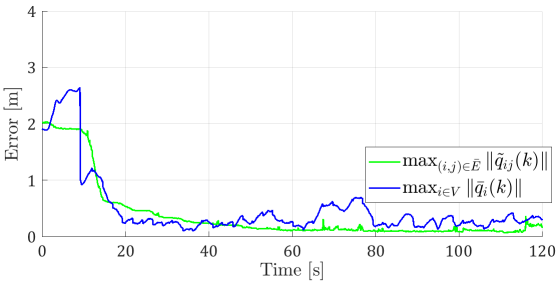

(a) Relative localization and formation errors in the experiment and main parameters.

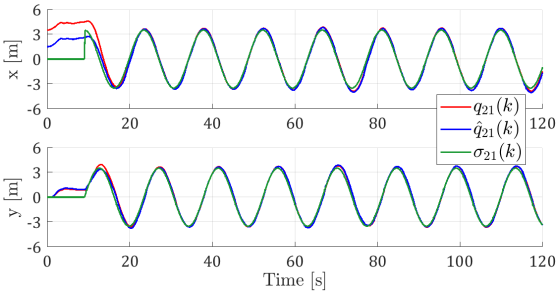

(b) Relative position estimate, ground truth and relative reference trajectory on the edge $(2,1)$.

FIGURE 7.4: Time evolution of the errors and relative states under the PEARL-TVF algorithm.

Figure 7.4a shows the time evolution of the relative localization and formation errors. It can be seen that both errors reduce to some small values, which are expected due to the existence of measurement errors. Figure 7.4b shows the time

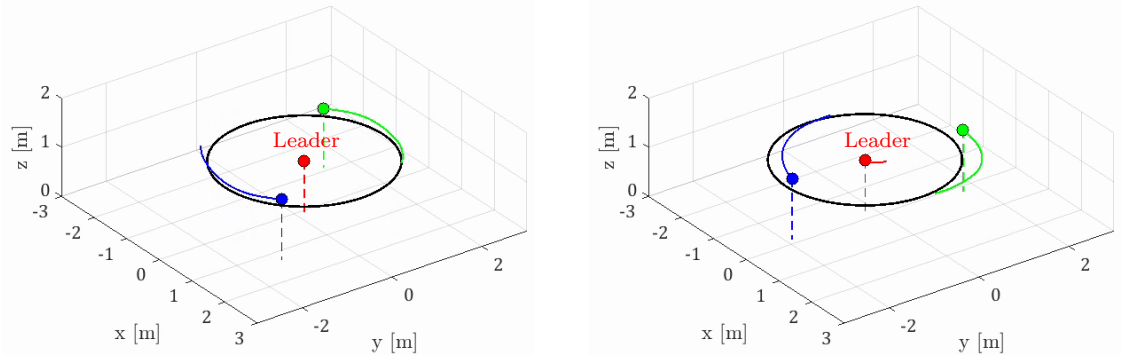

(a) When the leader stays static, the followers' trajectories converge to a circular reference trajectory centered at the leader.

(b) When the leader is shifted away, the followers' trajectories deviate from the circle but will converge back to it later.

FIGURE 7.5: Recorded 3D trajectories of the robots over some short periods.

evolution of the relative position estimates $\hat{q}_{21}(k)$, in comparison with the ground truth $q_{21}(k)$ from the motion capture system and the relative reference trajectory $\sigma_{21}(k)$. We can observe that $\hat{q}_{21}(k)$ and $q_{21}(k)$ quickly converge to the reference trajectory $\sigma_{ij}(k)$ under the effect of the PEARL-TVF algorithm. Similar convergence can also be observed on other edges.

Also, it is worth mentioning that the formation error slightly increases and then decreases when the leader is shifted away. Figure 7.5 shows some snapshots of the formation when the leader is static and then moves to a new position, temporarily increasing the formation error. A video recording of the experiment overlaid with other real-time plots can be viewed at `https://youtu.be/0MUBlM8vNGY`.

7.6 Conclusion

In this chapter, we have introduced a distributed distance-based relative localization and time-varying formation control scheme for multi-robot systems with bounded input. By embedding the PE condition into the time-varying formation reference trajectories, we achieve EC for relative localization, which facilities e.c. time-varying formation in the deterministic leader case, and a globally stable time-varying formation in the nondeterministic leader under DAG. Numerical and emperical examples were used to demonstrate the theoretical findings.

Chapter 8

Conclusion & Future works

8.1 Conclusion

In this thesis we have developed a number of integrated relative localization and navigation schemes for MAVs. In all of these schemes, as relative localization is achieved by combining UWB-based ranging measurement with visual odometry information, the MAV system can operate independently from external localization systems. Many important technical and theoretical results have been achieved, specifically:

- Chapter 3 proposed a sensor fusion scheme to combine UWB ranging measurements and other onboard sensors to achieve robust relative localization and tracking of a target in close range. UWB-based communication and strategic installation of UWB nodes were also deliberated to increase the efficiency and observability of the relative position estimate. Extensive experiments were carried out to demonstrate effectiveness and accuracy of this method, even under the uncertainty on the velocity of the target.

- To complement the sensor fusion scheme which is only effective at close range, in Chapter 4 we developed a new method to allow the MAV to navigate towards the target from a large distance. Asymptotic convergence of the navigation task was established in the noise-free case, and the stability under distance measurement noise was also investigated. Comprehensive simulation was carried out to study the performance of the system under different

choices of control gains, and real-world experiments were conducted to verify the theorectical findings. Moreover, it can be seen that all subsequent chapters have inherited one or several important developments achieved in this chapter, i.e. the discrete-time distance-displacement-based relative localization technique, the practical control scheme with input saturation, and the new insights into the PE condition.

- Chapter 5 has innovated the autonomous docking operation for MAV in GPS-denied conditions by combining the close range sensor fusion scheme with the long range relative localization and navigation technique. By using the developed distance-based relative localization technique, the proposed system has resolved a prevalent limitation of existing methods, i.e. the capability to locate and approach the target before visual tracking can be effective for landing. Extensive experiments results clearly demonstrated the performance of the autonomous docking system even when the MAV starts from over 50m away.

- Chapter 6 made an initial attempt on cooperative scheme of multi-MAV system. Specifically, with the goal of controlling the MAVs to follow a leader, the use of specialized agents was comtemplated to maintain p.e. trajectories that facilitate EC of both *relative localization* and *tracking* errors. Discrete-time formulation and control input saturation have been taken into account to ensure the practical implementability of the proposed technique. Several experiments on quadcopter in GPS-denied conditions were carried out to validate the efficacy of the proposed scheme.

- Chapter 7 proposed a novel mutually reinforcing integration scheme for relative localization and time-varying formation of the MAV swarm, in which by ensuring that the the predefined time-varying formation reference trajectories satisfy the PE condition, EC of relative localization can be achieved; reciprocally, the EC of the time-varying formation formation can be achieved for a globally reachable and deterministic leader, and ultimately bounded error for a nondeterministic leader under DAG topology. Experiments on quadcopters were also carried out to further validate the theorectical findings.

8.2 Future Works

Many interesting issues would deserve further investigations

- In most chapters, it has been assumed that the orientations of the vehicles are referenced to a common frame. While this condition can be satisfied by having all of the vehicles measure and exchange their heading in the earth magnetic frame, this can be troublesome in some practical scenarios where there is magnetic interference, or that there is simply no direct measurement of the heading. Thus in the future it is worth investigating other estimation schemes where the relative heading can also be estimated to improve the flexibility of the system.

- In Chapters 5 to 7 we have employed different variants of the adaptive relative localization technique that combines distance and displacement measurements. In this thesis, for convenience of implementation, a simple VIO system was employed. However it has been shown in Chapter 6 that the quality of the displacement measurement can significantly influence the accuracy of the estimate. Thus it is necessary that further investigations are done to improve the accuracy with better VIO techniques.

- So far, we have studied the cooperative localization and control scheme with simple single-integrator dynamics. While it was intentionally imposed that the control input be proactively bounded so that other control techniques can be used to realize the single-integrator model, it is worth investigating the extension of current study to double-integrator dynamics or unicycle dynamics to better match the dynamics of MAVs.

- Last but not least, in Chapter 7, for the non-determistic case, we have shown that the system is stable given that the topology is a DAG. Thus it is necessary to investigate the stability of the system under a more general topology.

Author's Publications[1]

Journal Articles

- **Thien-Minh Nguyen**, Zhirong Qiu, Muqing Cao, Thien Hoang Nguyen, Lihua Xie, "Single Landmark Distance-Based Navigation", in *IEEE Transactions on Control Systems Technology*, Early Access, 2019.

- **Thien-Minh Nguyen**, Zhirong Qiu, Thien Hoang Nguyen, Muqing Cao, Lihua Xie, "Distance-Based Cooperative Relative Localization for Leader-Following Control of MAVs", in *IEEE Robotics and Automation Letters*, vol. 4, no. 4, pp. 3641-3648, 2019. The contents of this paper are also selected by IROS'19 Program Committee for presentation at the Conference.

- **Thien-Minh Nguyen***, Zhirong Qiu*, Thien Hoang Nguyen, Muqing Cao, Lihua Xie, "Persistently-Excited Adaptive Relative Localization and Time-Varying Formation Control of Robot Swarms", in *IEEE Transactions on Robotics*, Early Access, 2019.

- Xu Fang, Chen Wang, **Thien-Minh Nguyen**, and Lihua Xie, "Graph Optimization Approach to Range-Based Localization", in *IEEE Transactions on Systems, Man, and Cybernetics: Systems*, Early Access, 2020.

- Thien Hoang Nguyen, **Thien-Minh Nguyen**, Muqing Cao, and Lihua Xie, "Loosely-Coupled Ultra-Wideband-Aided Scale Correction for Monocular Visual Odometry", in *Unmanned Systems*, Early Access, 2020.

[1] The superscript * indicates joint first authors

Conference Proceedings

- Thien Hoang Nguyen, **Thien-Minh Nguyen**, Lihua Xie, "Tightly-Coupled Single-Anchor Ultra-Wideband-Aided Monocular Visual Odometry System", in *2019 IEEE International Conference on Robotics and Automation (ICRA), accepted, to appear.*

- **Thien-Minh Nguyen**, Thien Hoang Nguyen, Muqing Cao, Zhirong Qiu, Lihua Xie, "Integrated UWB-Vision Approach for Autonomous Docking of UAVs in GPS-Denied Environments", in *2019 IEEE International Conference on Robotics and Automation (ICRA), Montreal, QC, Canada, 2019, pp. 9603-9609. IEEE, 2019.*

- **Thien-Minh Nguyen**, Zhirong Qiu, Muqing Cao, Thien Hoang Nguyen, Lihua Xie, "An Integrated Localization-Navigation Scheme for Distance-Based Docking of UAVs", in *2018 IEEE/RSJ International Conference on Intelligent Robots and Systems (IROS), Madrid, Spain, pp. 5245-5250. IEEE, 2018.*

- **Thien-Minh Nguyen**, Abdul Hanif Zaini, Chen Wang, Kexin Guo, and Lihua Xie, "Robust Target-Relative Localization with Ultra-Wideband Ranging and Communication", in *2018 IEEE International Conference on Robotics and Automation (ICRA), Brisbane, QLD, Australia, pp. 2312-2319. IEEE, 2018.*

- Chen Wang, Tete Ji, **Thien-Minh Nguyen**, Lihua Xie, "Correlation Flow: Robust Optical Flow Using Kernel Cross-Correlators", in *2018 IEEE International Conference on Robotics and Automation (ICRA), Brisbane, QLD, Australia, pp. 836-841. IEEE, 2018.*

- Chen Wang, Handuo Zhang, **Thien-Minh Nguyen**, Lihua Xie, "Ultra-Wideband Aided Fast Localization and Mapping System", in *2017 IEEE/RSJ International Conference on Intelligent Robots and Systems (IROS), Vancouver, BC, Canada, pp. 1602-1609. IEEE, 2017.*

- **Thien-Minh Nguyen**, Lihua Xie, "Least-Squares Based Recursive Optimization for Distance-Based Source Localization", in *2018 14th IEEE International Conference on Control and Automation (ICCA), Anchorage, AK, USA, pp. 75-80. IEEE, 2018.*

- Thien Hoang Nguyen*, Muqing Cao*, **Thien-Minh Nguyen***, Lihua Xie, "Post-Mission Autonomous Return and Precision Landing of UAV", in *2018 15th International Conference on Control, Automation, Robotics and Vision (ICARCV), Singapore, pp. 1747-1752. IEEE, 2018.*

- Xu Fang, Chen Wang, **Thien-Minh Nguyen**, Lihua Xie, "Model-Free Approach for Sensor Network Localization with Noisy Distance Measurement", in *2018 15th International Conference on Control, Automation, Robotics and Vision (ICARCV), Singapore, pp. 1973-1978. IEEE, 2018.*

- **Thien-Minh Nguyen**, Xiuxian Li, and Lihua Xie, "Barrier Coverage by Heterogeneous Sensor Network with Input Saturation", in *2017 11th Asian Control Conference (ASCC), Gold Coast, QLD, Australia, pp. 1719-1724. IEEE, 2017..*

- **Thien-Minh Nguyen**, Abdul Hanif Zaini, Kexin Guo, and Lihua Xie, "An Ultra-Wideband-Based Multi-UAV Localization System in GPS-denied Environments", in *2016 International Micro Air Vechicle Competition and Conference (IMAV), Beijing, China*, **Best Paper Finalist**.

- Kexin Guo, Zhirong Qiu, Wei Meng, **Thien-Minh Nguyen** and Lihua Xie, "Relative Localization for Quadcopters Using Ultra-wideband Sensors", in *2016 International Micro Air Vechicle Competition and Conference (IMAV), Beijing, China.*

Bibliography

[1] Francesco Nex and Fabio Remondino. Uav for 3d mapping applications: a review. *Applied Geomatics*, 6(1):1–15, 2014. 1

[2] Chunhua Zhang and John M Kovacs. The application of small unmanned aerial systems for precision agriculture: a review. *Precision Agriculture*, 13 (6):693–712, 2012. 1

[3] Juntong Qi, Dalei Song, Hong Shang, Nianfa Wang, Chunsheng Hua, Chong Wu, Xin Qi, and Jianda Han. Search and rescue rotary-wing uav and its application to the lushan ms 7.0 earthquake. *Journal of Field Robotics*, 33 (3):290–321, 2016. 1

[4] Giuseppe Loianno, Justin Thomas, and Vijay Kumar. Cooperative localization and mapping of mavs using rgb-d sensors. In *2015 IEEE International Conference on Robotics and Automation (ICRA)*, pages 4021–4028. IEEE, 2015. 1

[5] Antonio Adaldo, Sina Sharif Mansouri, Christoforos Kanellakis, Dimos V Dimarogonas, Karl H Johansson, and George Nikolakopoulos. Cooperative coverage for surveillance of 3d structures. In *2017 IEEE/RSJ International Conference on Intelligent Robots and Systems (IROS)*, pages 1838–1845. IEEE, 2017. 1

[6] Jonathan Fink, Nathan Michael, Soonkyum Kim, and Vijay Kumar. Planning and control for cooperative manipulation and transportation with aerial robots. *The International Journal of Robotics Research*, 30(3):324–334, 2011. 1

[7] Giuseppe Loianno and Vijay Kumar. Cooperative transportation using small quadrotors using monocular vision and inertial sensing. *IEEE Robotics and Automation Letters*, 3(2):680–687, 2018. 1

[8] Jamie Condliffe. A 100-drone swarm, dropped from jets, plans its own moves, 2017. 1

[9] Alex Kushleyev, Daniel Mellinger, Caitlin Powers, and Vijay Kumar. Towards a swarm of agile micro quadrotors. *Autonomous Robots*, 35(4):287–300, 2013. 2, 9

[10] Yash Mulgaonkar, Gareth Cross, and Vijay Kumar. Design of small, safe and robust quadrotor swarms. In *2015 IEEE International Conference on Robotics and Automation (ICRA)*, pages 2208–2215. IEEE, 2015.

[11] James A Preiss, Wolfgang Honig, Gaurav S Sukhatme, and Nora Ayanian. Crazyswarm: A large nano-quadcopter swarm. In *2017 IEEE International Conference on Robotics and Automation (ICRA)*, pages 3299–3304. IEEE, 2017. 2, 9, 10

[12] Kexin Guo, Zhirong Qiu, Cunxiao Miao, Abdul Hanif Zaini, Chun-Lin Chen, Wei Meng, and Lihua Xie. Ultra-wideband-based localization for quadcopter navigation. *Unmanned Systems*, 4(01):23–34, 2016. 2, 14, 43

[13] Thien-Minh Nguyen, Abdul Hanif Zaini, Kexin Guo, and Lihua Xie. An ultra-wideband-based multi-uav localization system in gps-denied environments. In *International Micro Air Vehicle Competition and Conference 2016*, pages 56–61, Beijing, China, Oct 2016. 14, 43, 69, 84, 129

[14] Mark W. Mueller, Michael Hamer, and Raffaello D'Andrea. Fusing ultra-wideband range measurements with accelerometers and rate gyroscopes for quadrocopter state estimation. In *2015 IEEE International Conference on Robotics and Automation (ICRA)*, pages 1730–1736. IEEE, 2015. xxi, 14, 15

[15] Anton Ledergerber, Michael Hamer, and Raffaello D'Andrea. A robot self-localization system using one-way ultra-wideband communication. In *2015 IEEE/RSJ International Conference on Intelligent Robots and Systems (IROS)*, pages 3131–3137. IEEE, 2015. xxi, 13, 14

[16] José Paredes, Fernando Álvarez, Teodoro Aguilera, and José Villadangos. 3d indoor positioning of uavs with spread spectrum ultrasound and time-of-flight cameras. *Sensors*, 18(1):89, 2018. 2, 11

[17] Reza Olfati-Saber. Flocking for multi-agent dynamic systems: Algorithms and theory. *IEEE Transactions on Automatic Control*, 51(3):401–420, 2006. 2, 94, 112

[18] Mohammad Deghat, Brian DO Anderson, and Zhiyun Lin. Combined flocking and distance-based shape control of multi-agent formations. *IEEE Transactions on Automatic Control*, 61(7):1824–1837, 2016. 2

[19] Xiwang Dong, Bocheng Yu, Zongying Shi, and Yisheng Zhong. Time-varying formation control for unmanned aerial vehicles: Theories and applications. *IEEE Transactions on Control Systems Technology*, 23(1):340–348, 2015. 2

[20] Kevin ZY Ang, Xiangxu Dong, Wenqi Liu, Geng Qin, Shupeng Lai, Kangli Wang, Dong Wei, Songyuan Zhang, Phang Swee King, Xudong Chen, et al. High-precision multi-uav teaming for the first outdoor night show in singapore. *Unmanned Systems*, pages 1–27, 2018.

[21] Thien-Minh Nguyen, Xiuxian Li, and Lihua Xie. Barrier coverage by heterogeneous sensor network with input saturation. In *2017 11th Asian Control Conference (ASCC)*, pages 1719–1724. IEEE, 2017. 2

[22] Bing Zhu, Abdul Hanif Bin Zaini, and Lihua Xie. Distributed guidance for interception by using multiple rotary-wing unmanned aerial vehicles. *IEEE Transactions on Industrial Electronics*, 64(7):5648–5656, 2017. 2

[23] Bing Zhu, Juanjuan Xu, Abdul Hanif Bin Zaini, and Lihua Xie. A three-dimensional integrated guidance law for rotary uav interception. In *2016 12th IEEE International Conference on Control and Automation (ICCA)*, pages 726–731. IEEE, 2016.

[24] Bing Zhu, Lihua Xie, and Chun Yin. Dynamic mission allocation for interceptions by using multiple rotary-wing uavs. In *2017 11th Asian Control Conference (ASCC)*, pages 441–446. IEEE, 2017. 2

[25] Shaojie Shen, Nathan Michael, and Vijay Kumar. 3d indoor exploration with a computationally constrained mav. In *Robotics: Science and Systems*, 2011. 2

[26] Shaojie Shen, Nathan Michael, and Vijay Kumar. Autonomous multi-floor indoor navigation with a computationally constrained mav. In *2011 IEEE*

International Conference on Robotics and Automation (ICRA), pages 20–25. IEEE, 2011.

[27] Shaojie Shen, Yash Mulgaonkar, Nathan Michael, and Vijay Kumar. Vision-based state estimation and trajectory control towards high-speed flight with a quadrotor. In *Robotics: Science and Systems*, volume 1. Citeseer, 2013.

[28] Shaojie Shen, Yash Mulgaonkar, Nathan Michael, and Vijay Kumar. Multi-sensor fusion for robust autonomous flight in indoor and outdoor environments with a rotorcraft mav. In *2014 IEEE International Conference on Robotics and Automation (ICRA)*, pages 4974–4981. IEEE, 2014. xxi, 17, 18

[29] Shaojie Shen, Nathan Michael, and Vijay Kumar. Tightly-coupled monocular visual-inertial fusion for autonomous flight of rotorcraft mavs. In *2015 IEEE International Conference on Robotics and Automation (ICRA)*, pages 5303–5310. IEEE, 2015.

[30] Rodrigo Munguía, Sarquis Urzua, Yolanda Bolea, and Antoni Grau. Vision-based slam system for unmanned aerial vehicles. *Sensors*, 16(3):372, 2016.

[31] Giuseppe Loianno, Chris Brunner, Gary McGrath, and Vijay Kumar. Estimation, control, and planning for aggressive flight with a small quadrotor with a single camera and imu. *IEEE Robotics and Automation Letters*, 2(2): 404–411, 2017. xxi, 2, 19, 20, 74

[32] Aaron Weinstein, Adam Cho, Giuseppe Loianno, and Vijay Kumar. Visual inertial odometry swarm: An autonomous swarm of vision-based quadrotors. *IEEE Robotics and Automation Letters*, 3(3):1801–1807, 2018. 2

[33] Patrik Schmuck. Multi-uav collaborative monocular slam. In *2017 IEEE International Conference on Robotics and Automation (ICRA)*, pages 3863–3870. IEEE, 2017. 2

[34] Timothy Stirling, James Roberts, Jean-Christophe Zufferey, and Dario Floreano. Indoor navigation with a swarm of flying robots. In *2012 IEEE International Conference on Robotics and Automation (ICRA)*, pages 4641–4647. IEEE, 2012. 3, 21

[35] James F Roberts, Timothy Stirling, Jean-Christophe Zufferey, and Dario Floreano. 3-d relative positioning sensor for indoor flying robots. *Autonomous Robots*, 33(1-2):5–20, 2012. 21

[36] Tobias Nägeli, Christian Conte, Alexander Domahidi, Manfred Morari, and Otmar Hilliges. Environment-independent formation flight for micro aerial vehicles. In *2014 IEEE/RSJ International Conference on Intelligent Robots and Systems (IROS)*, pages 1141–1146. IEEE, 2014. xxi, 21

[37] Steven Roelofsen, Denis Gillet, and Alcherio Martinoli. Reciprocal collision avoidance for quadrotors using on-board visual detection. In *2015 IEEE/RSJ International Conference on Intelligent Robots and Systems (IROS)*, pages 4810–4817. IEEE, 2015. 3, 21

[38] Steven van der Helm, Kimberly N McGuire, Mario Coppola, and Guido CHE de Croon. On-board range-based relative localization for micro aerial vehicles in indoor leader-follower flight. *arXiv preprint arXiv:1805.07171*, 2018. 3, 21, 22

[39] Matthew Turpin, Nathan Michael, and Vijay Kumar. Trajectory design and control for aggressive formation flight with quadrotors. *Autonomous Robots*, 33(1-2):143–156, 2012. 9, 10

[40] Sergei Lupashin, Markus Hehn, Mark W Mueller, Angela P Schoellig, Michael Sherback, and Raffaello D'Andrea. A platform for aerial robotics research and demonstration: The flying machine arena. *Mechatronics*, 2014. 9

[41] Nel Samama. *Global positioning: Technologies and performance*, volume 7. John Wiley & Sons, 2008. 10

[42] Hui Liu, Houshang Darabi, Pat Banerjee, and Jing Liu. Survey of wireless indoor positioning techniques and systems. *IEEE Transactions on Systems, Man, and Cybernetics, Part C (Applications and Reviews)*, 37(6):1067–1080, 2007. 11

[43] Guoqiang Mao, Barış Fidan, and Brian DO Anderson. Wireless sensor network localization techniques. *Computer Networks*, 51(10):2529–2553, 2007.

[44] Balaram Singh, Santosh Kumar Sahoo, and Soumya Ranjan Pradhan. Performance evaluation of anchor-based range-based localization systems in wireless sensor networks. *International Journal of Computer Applications*, 52 (17), 2012.

[45] José-Luis Rullán-Lara, Sergio Salazar, and Rogelio Lozano. Real-time localization of an uav using kalman filter and a wireless sensor network. *Journal of Intelligent & Robotic Systems*, 65(1-4):283–293, 2012. 11

[46] Faheem Zafari, Athanasios Gkelias, and Kin K Leung. A survey of indoor localization systems and technologies. *IEEE Communications Surveys & Tutorials*, 2019. xxvii, 11

[47] Andrew Singer, Michael Oelze, and Anthony Podkowa. Mbps experimental acoustic through-tissue communications: Meat-comms. In *2016 IEEE 17th International Workshop on Signal Processing Advances in Wireless Communications (SPAWC)*, pages 1–4. IEEE, 2016. 11

[48] Sima Nadler, Vladimir Soroka, Omri Fuchs, Roni Korenshtein, and Eyal Sonsino. Presence zones for contextual location based services. *Innovations in Clouds, Internet and Networks*, 2008. 11

[49] Sinem Coleri Ergen. Zigbee/ieee 802.15. 4 summary. *UC Berkeley, September*, 10:17, 2004. 11

[50] Majid Shaik. Ultra wide-band vs. wi-fia study and comparison of the two technologies, 2014. 11

[51] Bemri. Visible light communication (vlc/li-fi) systems, 2016. 11

[52] Rainer Mautz. Indoor positioning technologies. *ETH Zurich's Research Collection*, 2012. URL https://doi.org/10.3929/ethz-a-007313554. xxi, 12

[53] Xu Fang, Chen Wang, Thien-Minh Nguyen, and Lihua Xie. Model-free approach for sensor network localization with noisy distance measurement. In *2018 15th International Conference on Control, Automation, Robotics and Vision (ICARCV)*, pages 1973–1978. IEEE, 2018. 14

[54] Chen Wang, Handuo Zhang, Thien-Minh Nguyen, and Lihua Xie. Ultra-Wideband Aided Fast Localization and Mapping System. In *2017 IEEE/RSJ International Conference on Intelligent Robots and Systems (IROS)*. IEEE, 2017. 14

[55] Janis Tiemann and Christian Wietfeld. Scalable and precise multi-uav indoor navigation using tdoa-based uwb localization. In *2017 International*

Conference on Indoor Positioning and Indoor Navigation (IPIN), pages 1–7. IEEE, 2017. 14

[56] Jiaxin Li, Yingcai Bi, Kun Li, Kangli Wang, Feng Lin, and Ben M Chen. Accurate 3d localization for mav swarms by uwb and imu fusion. In *2018 14th IEEE International Conference on Control and Automation (ICCA)*, pages 100–105. IEEE, 2018. 14

[57] Ji Zhang and Sanjiv Singh. Laser–visual–inertial odometry and mapping with high robustness and low drift. *Journal of Field Robotics*, 35(8):1242–1264, 2018. xxi, 18

[58] Raul Mur-Artal, Jose Maria Martinez Montiel, and Juan D Tardos. Orb-slam: a versatile and accurate monocular slam system. *IEEE Transactions on Robotics*, 31(5):1147–1163, 2015. 17

[59] Dirk Hähnel, Sebastian Thrun, Ben Wegbreit, and Wolfram Burgard. Towards lazy data association in slam. In *Robotics Research. The Eleventh International Symposium*, pages 421–431. Springer, 2005. 17

[60] Paul Newman and Kin Ho. Slam-loop closing with visually salient features. In *2005 IEEE International Conference on Robotics and Automation (ICRA)*, pages 635–642. IEEE, 2005. 17

[61] Rainer Kümmerle, Giorgio Grisetti, Hauke Strasdat, Kurt Konolige, and Wolfram Burgard. g 2 o: A general framework for graph optimization. In *2011 IEEE International Conference on Robotics and Automation (ICRA)*, pages 3607–3613. IEEE, 2011. 17

[62] Armin Hornung, Kai M Wurm, Maren Bennewitz, Cyrill Stachniss, and Wolfram Burgard. Octomap: An efficient probabilistic 3d mapping framework based on octrees. *Autonomous Robots*, 34(3):189–206, 2013. 17

[63] Dominik Honegger, Lorenz Meier, Petri Tanskanen, and Marc Pollefeys. An open source and open hardware embedded metric optical flow cmos camera for indoor and outdoor applications. In *2013 IEEE International Conference on Robotics and Automation (ICRA)*, pages 1736–1741. IEEE, 2013. xxi, 19, 74, 105

[64] Sunglok Choi, Jaehyun Park, and Wonpil Yu. Resolving scale ambiguity for monocular visual odometry. In *2013 10th International Conference on Ubiquitous Robots and Ambient Intelligence (URAI)*, pages 604–608. IEEE, 2013. 19

[65] Bernd Manfred Kitt, Joern Rehder, Andrew D. Chambers, Miriam Schonbein, Henning Lategahn, and Sanjiv Singh. Monocular visual odometry using a planar road model to solve scale ambiguity. In *European Conference on Mobile Robots*, 2011.

[66] Richard Hartley and Andrew Zisserman. *Multiple view geometry in computer vision*. Cambridge University Press, 2003.

[67] Hauke Strasdat, J Montiel, and Andrew J Davison. Scale drift-aware large scale monocular slam. *Robotics: Science and Systems VI*, 2, 2010. 19

[68] Jakob Engel, Jörg Stückler, and Daniel Cremers. Large-scale direct slam with stereo cameras. In *2015 IEEE/RSJ International Conference on Intelligent Robots and Systems (IROS)*, pages 1935–1942. IEEE, 2015. 19

[69] Benjamin Hepp, Tobias Nägeli, and Otmar Hilliges. Omni-directional person tracking on a flying robot using occlusion-robust ultra-wideband signals. In *2016 IEEE/RSJ International Conference on Intelligent Robots and Systems (IROS)*, pages 189–194. IEEE, 2016. 22, 27

[70] Thien-Minh Nguyen, Abdul Hanif Zaini, Chen Wang, Kexin Guo, and Lihua Xie. Robust target-relative localization with ultra-wideband ranging and communication. In *2018 IEEE International Conference on Robotics and Automation (ICRA)*, pages 2312–2319. IEEE, 2018. 84, 129

[71] Mario Coppola, Kimberly N McGuire, Kirk YW Scheper, and Guido CHE de Croon. On-board communication-based relative localization for collision avoidance in micro air vehicle teams. *Autonomous Robots*, pages 1–19, 2018. 22

[72] Jianlin Chen, Devin Raye, Wahab Khawaja, Priyanka Sinha, and Ismail Guvenc. Impact of 3d uwb antenna radiation pattern on air-to-ground drone connectivity. In *2018 IEEE 88th Vehicular Technology Conference (VTC-Fall)*, pages 1–5, Aug 2018. doi: 10.1109/VTCFall.2018.8690726. 22

[73] Guofei Chai, Che Lin, Zhiyun Lin, and Weidong Zhang. Consensus-based cooperative source localization of multi-agent systems with sampled range measurements. *Unmanned Systems*, 2(03):231–241, 2014. 22, 25, 90

[74] Guofei Chai, Che Lin, Zhiyun Lin, and Minyue Fu. Single landmark based collaborative multi-agent localization with time-varying range measurements and information sharing. *Systems & Control Letters*, 87:56–63, 2016. 22, 25, 90, 92

[75] Barış Fidan, Soura Dasgupta, and Brian Anderson. Adaptive range-measurement-based target pursuit. *International Journal of Adaptive Control and Signal Processing*, 27(1-2):66–81, 2013. 22, 23, 44

[76] Barış Fidan and Ilknur Umay. Adaptive environmental source localization and tracking with unknown permittivity and path loss coefficients. *Sensors*, 15(12):31125–31141, 2015.

[77] Barış Fidan, Ahmet Çamlıca, and Samet Güler. Least-squares-based adaptive target localization by mobile distance measurement sensors. *International Journal of Adaptive Control and Signal Processing*, 29(2):259–271, 2015. 23

[78] Iman Shames, Soura Dasgupta, Barış Fidan, and Brian DO Anderson. Circumnavigation using distance measurements under slow drift. *IEEE Transactions on Automatic Control*, 57(4):889–903, 2012. 22, 23, 44

[79] Hamid Teimoori and Andrey V Savkin. Equiangular navigation and guidance of a wheeled mobile robot based on range-only measurements. *Robotics and Autonomous Systems*, 58(2):203–215, 2010. 23

[80] Alexey S Matveev, Hamid Teimoori, and Andrey V Savkin. Range-only measurements based target following for wheeled mobile robots. *Automatica*, 47(1):177–184, 2011.

[81] Yongcan Cao. UAV circumnavigating an unknown target under a GPS-denied environment with range-only measurements. *Automatica*, 55:150–158, May 2015. ISSN 0005-1098. doi: 10.1016/j.automatica.2015.03.007.

[82] Gaurav Chaudhary, Arpita Sinha, Twinkle Tripathy, and Aseem Borkar. Conditions for target tracking with range-only information. *Robotics and Autonomous Systems*, 75:176–186, 2016. 23

[83] Samet Güler, Barış Fidan, Soura Dasgupta, Brian DO Anderson, and Iman Shames. Adaptive source localization based station keeping of autonomous vehicles. *IEEE Transactions on Automatic Control*, 62(7):3122–3135, 2017. 23, 44

[84] Sandra H Dandach, Barış Fidan, Soura Dasgupta, and Brian DO Anderson. A continuous time linear adaptive source localization algorithm, robust to persistent drift. *Systems & Control Letters*, 58(1):7–16, 2009. 23

[85] Alvika Gautam, PB Sujit, and Srikanth Saripalli. A survey of autonomous landing techniques for uavs. In *2014 International Conference on Unmanned Aircraft Systems (ICUAS)*, pages 1210–1218. IEEE, 2014. 24

[86] Shaogang Jin, Jiyang Zhang, Lincheng Shen, and Tengxiang Li. On-board vision autonomous landing techniques for quadrotor: A survey. In *2016 35th Chinese Control Conference (CCC)*, pages 10284–10289. IEEE, 2016.

[87] Roland Brockers, Sara Susca, David Zhu, and Larry Matthies. Fully self-contained vision-aided navigation and landing of a micro air vehicle independent from external sensor inputs. In *Unmanned Systems Technology XIV*, volume 8387, page 83870Q. International Society for Optics and Photonics, 2012.

[88] Shaowu Yang, Sebastian A Scherer, and Andreas Zell. An onboard monocular vision system for autonomous takeoff, hovering and landing of a micro aerial vehicle. *Journal of Intelligent & Robotic Systems*, pages 1–17, 2013.

[89] Maximilian Laiacker, Konstantin Kondak, Marc Schwarzbach, and Tin Muskardin. Vision aided automatic landing system for fixed wing uav. In *2013 IEEE/RSJ International Conference on Intelligent Robots and Systems (IROS)*, pages 2971–2976. IEEE, 2013.

[90] Kevin Ling. Precision landing of a quadrotor uav on a moving target using low-cost sensors. Master's thesis, University of Waterloo, 2014.

[91] Karl Engelbert Wenzel, Andreas Masselli, and Andreas Zell. Automatic take off, tracking and landing of a miniature uav on a moving carrier vehicle. *Journal of Intelligent & Robotic systems*, 61(1):221–238, 2011.

[92] Davide Falanga, Alessio Zanchettin, Alessandro Simovic, Jeffrey Delmerico, and Davide Scaramuzza. Vision-based autonomous quadrotor landing on a moving platform. In *2017 IEEE International Symposium on Safety, Security and Rescue Robotics (SSRR)*. IEEE, 2017. 24

[93] Alexandre Borowczyk, Duc-Tien Nguyen, André Phu-Van Nguyen, Dang Quang Nguyen, David Saussié, and Jerome Le Ny. Autonomous landing of a multirotor micro air vehicle on a high velocity ground vehicle. *IFAC-PapersOnLine*, 50(1):10488–10494, 2017. 24

[94] Daniel Briggs Wilson, Ali Göktogan, and Salah Sukkarieh. Guidance and navigation for uav airborne docking. In *Robotics: Science and Systems*, volume 3, 2015. 24

[95] Weiwei Kong, Daibing Zhang, Xun Wang, Zhiwen Xian, and Jianwei Zhang. Autonomous landing of an uav with a ground-based actuated infrared stereo vision system. In *2013 IEEE/RSJ International Conference on Intelligent Robots and Systems (IROS)*, pages 2963–2970. IEEE, 2013. 24

[96] Yang Gui, Pengyu Guo, Hongliang Zhang, Zhihui Lei, Xiang Zhou, Jing Du, and Qifeng Yu. Airborne vision-based navigation method for uav accuracy landing using infrared lamps. *Journal of Intelligent & Robotic Systems*, 72 (2):197, 2013. 24

[97] Wei Ren. Consensus strategies for cooperative control of vehicle formations. *IET Control Theory & Applications*, 1(2):505–512, 2007. 25

[98] Laura Krick, Mireille E Broucke, and Bruce A Francis. Stabilisation of infinitesimally rigid formations of multi-robot networks. *International Journal of Control*, 82(3):423–439, 2009.

[99] Jing Guo, Zhiyun Lin, Ming Cao, and Gangfeng Yan. Adaptive leader-follower formation control for autonomous mobile robots. In *2010 American Control Conference*, pages 6822–6827. IEEE, 2010.

[100] Zhiyun Lin, Lili Wang, Zhiyong Chen, Minyue Fu, and Zhimin Han. Necessary and sufficient graphical conditions for affine formation control. *IEEE Transactions on Automatic Control*, 61(10):2877–2891, 2016.

[101] Zhiyong Sun, Shaoshuai Mou, Brian DO Anderson, and A Stephen Morse. Rigid motions of 3-d undirected formations with mismatch between desired distances. *IEEE Transactions on Automatic Control*, 62(8):4151–4158, 2017.

[102] Tingrui Han, Zhiyun Lin, and Minyue Fu. Three-dimensional formation merging control under directed and switching topologies. *Automatica*, 58: 99–105, 2015. 26

[103] Zhimin Han, Lili Wang, Zhiyun Lin, and Ronghao Zheng. Formation control with size scaling via a complex laplacian-based approach. *IEEE Transactions on Cybernetics*, 46(10):2348–2359, 2016. 90

[104] Zhiyun Lin, Lili Wang, Zhimin Han, and Minyue Fu. A graph laplacian approach to coordinate-free formation stabilization for directed networks. *IEEE Transactions on Automatic Control*, 61(5):1269–1280, 2016. 25

[105] Meysam Basiri, Adrian N Bishop, and Patric Jensfelt. Distributed control of triangular formations with angle-only constraints. *Systems & Control Letters*, 59(2):147–154, 2010. 25

[106] Shiyu Zhao and Daniel Zelazo. Bearing rigidity and almost global bearing-only formation stabilization. *IEEE Transactions on Automatic Control*, 61 (5):1255–1268, 2016.

[107] Shiyu Zhao and Daniel Zelazo. Translational and scaling formation maneuver control via a bearing-based approach. *IEEE Transactions on Control of Network Systems*, 4(3):429–438, 2017. 25

[108] Ming Cao, Changbin Yu, and Brian DO Anderson. Formation control using range-only measurements. *Automatica*, 47(4):776–781, 2011. 25

[109] Bomin Jiang, Mohammad Deghat, and Brian DO Anderson. Simultaneous velocity and position estimation via distance-only measurements with application to multi-agent system control. *IEEE Transactions on Automatic Control*, 62(2):869–875, 2017. 25

[110] Ioannis Sarras, Julien Marzat, Sylvain Bertrand, and Hélène Piet-Lahanier. Collaborative multiple micro air vehicles localization and target tracking in gps-denied environment from range–velocity measurements. *International Journal of Micro Air Vehicles*, 10(2):225–239, 2018. 25, 26, 90, 92

[111] Zhimin Han, Kexin Guo, Lihua Xie, and Zhiyun Lin. Integrated relative localization and leader–follower formation control. *IEEE Transactions on Automatic Control*, 64(1):20–34, 2018. 25, 112

[112] Bomin Jiang, Mohammad Deghat, and Brian DO Anderson. Translational velocity consensus using distance-only measurements. In *2013 IEEE 52nd Annual Conference on Decision and Control (CDC)*, pages 2746–2751. IEEE, 2013. 25

[113] Bomin Jiang, Mohammad Deghat, and Brian DO Anderson. Velocity consensus and formation shape control using distance-only measurements. *IEEE Transactions on Automatic Control*, 2016. 25

[114] Guofei Chai, Zhiyun Lin, and Minyue Fu. Consensus-based cooperative source localization of multi-agent systems. In *2013 32nd Chinese Control Conference (CCC)*, pages 6809–6814. IEEE, 2013. 25, 90

[115] Ioannis Sarras, Julien Marzat, Sylvain Bertrand, and Hélène Piet-Lahanier. Collaborative multi-vehicle localization with respect to static/dynamic target from range and velocity measurements. In *2017 International Conference on Unmanned Aircraft Systems (ICUAS)*, pages 850–859. IEEE, 2017. 25, 90

[116] Felipe R. Fabresse, Fernando Caballero, Ivan Maza, and Anibal Ollero. Localization and mapping for aerial manipulation based on range-only measurements and visual markers. In *2014 IEEE International Conference on Robotics and Automation (ICRA)*, pages 2100–2106. IEEE, 2014. 27

[117] James Diebel. Representing attitude: Euler angles, unit quaternions, and rotation vectors. *Matrix*, 58(15-16):1–35, 2006. 31

[118] Markus W Achtelik. *Advanced closed loop visual navigation for micro aerial vehicles*. PhD thesis, ETH Zurich, 2014. 31

[119] Paul G Savage. Strapdown inertial navigation integration algorithm design part 1: Attitude algorithms. *Journal of Guidance, Control, and Dynamics*, 21(1):19–28, 1998.

[120] Paul G Savage. Strapdown inertial navigation integration algorithm design part 2: Velocity and position algorithms. *Journal of Guidance, Control, and Dynamics*, 21(2):208–221, 1998. 31

[121] Chen Wang, Tete Ji, Thien-Minh Nguyen, and Lihua Xie. Correlation flow: robust optical flow using kernel cross-correlators. In *2018 IEEE International Conference on Robotics and Automation (ICRA)*, pages 836–841. IEEE, 2018. 32

[122] Maxim Shchekotov. Indoor localization method based on wi-fi trilateration technique. In *Proceedings of the 16th Conference of FRUCT Association*, pages 177–179, 2014. 43

[123] Petros Ioannou and Bariş Fidan. *Adaptive Control Tutorial*. SIAM, 2006. 48, 52, 81, 99

[124] Wenjun Mei and Francesco Bullo. Lasalle invariance principle for discrete-time dynamical systems: A concise and self-contained tutorial. *arXiv preprint arXiv:1710.03710*, 2017. 54, 55

[125] Richard M Johnstone, C Richard Johnson, Robert R Bitmead, and Brain DO Anderson. Exponential convergence of recursive least squares with exponential forgetting factor. In *1982 21st IEEE Conference on Decision and Control*, pages 994–997. IEEE, 1982. 83, 118

[126] John Wang and Edwin Olson. AprilTag 2: Efficient and robust fiducial detection. In *2016 IEEE/RSJ International Conference on Intelligent Robots and Systems (IROS)*, pages 4193–4198. IEEE, oct 2016. ISBN 978-1-5090-3762-9. doi: 10.1109/IROS.2016.7759617. 85

[127] Wei Wang, Changyun Wen, Jiangshuai Huang, and Zhengguo Li. Hierarchical decomposition based consensus tracking for uncertain interconnected systems via distributed adaptive output feedback control. *IEEE Transactions on Automatic Control*, 61(7):1938–1945, 2015. 112, 124

[128] Zhiyun Zhao, Yiguang Hong, and Zongli Lin. Semi-global output consensus of a group of linear systems in the presence of external disturbances and actuator saturation: An output regulation approach. *International Journal of Robust and Nonlinear Control*, 26(7):1353–1375, 2016. 112, 124

[129] Housheng Su, Yuan Qiu, and Lei Wang. Semi-global output consensus of discrete-time multi-agent systems with input saturation and external disturbances. *ISA Transactions*, 67:131–139, 2017. 112, 124

[130] Xiwang Dong and Guoqiang Hu. Time-varying formation tracking for linear multiagent systems with multiple leaders. *IEEE Transactions on Automatic Control*, 62(7):3658–3664, July 2017. ISSN 0018-9286. doi: 10.1109/TAC.2017.2673411. 115

[131] Lara Brinón-Arranz, Alexandre Seuret, and Carlos Canudas-de Wit. Cooperative control design for time-varying formations of multi-agent systems. *IEEE Transactions on Automatic Control*, 59(8):2283–2288, 2014. 115

[132] Ziyang Meng, Zongli Lin, and Wei Ren. Robust cooperative tracking for multiple non-identical second-order nonlinear systems. *Automatica*, 49(8):2363–2372, 2013. 119

[133] Hai-Tao Zhang, Zhiyong Chen, and Xiaoyu Mo. Effect of adding edges to consensus networks with directed acyclic graphs. *IEEE Transactions on Automatic Control*, 62(9):4891–4897, 2017. 125

[134] Xiaoyu Mo, Zhiyong Chen, and Hai-Tao Zhang. Effects of adding a reverse edge across a stem in a directed acyclic graph. *Automatica*, 103:254–260, 2019. 125